

# The Atlantic Subtropical Cells - mean state and variability from an observational perspective

## Dissertation

zur Erlangung des Doktorgrades  
der Mathematisch-Naturwissenschaftlichen Fakultät  
der Christian-Albrechts-Universität zu Kiel

vorgelegt von

**Franz Philip Tuchen**

Kiel, August 2020





Erste Gutachterin: Prof. Dr. Joke F. Lübbecke  
Zweiter Gutachter: Prof. Dr. Mojib Latif  
Tag der mündlichen Prüfung: 23.10.2020  
Zum Druck genehmigt: 23.10.2020



# Abstract

The Atlantic Subtropical Cells (STCs) are shallow wind-driven overturning circulations that consist of poleward Ekman transport from the tropics to the subtropics in the surface layer, subduction in the subtropics and equatorward geostrophic flow at thermocline level. They are eventually closed by equatorial and eastern boundary upwelling. To date, the Atlantic STCs have mainly been investigated in general circulation or data assimilation models while the only observational study has been conducted before the Argo float era.

In this thesis, for the first time, the mean state of the horizontal branches of the Atlantic STCs is characterized along  $10^\circ\text{N}$  and  $10^\circ\text{S}$  based on 13 years of hydrographic data from Argo floats. The interface depth between the surface layer and the thermocline layer is defined by the seasonally varying depth at which the meridional velocity reverses sign from poleward to equatorward (30 – 70 m). The lower boundary of the thermocline layer is characterized by another flow reversal at the  $26.0\text{ kg m}^{-3}$  isopycnal. Within the thermocline layer, a mean equatorward transport of about  $9\text{ Sv}$  ( $5\text{ Sv}$  at the western boundary west of  $32^\circ\text{W}$ ,  $4\text{ Sv}$  in the interior) along  $10^\circ\text{S}$  is observed. Here, the western boundary transport at  $10^\circ\text{S}$  is derived from ship section data because of a transport underestimation by Argo float data. In contrast, only about  $3\text{ Sv}$  of equatorward transport are entering the equatorial region at thermocline level along  $10^\circ\text{N}$  of which the majority is concentrated at the western boundary west of  $50^\circ\text{W}$ . This asymmetric thermocline layer transport convergence is largely balanced by a rather symmetric net transport divergence in the surface layer, where the Ekman divergence exceeds the geostrophic convergence. Overall, the resulting residual of about  $3\text{ Sv}$  is attributed to western boundary transport uncertainty at  $10^\circ\text{N}$  and diapycnal transport equatorward of  $10^\circ\text{N/S}$  associated with the northward return flow of the Atlantic Meridional Overturning Circulation that partly upwells in the tropics.

With this newly available Argo float data set, another part of this thesis focuses on the observed transport variability of the individual horizontal branches of the Atlantic STCs with an emphasis on their connection to tropical sea surface temperature (SST) anomalies. For the first time, surface layer and thermocline layer transport time series associated with the Atlantic STCs are derived from Argo float observations. Both layers are dominated by seasonal variability. The thermocline layer convergence varies from 7 – 14 Sv whereas the surface layer divergence varies from 0 to more than 20 Sv between boreal summer and winter, respectively. Although interannual transport fluctuations at thermocline level are relatively weak, they are suggested to modulate equatorial SST anomalies at time scales of  $\sim 5$  years and longer. Re-

markably, at these time scales, only positive anomalies of the interior part of the thermocline layer transport convergence are leading negative equatorial SST anomalies. At shorter time scales, both SST and interior thermocline layer transport convergence anomalies are rather forced in parallel by local changes of zonal wind stress. Moreover, at thermocline level, the western boundary transport component is anti-correlated with interior transport anomalies on all time scales and in both hemispheres. Due to the small time lags between both transport components, it is suggested that locally forced westward propagating Rossby waves cause the anti-correlation. However, Rossby waves that are forced poleward of the zonal sections at  $10^{\circ}$  N/S and reach the western boundary to propagate equatorward are expected to distort the initial time lag due to the locally forced Rossby waves.

Overall, the results of this thesis provide a new detailed description of the different characteristics of the Atlantic STCs in terms of both their mean state and temporal variability while shedding light on processes that so far have only been observed in the Pacific Ocean or in model studies. It further proves the relevance and capability of Argo float observations within the scope of the Atlantic STC circulation while also addressing their limitations. Eventually, the results aim to provide a benchmark against which general circulation models should be validated.

# Zusammenfassung

Die Atlantischen Subtropischen Zellen (STCs) sind flache windgetriebene Umwälzbewegungen, die aus polwärtigem Ekman-Transport in der Oberflächenschicht, Subduktion in den Subtropen und äquatorwärtigem, geostrophischem Transport in der Thermoklinenschicht bestehen. Sie werden durch Auftrieb entlang des Äquators und in den Auftriebsgebieten am östlichen Rand geschlossen. Bislang wurden die Atlantischen STCs hauptsächlich in Zirkulations- oder Daten-Assimilations-Modellen untersucht, wohingegen die einzige Beobachtungsstudie bereits vor Beginn des Argo-Programmes durchgeführt wurde.

In dieser Arbeit wird zum ersten Mal der mittlere Zustand der horizontalen Zweige der Atlantischen STCs anhand von 13 Jahren Argo-Drifter-Daten entlang von  $10^\circ$  N und  $10^\circ$  S beschrieben. Die Grenzfläche zwischen der Oberflächenschicht und der Thermoklinenschicht ist durch die saisonal variierende Tiefe, in der sich das Vorzeichen der meridionalen Geschwindigkeit von polwärtig zu äquatorwärtig umkehrt, definiert (30 – 70 m). Die untere Grenze der Thermoklinenschicht wird durch eine weitere Umkehr der Meridionalgeschwindigkeit auf der  $26.0 \text{ kg m}^{-3}$  Isopykne bestimmt. Innerhalb der Thermoklinenschicht wird ein äquatorwärtiger Transport von etwa  $9 \text{ Sv}$  ( $5 \text{ Sv}$  entlang des westlichen Randes westlich von  $32^\circ$  W,  $4 \text{ Sv}$  im Inneren) entlang von  $10^\circ$  S beobachtet. Aufgrund einer Unterschätzung des Transportes am westlichen Rand bei  $10^\circ$  S durch Argo-Daten, wird der Transport dort durch einen mittleren Schiffsschnitt bestimmt. Demgegenüber stehen etwa  $3 \text{ Sv}$  äquatorwärtiger Transport entlang von  $10^\circ$  N, von dem die Mehrheit über den westlichen Rand westlich von  $50^\circ$  W Richtung Äquator strömt. Die Asymmetrie der Transport-Konvergenz in der Thermoklinenschicht wird zum großen Teil durch eine symmetrische Transport-Divergenz in der Oberflächenschicht balanciert, wobei die Ekman-Divergenz die geostrophische Konvergenz übertrifft. Insgesamt wird das resultierende Residuum von etwa  $3 \text{ Sv}$  sowohl der Transportunsicherheit am westlichen Rand bei  $10^\circ$  N als auch dem diapiknischen Transport äquatorwärtig von  $10^\circ$  N/S als Teil des partiellen Auftriebes der nordwärtigen Atlantischen Meridionalen Umwälzbewegung in den Tropen zugeschrieben. Mithilfe dieses neu verfügbaren Argo-Drifter-Datensatzes kann - ebenfalls zum ersten Mal - anhand von Beobachtungsdaten ein Einblick in die Transportvariabilität der einzelnen horizontalen STC-Zweige gewährt werden. Hierbei liegt der Schwerpunkt auf deren Verbindung zu Anomalien der tropischen Meeresoberflächentemperatur (SST). In beiden Schichten dominiert die saisonale Variabilität. Die Transport-Konvergenz in der Thermoklinenschicht variiert zwischen  $7 \text{ Sv}$  im borealen Sommer und  $14 \text{ Sv}$  im borealen Winter während die Transport-Divergenz in der Oberflächenschicht zwischen 0 und mehr als  $20 \text{ Sv}$  variiert. Obwohl interannuale Trans-

portschwankungen relativ schwach sind, lässt sich zeigen, dass sie auf Zeitskalen von  $\sim 5$  Jahren und länger äquatoriale SST-Anomalien modulieren. Bemerkenswerterweise geht eine positive Anomalie des inneren Anteils der Transportkonvergenz in der Thermoklinenschicht nur auf diesen Zeitskalen einer negativen äquatorialen SST-Anomalie voraus. Auf kürzeren Zeitskalen hingegen sind sowohl SST- als auch STC-Schwankungen eher lokal durch zonale Wind-Stress-Variabilität angetrieben. Daneben sind Transportanomalien im Inneren außerdem mit Transportanomalien am westlichen Rand antikorreliert. Die Ergebnisse weisen darauf hin, dass lokal erzeugte westwärts propagierende Rossby-Wellen für diese Anti-Korrelation verantwortlich sind und zu kurzen Zeitversätzen zwischen den beiden Transportkomponenten führen. Es ist naheliegend, dass Rossby-Wellen polwärts der zonalen Schnitte bei  $10^\circ$  N/S erzeugt werden und über den westlichen Rand zum Äquator propagieren und dadurch die zeitliche Verzögerung bei  $10^\circ$  N/S beeinflussen, die durch die lokalen Rossby-Wellen zwischen Transportanomalien im Inneren und am westlichen Rand entstehen.

Die Resultate dieser Arbeit liefern neue detaillierte Einblicke in die verschiedenen Charakteristiken der Atlantischen STCs sowohl im Hinblick auf deren mittleren Zustand als auch auf deren zeitliche Variabilität, sodass Prozesse untersucht werden können, die bisher Studien über die Pazifischen STCs vorbehalten waren. Des Weiteren wird die Relevanz und Bedeutung von Argo-Driftern am Beispiel der Atlantischen STCs belegt. Gleichzeitig werden aber auch Einschränkungen und Verbesserungspotential angesprochen. Letztendlich bilden die Ergebnisse eine wichtige Referenz, mit der zukünftige Modell-Studien validiert werden können.



# Contents

<b>Abstract</b>	<b>I</b>
<b>Zusammenfassung</b>	<b>III</b>
<b>Contents</b>	<b>V</b>
<b>List of Figures</b>	<b>VII</b>
<b>List of Tables</b>	<b>IX</b>
<b>List of Abbreviations</b>	<b>XI</b>
<b>1 Motivation, study aims and outline</b>	<b>1</b>
<b>2 Scientific Background</b>	<b>5</b>
2.1 Momentum equation and fundamental balances . . . . .	5
2.2 Mean circulation of the upper tropical Atlantic . . . . .	8
2.3 Tropical Atlantic Variability . . . . .	9
2.4 The ventilated thermocline and the Subtropical Cells . . . . .	11
2.4.1 Theoretical background . . . . .	12
2.4.2 Mean state and variability . . . . .	13
<b>3 The mean Atlantic Subtropical Cells inferred from observations</b>	<b>17</b>
3.1 Introduction . . . . .	19
3.2 Data . . . . .	21
3.2.1 Argo Climatological Data . . . . .	21
3.2.2 Western Boundary Ship Section . . . . .	22
3.2.3 Monthly Isopycnal and Mixed-layer Ocean Climatology . . . . .	23
3.2.4 Ocean Reanalysis 4 . . . . .	23
3.2.5 Wind Products . . . . .	24
3.3 Methods . . . . .	24
3.3.1 Thermocline Transport . . . . .	24
3.3.2 Surface Transport . . . . .	25

3.4	Results . . . . .	25
3.4.1	Thermocline Transports . . . . .	25
3.4.2	Surface Transports . . . . .	31
3.5	Summary and Discussion . . . . .	34
<b>4</b>	<b>Observed transport variability of the Atlantic Subtropical Cells and their connection to tropical sea surface temperature variability</b>	<b>41</b>
4.1	Introduction . . . . .	43
4.2	Data . . . . .	45
4.3	Methods . . . . .	46
4.3.1	Thermocline Transports . . . . .	46
4.3.2	Ekman and surface layer transports . . . . .	49
4.4	Results . . . . .	49
4.4.1	Transport variability of the horizontal STC branches . . . . .	49
4.4.2	Western boundary vs. interior transport anomalies . . . . .	54
4.4.3	Impact on sea surface temperature variability . . . . .	57
4.5	Summary and conclusion . . . . .	64
<b>5</b>	<b>Conclusion</b>	<b>69</b>
5.1	Scientific progress . . . . .	69
5.2	Outlook . . . . .	76
5.2.1	The recent strengthening of the STCs . . . . .	76
5.2.2	EUC water mass analysis . . . . .	80
5.2.3	Concluding remarks . . . . .	81
	<b>Bibliography</b>	<b>83</b>
	<b>Academic CV</b>	<b>95</b>
	<b>Publications</b>	<b>97</b>
	<b>Acknowledgments</b>	<b>99</b>
	<b>Declaration</b>	<b>101</b>

# List of Figures

1.1	Schematic representation of the circulation associated with the Atlantic Sub-tropical Cells . . . . .	2
1.2	Thermocline layer transport convergence vs. tropical sea surface temperature anomalies from observations in the Pacific Ocean . . . . .	3
2.1	Schematic representation of the different dynamical regions of the analytical solution of McCreary & Lu (1994) . . . . .	12
3.1	Spatial distribution of Argo profiles between 2004 and 2016 in the tropical Atlantic Ocean . . . . .	22
3.2	Mean zonal sections of hydrography and meridional geostrophic velocity from Argo floats at 10° N and 10° S . . . . .	27
3.3	Mean zonally integrated meridional geostrophic transport as a function of potential density at 10° N and 10° S . . . . .	28
3.4	Zonally averaged vertical profiles of meridional velocity from ORA-S4 at 10° N and 10° S . . . . .	29
3.5	Thermocline layer geostrophic transport in the tropical Atlantic Ocean from Argo data . . . . .	30
3.6	Cumulative meridional transport within the thermocline layer for different data products at 10° N and 10° S . . . . .	31
3.7	Mean zonal sections of hydrography and meridional velocity from the mean ship section along 11.5° S . . . . .	33
3.8	Mean meridional Ekman transport in the tropical Atlantic Ocean from ASCAT wind stress data . . . . .	34
3.9	Schematic of transport associated with the horizontal branches of the Atlantic STCs . . . . .	38
4.1	Mean absolute geostrophic velocities in the tropical Atlantic Ocean within the thermocline layer from Argo data . . . . .	48
4.2	Time series of thermocline layer transport components at 10° N and 10° S for different data products . . . . .	51
4.3	Time series of surface layer transport components at 10° N and 10° S for different data products . . . . .	52

4.4	Monthly climatology of thermocline layer, Ekman layer and surface layer transport components . . . . .	53
4.5	Monthly time series of western boundary and interior transport anomalies from Argo data and ORAS4 . . . . .	54
4.6	Linear regression of thermocline layer meridional geostrophic velocity onto interior thermocline layer transport anomalies . . . . .	56
4.7	Time series of the hemispheric components of thermocline layer transport convergence anomalies from Argo data and ORAS4 . . . . .	57
4.8	Transport anomaly of the horizontal STC branches vs. equatorial SST anomalies (2-year running mean) . . . . .	59
4.9	Transport anomaly of the horizontal STC branches vs. equatorial SST anomalies (5-year running mean) . . . . .	60
4.10	WB and INT thermocline layer transport convergence anomaly vs. equatorial SST anomaly on different time scales . . . . .	61
4.11	Linear regression map of STC transport anomalies onto equatorial SST anomalies (5-year running mean) . . . . .	62
4.12	Lag correlation analysis between zonal wind stress, equatorial SST and STC transport anomalies . . . . .	63
5.1	Monthly time series of equatorial zonal velocity anomaly (mean and seasonal cycle subtracted) at 23° W and 10° W . . . . .	77
5.2	Linear decadal trend and mean equatorial zonal velocity at the 23° W and 10° W mooring sites . . . . .	78
5.3	Linear decadal trend of zonal wind stress between 2008 to 2018 from ASCAT wind stress data . . . . .	79
5.4	Linear decadal trend of poleward Ekman transport between 2008 to 2018 from ASCAT wind stress data . . . . .	80

# List of Tables

3.1	Thermocline layer transport components at 10° N and 10° S for different data products . . . . .	32
3.2	Surface layer (geostrophic + Ekman) transport components at 10° N and 10° S for different data products . . . . .	35



# List of Abbreviations

Abbreviation	Meaning
AD	Angola Dome
ADCP	Acoustic Doppler Current Profiler
AMM	Atlantic Meridional Mode
AMO	Atlantic Multidecadal Oscillation
AMOC	Atlantic Meridional Overturning Circulation
ASCAT	Advanced Scatterometer
AZM	Atlantic Zonal Mode
BC	Brazil Current
cSEC	central South Equatorial Current
CTD	Conductivity-Temperature-Depth
EDJs	Equatorial Deep Jets
ENSO	El-Niño Southern Oscillation
EUC	Equatorial Undercurrent
GD	Guinea Dome
INT	Interior Ocean
ITCZ	Intertropical Convergence Zone
MIMOC	Monthly Isopycnal and Mixed-Layer Ocean Climatology
MOC	Meridional Overturning Circulation
NAO	North Atlantic Oscillation
NBC	North Brazil Current
NBUC	North Brazil Undercurrent
NEC	North Equatorial Current
NECC	North Equatorial Counter Current
NEUC	North Equatorial Undercurrent
nSEC	northern South Equatorial Current
SEC	South Equatorial Current
sSEC	southern South Equatorial Current
SEUC	South Equatorial Undercurrent
SST	Sea Surface Temperature
STC	Subtropical Cell
TAV	Tropical Atlantic Variability
TC	Tropical Cell
TIWs	Tropical Instability Waves
WAM	West African Monsoon
WB	Western Boundary
WWV	Warm Water Volume





# 1 Motivation, study aims and outline

Tropical sea surface temperature (SST) is an important component of the coupled ocean-atmosphere system and impacts climate variability on the surrounding continents (e.g. [Carton et al., 1996](#); [Chang et al., 1998](#)). On decadal time scales, shallow meridional overturning circulations, the so-called Subtropical Cells (STCs), are suggested to modulate tropical SST variability ([McPhaden and Zhang, 2002](#)) and could therefore play an important role in the prediction of climate hazards such as hurricane activity and droughts/floods over South America and Africa ([Foltz et al., 2019](#)). The shallow oceanic circulation of the tropical Atlantic is characterized by a superposition of wind- and density-driven currents (e.g. [Schott et al., 2004](#), Fig. 1.1). Together, these two circulation components form the STCs which provide a connection between the subtropical subduction regions and the equatorial and eastern boundary upwelling regions ([McCreary and Lu, 1994](#); [Liu et al., 1994](#)). In a simplified, zonally averaged view, the STCs consist of poleward Ekman transport at the surface, subduction within the subtropical gyres, equatorward geostrophic flow at thermocline level and upwelling along the equator and the eastern boundary ([Fratantoni et al., 2000](#); [Malanotte-Rizzoli et al., 2000](#); [Schott et al., 2004](#)). Apart from their impact on tropical SST anomalies, the STCs are also an important mechanism for the ventilation of the tropical thermocline ([Luyten et al., 1983](#)).

To date, the mean characteristics of the Atlantic STCs are largely derived from the output of ocean general circulation models (e.g. [Fratantoni et al., 2000](#); [Malanotte-Rizzoli et al., 2000](#); [Inui et al., 2002](#); [Hazeleger et al., 2003](#); [Hazeleger and Drijfhout, 2006](#); [Hüttl and Böning, 2006](#)) and data assimilation models ([Rabe et al., 2008](#)). The only observation-based description of the mean Atlantic STCs was published by [Zhang et al. \(2003\)](#), relying on hydrographic data from the World Ocean Atlas. At the time of their publication, the global Argo float program was still in its initial phase but has since turned out to fundamentally improve the observational coverage of vertical temperature and salinity profiles across the world oceans. Argo floats are autonomously drifting buoys generally covering the upper 2000 m. They are operating in cycles of around 10 days. Prior to their ascent, during which the CTD profile is measured, they float at a neutral isobaric surface (mostly around 1000 dbar) for several days, often referred to as the parking depth (e.g. [Lebedev et al., 2007](#)). In August 2020, almost 4,000 Argo floats are actively providing hydrographic data around the globe (<https://argo.ucsd.edu/about/status>). In contrast, [Zhang et al. \(2003\)](#) based their analysis on about 7,000 to 30,000 deep hydrographic casts per decade between 40° S and 50° N. The extensive set of observational hydrographic data provided by Argo floats now

facilitates a more robust description of the mean state of the Atlantic STC circulation and promises new insights into its transport components and associated variability.

Historically, the Atlantic STCs gained less attention than their counterparts in the Pacific Ocean. Thus, an exciting finding about STC variability was first described by [McPhaden and Zhang \(2002\)](#) for the equatorial Pacific. Based on observational data, the authors could demonstrate a connection between a long-term trend of decreasing transport convergence in the thermocline layer and a simultaneous positive trend in tropical SST anomalies (Fig. 1.2). These findings suggest that the thermocline layer branches of the STCs are able to modulate tropical SST on decadal time scales. This connection has later been confirmed by several model studies (e.g. [Zhang and McPhaden, 2006](#); [Lübbecke et al., 2008](#); [Farneti et al., 2014](#)) and also in additional observational studies ([McPhaden and Zhang, 2004](#)).

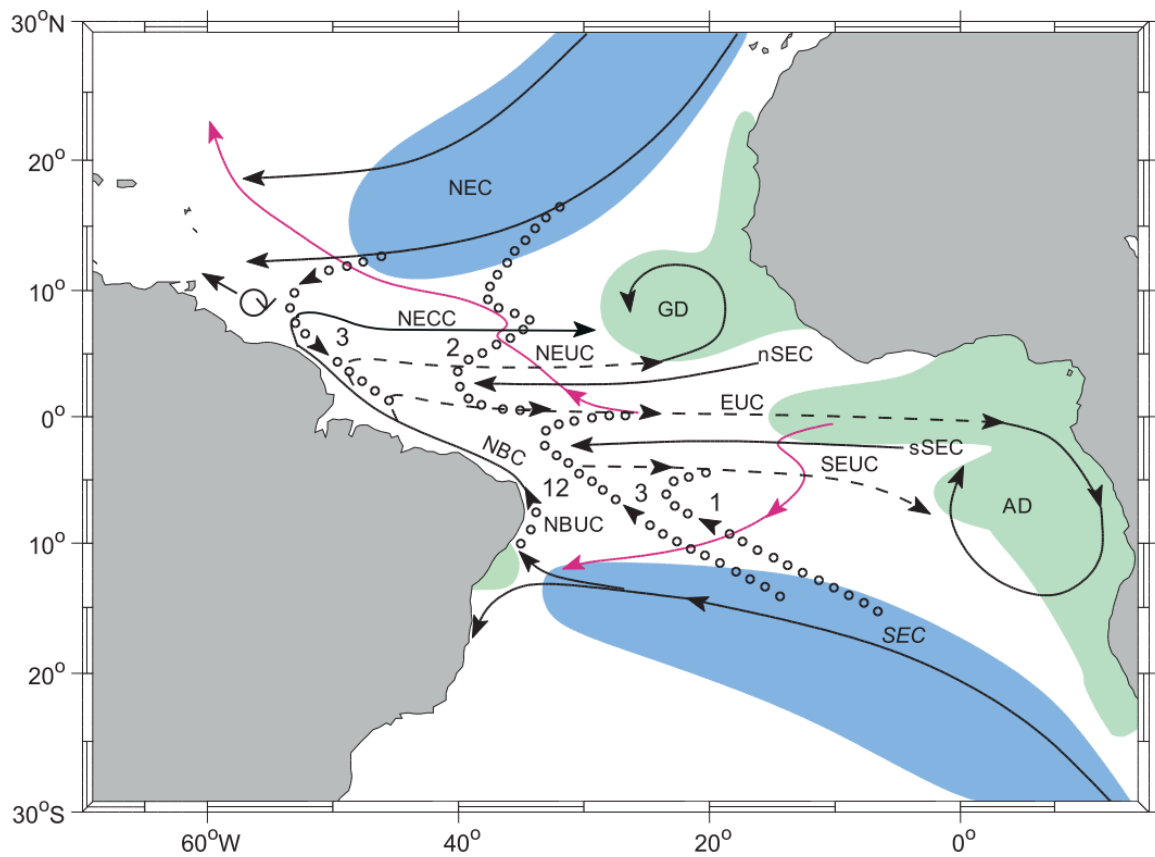


**Figure 1.1:** Schematic representation of the Atlantic STC circulation with areas of subduction (blue) and upwelling regions (green). Surface currents are marked by solid lines, while subsurface currents are marked by dashed lines. Interior equatorward transport pathways are indicated by the dotted lines and surface poleward transport pathways are indicated by magenta solid lines. Transport values are given in Sv ( $= 10^6 \text{ m}^3 \text{ s}^{-1}$ ) (Figure adapted from [Schott et al., 2004](#)).

However, the sparsity of available data forced [McPhaden and Zhang \(2002\)](#) to derive decadal transport averages rather than a continuous time series. In fact, at the western boundary, hy-

drographic data coverage was too sparse to derive reliable transport values there. Therefore, the authors were only able to relate the thermocline layer transport convergence of the interior basin to decadal SST fluctuations. The findings of *McPhaden and Zhang (2002)* raise the question whether a comparable relation for the Atlantic Ocean can be found.

Their suggested impact on tropical SST anomalies underlines the role of the STCs on climate parameters such as extreme rainfall or droughts. In the Atlantic, these climate hazards are rather associated with the meridional or zonal mode (e.g. *Carton et al., 1996; Kushnir et al., 2006; Keenlyside and Latif, 2007*), but could be modulated by the STCs on interannual to decadal time scales.

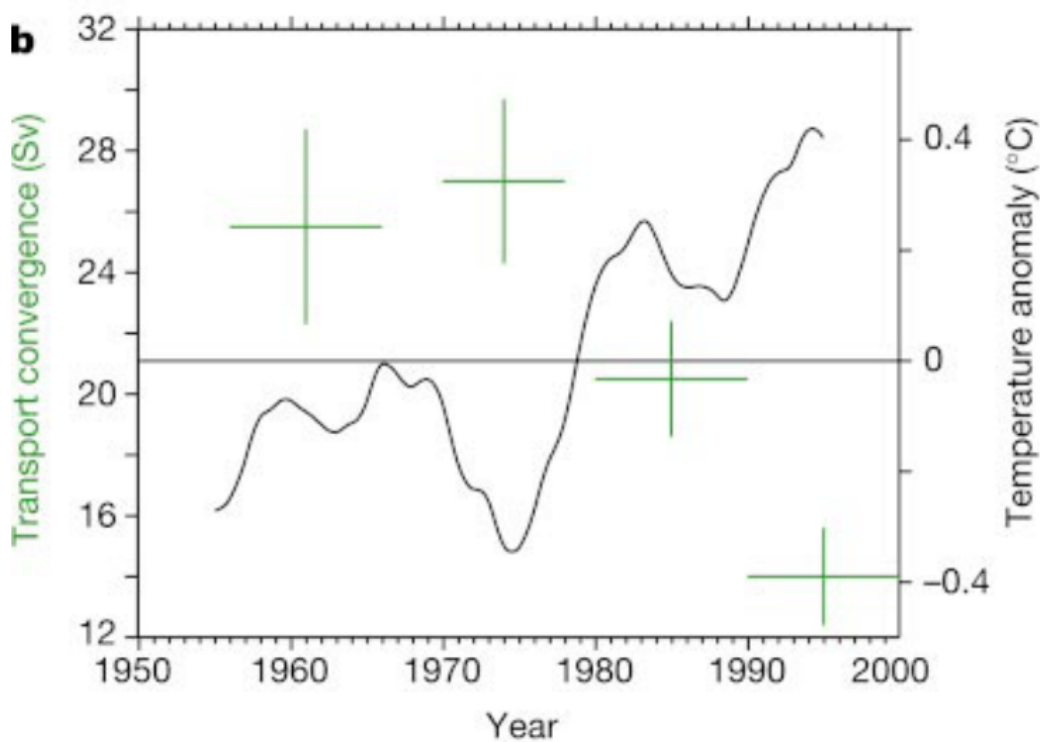


**Figure 1.2:** Meridional thermocline layer ( $22.0\text{--}26.0\text{ kg m}^{-3}$ ) transport convergence between  $9^\circ\text{ N}$  and  $9^\circ\text{ S}$  (green) and sea surface temperature anomalies averaged between  $9^\circ\text{ N}$  to  $9^\circ\text{ S}$  and  $90^\circ\text{ W}$  to  $180^\circ\text{ W}$  (solid line) relative to the 1950-1999 average. Anomalies are smoothed twice with a 5-year running mean (Figure adapted from *McPhaden and Zhang, 2002*).

In general, two mechanisms have been proposed on how the STCs could be connected to tropical SST anomalies. First, *Gu and Philander (1997)* formulated their theory that hypothesizes how subducted subtropical temperature anomalies ( $T'$ ) are transported towards the equator by a mean transport ( $\bar{v}$ ) at thermocline level. In this context, subduction describes the transfer of a water parcel from the surface mixed layer into the stratified thermocline layer. Second, *Kleeman et al. (1999)* proposed a more dynamic mechanism in which tropical SST anomalies are rather forced by a change of equatorward transport ( $v'$ ) while subducted temperature

anomalies are constant ( $\bar{T}$ ). Over the years, the majority of studies favored the so-called  $v'\bar{T}$  mechanism by *Kleeman et al.* (1999) and further contributed to a sharpened description of the exact characteristics of the mechanism in both the Atlantic and Pacific Ocean (e.g. *Nonaka et al.*, 2002; *Kröger et al.*, 2005; *Graffino et al.*, 2019). In contrast, the  $\bar{v}T'$  mechanism by *Gu and Philander* (1997) has been questioned by several studies since e.g. temperature anomalies have difficulties to propagate over such a long distance (e.g. *Schneider et al.*, 1999; *Hazeleger et al.*, 2001). The rather dynamic  $v'\bar{T}$  mechanism can be explained by a spin-up or spin-down of the entire shallow overturning circulations due to variations in the wind field, sometimes called STC loop (*Rabe et al.*, 2008) that could account for the almost instantaneous SST response to STC changes as observed in the Pacific Ocean (*McPhaden and Zhang*, 2002). An observational analysis of the relation between STC transport variability and tropical SST anomalies is carried out in this thesis for the first time in the Atlantic Ocean and will shed further light on the mechanism. With more than 15 years of available Argo data, it is now possible to derive an updated estimate of the mean state of the Atlantic STCs and to further explore the impact of STC transport variability on tropical SST anomalies. In this thesis, the following scientific questions will be addressed:

- Is the data density provided by Argo floats sufficient to realistically derive the mean characteristics of the Atlantic STC circulation? (Chapter 3)
- Given a sufficient distribution of Argo float data, what are the mean characteristics of the Atlantic STCs in terms of meridional transport, pathways and interhemispheric differences? (Chapter 3)
- What are the dominant time scales of transport variability observed in the individual horizontal branches of the Atlantic STCs? (Chapter 4)
- How is STC transport variability connected to tropical SST anomalies in the Atlantic? (Chapter 4)

The next chapter 2 provides an overview of the scientific background relevant for this thesis. In chapter 3, the different horizontal branches of the Atlantic STCs are identified in order to provide the first estimate of the mean state of the Atlantic STCs based on Argo float observations. Building up on the definitions given in chapter 3, the succeeding chapter 4 investigates the observed transport variability of the individual branches of the STCs. In addition, a detailed analysis of the connection between STC transport variability and tropical SST anomalies is given. Eventually, in chapter 5, a conclusion of the presented results is drawn and the contribution of this thesis to the current state of research is evaluated. Chapter 5 is complemented by an outlook on work in progress and possible future research.

## 2 Scientific Background

In this chapter, the scientific background necessary to address the scientific questions raised in chapter 1 is provided. A brief introduction to the most fundamental balances that apply in the ocean is given in section 2.1 followed by an overview of the upper ocean circulation in the tropical Atlantic in section 2.2. To understand and distinguish different causes of SST anomalies on various spatial and temporal scales, a summary of the Tropical Atlantic variability is given in section 2.3. Eventually, in section 2.4, the historical development of the description of the Subtropical Cells from the first simple two layer models to the current state of research in observations and general circulation models is provided.

### 2.1 Momentum equation and fundamental balances

Motion in the ocean is governed by a complex set of acting forces. For simplicity, it is best described - under several assumptions and approximations - by the conservation of momentum of a geophysical fluid in a rotating frame. The momentum equation, according to Newtons second law of motion, can be written in its conservative form as (e.g. *Cushman-Roisin and Beckers, 2011*):

$$\frac{\partial \vec{u}}{\partial t} + \vec{u} \nabla \vec{u} + \vec{g} + f \vec{k} \times \vec{u} + \frac{1}{\rho} \nabla p = A_h \nabla_h^2 + A_v \frac{\partial^2 \vec{u}}{\partial z^2} \quad (2.1)$$

(1)    (2)    (3)    (4)    (5)    (6)    (7)

Following standard notation,  $\vec{u}$  is the velocity vector,  $t$  the time,  $\vec{g}$  the gravitational acceleration,  $f$  the Coriolis parameter,  $\vec{k}$  the unit vector,  $\rho$  the reference density,  $p$  the pressure,  $A_h$  the horizontal and  $A_v$  the vertical eddy viscosity coefficient. The individual terms in Equation 2.1 represent (1) the temporal derivative of velocity, (2) the advection of momentum, (3) the gravitational force, (4) the Coriolis force, (5) the pressure gradient force, (6) the horizontal friction force and (7) the vertical friction force. Note that (1) and (2) together form the material derivative of velocity which, in a steady state, becomes zero. Under certain further assumptions this still rather complex horizontal momentum equation 2.1 can be broken down into more simple balances of forces of which the most fundamental ones for this thesis are described in the following.

## Geostrophic balance

Geostrophic balance describes a steady state that is reached when the horizontal velocity is solely governed by a balance of the pressure gradient force (4) and the Coriolis force (5), i.e. neglecting frictional effects, which can be written component-wise for zonal ( $u$ ) and meridional ( $v$ ) velocity (e.g. *Olbers et al.*, 2012):

$$fu_g = -\frac{1}{\rho} \frac{\partial p}{\partial y} \quad (2.2)$$

$$-fv_g = -\frac{1}{\rho} \frac{\partial p}{\partial x} \quad (2.3)$$

The resulting motion is called geostrophic flow ( $\vec{u}_g$ ). Initially, the flow is directed from high to low pressure along the horizontal pressure gradient and is deflected to the right in the northern and to left in the southern hemisphere by the Coriolis force. Once a steady state is reached, the flow follows isobars with the high pressure to the right (left) in the northern (southern) hemisphere. Note that geostrophic balance does not hold close to the equator where the Coriolis force vanishes ( $f = 0$ ). However, under the assumption that the meridional gradient of zonal velocity across the equator is zero, on an equatorial  $\beta$  plane ( $f = \beta y$ ), Equation 2.2 can be differentiated with respect to  $y$  to derive an equatorial geostrophy which is valid for low-frequency flow (*Picaut et al.*, 1990).

About  $2^\circ$  off the equator, horizontal geostrophic flow can be derived from vertical profiles of hydrographic properties (see e.g. *Gray and Riser*, 2014). This approach provides a way to estimate a steady state flow field without depending on measured velocities which are more complicated to obtain than hydrographic properties. The potential density of a water parcel is determined by its conservative temperature, absolute salinity and pressure. By integrating the reciprocal of the potential density (specific density) from a reference depth to the surface the local dynamic height is calculated. Horizontal gradients of dynamic height are then used as horizontal pressure gradients. In combination with the latitude-dependent Coriolis parameter  $f$  and a reference density  $\rho$ , they are sufficient to derive the horizontal components of the absolute geostrophic velocity. To calculate relative geostrophic velocities, the reference level can either be chosen as the interface depth between water masses, where presumably a level of no motion exists or - if available - as a level of known motion derived from velocity data. In the ocean surface and bottom layer, the impact of vertical friction distorts the geostrophic balance. Here, the Ekman balance applies, which is superimposed onto the geostrophic balance in these layers. Throughout this thesis, an important and well-justified assumption is that below the mainly wind-driven surface layer the ocean interior is generally in geostrophic balance (e.g. *Olbers et al.*, 2012).

## Ekman balance

In the ocean surface layer, a balance between the Coriolis force (4) and the vertical gradient of friction (7), the so-called Ekman balance, applies through the momentum transfer of wind stress from the atmosphere into the ocean:

$$fu_E = A_v \frac{\partial^2 v}{\partial z^2} = \frac{1}{\rho} \frac{\partial \tau_y}{\partial z} \quad (2.4)$$

$$-fv_E = A_v \frac{\partial^2 u}{\partial z^2} = \frac{1}{\rho} \frac{\partial \tau_x}{\partial z} \quad (2.5)$$

Here, the vertical friction term in Equation 2.4 and 2.5 (center) is replaced by the vertical gradient of the particular wind stress component of  $\vec{\tau}$ . The resulting horizontal flow is called Ekman flow ( $\vec{u}_E$ ). Due to the rotation of the Earth and the resulting Coriolis force, the wind-driven surface flow is deflected to the right (left) in the northern (southern) hemisphere by about  $45^\circ$  relative to the direction of the wind. With increasing depth the wind-driven flow decreases in magnitude and is continuously deflected further to the right (left) in the northern (southern) hemisphere. The direct impact of wind stress is limited to a layer from the surface down to the so-called Ekman depth ( $H_e$ ) which varies between about 30 – 100 m and depends on the stratification of the surface layer. Vertically integrating from  $H_e$  to the surface yields the Ekman mass transport:

$$M_x = \frac{1}{f} \tau_y \quad (2.6)$$

$$M_y = -\frac{1}{f} \tau_x \quad (2.7)$$

Overall, the net water mass transport described in Equation 2.6 and 2.7 is directed  $90^\circ$  to the right (left) of the wind in the northern (southern) hemisphere. Note that a similar balance between Coriolis force and the vertical gradient of friction also exists in the bottom layer of the oceans. At the equator, the converging easterly trade winds force poleward Ekman transport on both sides of the equator and the resulting water mass divergence drives equatorial upwelling (e.g. [Grodsky et al., 2008](#)).

## Sverdrup balance

The combination of geostrophic and Ekman dynamics describes a balance between Coriolis force (4), pressure gradient force (5) and vertical friction (7), the so-called Sverdrup balance ([Sverdrup, 1947](#)):

$$\rho f u + \frac{\partial p}{\partial y} = \frac{\partial \tau_y}{\partial z} \quad (2.8)$$

$$-\rho f v + \frac{\partial p}{\partial x} = \frac{\partial \tau_x}{\partial z} \quad (2.9)$$

Sverdrup dynamics relate the wind stress curl (z-component of the rotation of the wind stress field) to meridional transport in the ocean interior. Integration from water depth  $-H$  to the surface, while neglecting bottom stress, yields the northward Sverdrup mass transport:

$$M_y = \frac{1}{\beta} \nabla \times \tau \quad (2.10)$$

Note that on a  $\beta$  plane the Coriolis parameter varies with latitude. Usually, the meridional Sverdrup transport is integrated from the eastern boundary westward to derive the total northward transport of the ocean interior at one latitude. However, Sverdrup dynamics are initially not mass balanced. Only when including the horizontal friction term (6) the transport stream lines are closed by a western intensification of meridional transport (accomplished by western boundary currents) and a balance of mass is achieved (*Stommel, 1948; Munk, 1950*). Note that the Sverdrup balance can also be derived from the linearized barotropic vorticity equation for steady motion.

## 2.2 Mean circulation of the upper tropical Atlantic

The mean circulation of the upper tropical Atlantic is generally characterized by a superposition of wind- and density-driven flow components (e.g. *Stramma and Schott, 1999; Schott et al., 2004; Lumpkin and Garzoli, 2005*). Moreover, it is a major crossroad for transport of water masses and can be separated into the following regimes: the wind-driven equatorial and subtropical gyres, the northward return flow of the Atlantic Meridional Overturning Circulation (AMOC) and the Subtropical (*Zhang et al., 2003; Schott et al., 2004*) and Tropical Cells (TCs *Molinari et al., 2003; Perez et al., 2014*).

The mean wind stress in the tropics is dominated by the convergence of the south-easterly and north-easterly trade winds at the mean position of the ITCZ north of the equator. Mean easterly winds force westward surface currents close to the equator (central and southern South Equatorial Current; cSEC and sSEC, respectively) building up an eastward pressure gradient along the equator (see Fig. 1.1). At thermocline level, the eastward flowing Equatorial Undercurrent (EUC), one of the strongest currents in the tropics, compensates the equatorial pressure gradient (e.g. *Metcalf et al., 1962; Brandt et al., 2014; Johns et al., 2014*). North and south of the equator, an alternation of westward and eastward currents is observed (*Schott et al., 2004; Brandt et al., 2008*). In both hemispheres, the most equatorward branches of the subtropical gyres are flowing westward as part of the North Equatorial Current (NEC) in the northern and the Southern Equatorial Current (SEC) in the southern hemisphere (e.g. *Schott et al., 2004*). The SEC furthermore acts as the connection between the Indian and the Atlantic Ocean and is the major supplier of the northward return flow of the AMOC (e.g. *Rühs et al., 2019*). It carries warm water northwestward to the Brazilian coast, where the SEC bifurcates at around  $15^\circ$  S into the equatorward flowing North Brazil Undercurrent (NBUC)



and the poleward flowing Brazil Current (BC) (*Schott et al., 2004*). The NBUC shoals on its northward pathway along the Brazilian coast and crosses the equator within the North Brazil Current (NBC). After crossing the equator, the NBC becomes unstable. Partly it retroflects at around  $5^{\circ}$  N to feed the eastward flowing North Equatorial Countercurrent (NECC), the North Equatorial Undercurrent (NEUC) and the EUC. Partly it sheds northward propagating eddies known as NBC rings north of the retroflexion region as part of the AMOC return flow (*Johns et al., 1998; Garzoli et al., 2004*).

In the meridional direction, the mean zonal wind stress forces poleward Ekman transport in both hemispheres yielding Ekman divergence and equatorial upwelling. At about  $5^{\circ}$  off the equator, a relative convergence of Ekman transport drives the shallow TCs which recirculate tropical water back to the equator (*Molinari et al., 2003; Perez et al., 2014*). In general, Ekman transport is directed poleward from the equator to the subtropical subduction regions, where water masses are largely subducted due to Ekman pumping and are transported back to the equator at thermocline level by the lower limb of the STCs. Note that, subduction also occurs when water masses are advected to regions with a shallower mixed layer depth, where they are cut off from the surface layer and subducted into the thermocline layer (e.g. *Karstensen and Quadfasel, 2002*).

## 2.3 Tropical Atlantic Variability

In the context of this thesis, SST variability due to transport changes associated with the STCs is investigated. STC-driven SST variability could provide an additional contribution to Atlantic SST variability on interannual to decadal time scales and needs to be distinguished from other modes of SST variability and also from the overall global warming trend that, however, appears to be compensated in the eastern equatorial Atlantic (*Nnamchi et al., 2020*). In the Atlantic Ocean, SST variability is apparent on a wide range of temporal and spatial scales, commonly summarized under the term Tropical Atlantic Variability (TAV). This thesis focuses on seasonal to decadal time scales and rather large basin-wide spatial scales. Therefore, processes on intraseasonal time scales are mentioned, but not further considered in the context of this study.

The tropical Atlantic, unlike its Pacific counterpart, is not dominated by one single climate mode such as the El-Niño Southern Oscillation (ENSO) but rather characterized by a strong seasonality modulated by mainly two modes of climate variability (e.g. *Sutton et al., 2000*). These two patterns of ocean-atmosphere variability manifest themselves due to the seasonal migration of the ITCZ and are known as the Atlantic Meridional Mode (AMM or gradient mode) in boreal spring and the Atlantic Zonal Mode (AZM or Atlantic Niño) in boreal summer and show variations on interannual to decadal time scales (*Chang et al., 2006*).

The AZM can be described as temporal and spatial variations of the seasonal cold tongue

of SST along the eastern equatorial Atlantic in boreal summer, when the ITCZ reaches its northernmost position (*Xie and Carton, 2004; Chang et al., 2006*). The seasonal development of the Atlantic cold tongue is followed by the onset of the West African Monsoon (WAM) with a lag of some weeks (*Brandt et al., 2011a*) which is associated with anomalous precipitation over the coast north of the Gulf of Guinea (*Chang et al., 2006; Kushnir et al., 2006*). On interannual time scales the AZM is the dominant mode of variability and, in accordance with the Pacific Ocean, anomalously warm events are referred to as Atlantic Niños, whereas anomalously cold phases are called Atlantic Niñas. An important driver of the AZM is the coupled air-sea Bjerknes feedback that is most active during boreal summer in the Atlantic Ocean (*Keenlyside and Latif, 2007; Jouanno et al., 2017*). However, recent studies provide evidence for a variety of causes such as meridional advection of SST anomalies (*Richter et al., 2013*), equatorial wave propagation (*Foltz and McPhaden, 2010; Lübbecke and McPhaden, 2012; Burmeister et al., 2016*) or net surface heat flux anomalies (*Polo et al., 2015; Nnamchi et al., 2016*).

A positive AMM is associated with an anomalous northward SST gradient driving cross-equatorial northward wind that is strengthening the south-easterlies while weakening the north-easterlies in the southern and northern hemisphere, respectively (*Nobre and Shukla, 1996; Servain et al., 1999; Kushnir et al., 2006*). Wind-induced evaporation and the positive wind-evaporation feedback are suggested to be the main drivers of the meridional mode (*Carton et al., 1996; Chang et al., 2000*). SST anomalies associated with the AMM pattern are known to force anomalous precipitation on both sides of the tropical Atlantic Ocean, especially over Northeast Brazil (*Wallace et al., 1998*). Towards interannual time scales, the AMM becomes less important (*Enfield and Mayer, 1997*) and the dominant mode of tropical Atlantic SST variability are anomalous phases of the AZM (e.g. *Lübbecke et al., 2018*).

On decadal to multidecadal time scales, the Atlantic Multidecadal Oscillation (AMO) - sometimes referred to as Atlantic Multidecadal Variability (AMV) - is the leading mode of Atlantic SST variability (*Martín-Rey et al., 2018*). In its positive phase, the AMO is characterized by anomalously warm SST in the entire North Atlantic Ocean and cold SST anomalies in the southern hemisphere (e.g. *Knight et al., 2005, 2006*). Apart from their connection to rainfall over Northeast Brazil and the Sahel region (*Knight et al., 2006*) and hurricane activity in the tropical Atlantic Ocean (*Goldenberg et al., 2001*), the impact of the AMO on the TAV is still under investigation (*Tokinaga and Xie, 2011*). *Martín-Rey et al. (2018)* noted that a negative AMO can strengthen the AZM in terms of amplitude and western extent and that a surface negative AMO-like signature is found in case of a weakening AMOC. To date, observational studies could not find a link between AMOC and SST variability (e.g. *Lozier et al., 2019*) but several model studies suggest a possible connection. For instance, *Latif et al. (2006)* describe an Atlantic SST response to multidecadal changes of the AMOC that manifests as an interhemispheric SST dipole between the North and South Atlantic. Similarly, *Haarsma et al. (2008)* find a weakening of the seasonal cycle and interannual SST variability in the

eastern tropical Atlantic in case of a simulated collapse of the AMOC. They also note that a weakening of the AMOC resembles the SST pattern of a negative AMO phase.

In addition to internal variability on different time scales, the overall global warming trend marks an external source for SST variability in the tropical Atlantic Ocean (e.g. [Servain et al., 2014](#)). However, recently, [Nnamchi et al. \(2020\)](#) showed that despite the overall global warming trend, SST over the equatorial Atlantic cold tongue region, instead, only increased slightly since the beginning of the satellite era in 1979. They conclude that the warming hole is caused by a shoaling of the equatorial thermocline and damped by turbulent heat flux at the surface. In addition, they analyzed CMIP5 models showing that internal variability has the potential to cause such a warming hole by counteracting external greenhouse gas forcing. However, the relative roles of internal and external variability remain unclear.

As for SST, ocean velocity in the tropical Atlantic Ocean is largely dominated by the seasonal cycle. While meridional velocity, away from the western boundary, is mainly influenced by Tropical Instability Waves at intraseasonal time scales (e.g. [Bunge et al., 2007](#); [Athie and Marin, 2008](#); [Tuchen et al., 2018](#)), variability of the zonal velocity component along the equatorial Atlantic is focused on the semi-annual, annual and interannual (4.5 years) cycle ([Brandt et al., 2016](#); [Claus et al., 2016](#); [Greatbatch et al., 2018](#)) which resemble resonant equatorial basin modes consisting of an equatorial Kelvin wave and Rossby wave ([Cane and Moore, 1981](#)). The interannual fluctuations of equatorial zonal velocity are associated with the equatorial deep jets (EDJs) which are known to impact surface parameters such as SST, wind and precipitation through upward energy propagation ([Brandt et al., 2011b](#)) and potentially contribute to the generation of Atlantic Niños ([Lübbecke et al., 2018](#)).

In conclusion, at the STC-relevant interannual to decadal time scales, tropical Atlantic SST variability is driven by a combination of climate modes which has to be considered when evaluating the impact of STC transport variability on tropical and equatorial SST anomalies.

## 2.4 The ventilated thermocline and the Subtropical Cells

The following section provides the theoretical background and summarizes the current state of research of the mean state and variability of the Atlantic STCs. The dynamic explanation of the ventilated thermocline of [Luyten et al. \(1983\)](#) builds the foundation for the modern understanding of the STCs. It applies to both the Pacific and Atlantic STCs. However, in the Indian Ocean, only one cross-equatorial cell exists that fundamentally differs from the cells in the Pacific and Atlantic (e.g. [Schott et al., 2002b, 2004](#); [Nagura and McPhaden, 2018](#)) and will therefore not be further considered. First, a brief overview of the basic dynamics is given before the state of the art knowledge about the Atlantic and Pacific STCs mean state and variability from model and observational studies is presented.

## 2.4.1 Theoretical background

Within the subtropical gyres, water is subducted into the thermocline layer due to negative wind stress curl and then spreads to the equator along isopycnals governed by Sverdrup dynamics. The concept of the ventilated thermocline was first introduced by [Luyten et al. \(1983\)](#) and has later been explored in a two-layer model in the context of closed shallow meridional overturning cells by [McCreary and Lu \(1994\)](#). The solution of [Luyten et al. \(1983\)](#) provides a dynamic explanation for poorly ventilated oceanic regions, the so-called shadow zones and builds the foundation for the modern understanding of the Subtropical Cells. Here, a brief overview of the theoretical background is provided mainly based on the results of [Luyten et al. \(1983\)](#) and [McCreary and Lu \(1994\)](#) and the review study by [Schott et al. \(2004\)](#).

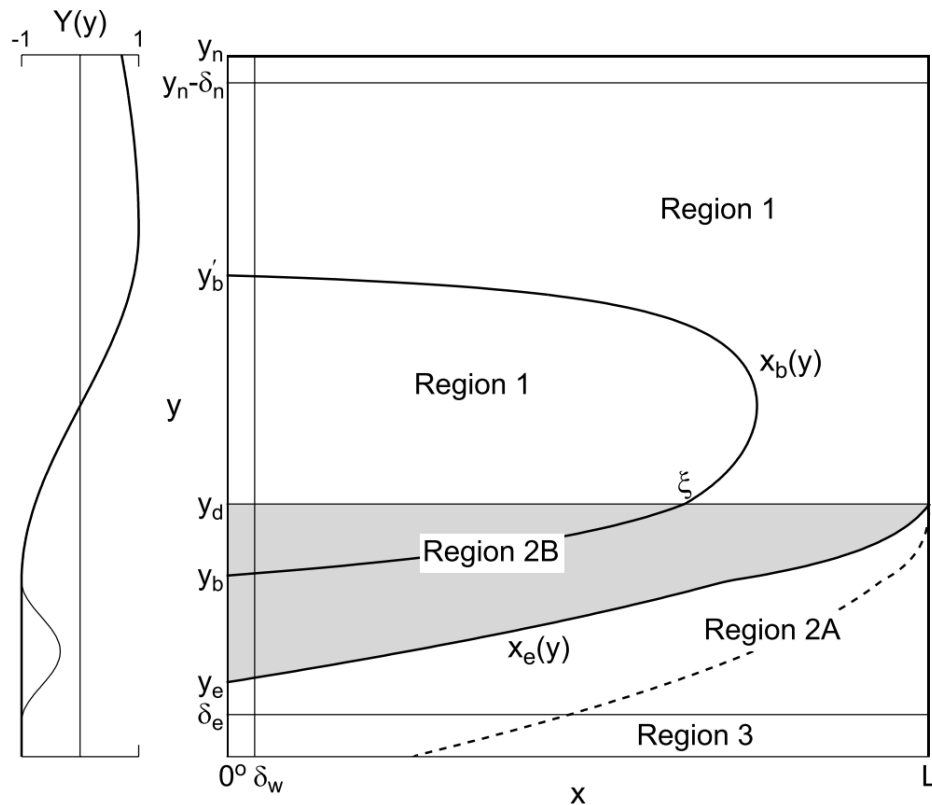


**Figure 2.1:** Schematic representation of the analytical solution of [McCreary and Lu \(1994\)](#) in a rectangular basin with  $y_n = L = 50^\circ$ . The left panel shows two wind profiles,  $Y(y)$ , as a function of latitude with maximum westerlies around  $37.5^\circ$  N and maximum easterlies around  $12.5^\circ$  N. The ITCZ is mimicked by a region of weak easterly winds close to the equator. The parameters chosen for the bifurcation streamline  $x_b$  and the lower-layer characteristic  $x_e$  are  $g'_{12} = 1.96 \text{ cm s}^{-2}$ ,  $g'_{23} = 3.675 \text{ cm s}^{-2}$  for the reduced gravity and  $H_1 = 50 \text{ m}$ ,  $H_2 = 200 \text{ m}$  for the individual layer thickness. More details are provided in the text (Figure adapted from [Schott et al., 2004](#)).

In Fig. 2.1 the analytical solution of the two-layer model of [McCreary and Lu \(1994\)](#) in a

rectangular basin, meridionally bounded by the equator and  $50^\circ$  N, is visualized. The wind forcing (Fig. 2.1, left panel) is zonally uniform and prescribes westerlies in the north and easterlies in the south. The domain is divided into 3 regions. Region 1 and 2 are separated by  $y_d$  which is referred to as the ventilation latitude at  $18^\circ$  N (Luyten *et al.*, 1983). Subduction of water is limited to the north of  $y_d$  in Region 1, where the thickness of the upper layer is kept constant so that the water mass exchange due to Ekman pumping between the two layers is maximum. In Region 2 subduction is prohibited and the layer thickness can adjust freely, whereas in Region 3 close to the equator upwelling is allowed. A series of studies focused on Regions 2 and 3 to analyze the subsurface pathways that subducted water parcels may take if supplying the EUC (Pedlosky, 1987, 1988; Pedlosky and Samelson, 1989; Pedlosky, 1991). Here, the surface layer transport  $M_1$  is determined by the zonal wind stress along  $y_d$  and reduced but not balanced by the geostrophic flow in the same layer. For continuity reasons, the resulting surface layer net transport has to be balanced by equatorward transport  $M_2$  in the lower layer, i.e.  $M_1(y_d) = -M_2(y_d)$ . The surface layer transport at  $y_d$  only depends on the zonal wind stress at  $y_d$  and is not affected by changes of wind stress curl in Region 1 if the wind stress remains unchanged.

In the lower layer, Sverdrup dynamics prescribe a southward transport due to the negative wind stress curl in Region 1. However, in Region 2, equatorward subsurface flow is observed only westward of the streamline  $x_e(y)$ , whereas eastward of it, in Region 2a, a shadow zone with no lower layer flow evolves. Note that the dashed line in Fig. 2.1 represents  $x_e(y)$  for a different set of parameter values ( $g'_{12} = 1.23 \text{ cm s}^{-2}$ ,  $H_2 = 150 \text{ m}$ ) leading to a reduction of the shadow zone. Similarly, in Region 1, only water that is subducted east of the bifurcation streamline  $x_b(y)$  is able to reach the western boundary and also travel further south towards the equator while water subducted west of  $x_b(y)$  recirculates northward at the western boundary. Note that in the real ocean, also interior pathways are observed (e.g. Fratantoni *et al.*, 2000) which, however, appear to be more pronounced in the Pacific Ocean than in the Atlantic Ocean due to the difference in basin width  $L$ .

## 2.4.2 Mean state and variability

Since the model studies by McCreary and Lu (1994) and also by Liu *et al.* (1994), the STCs have increasingly gained attention, especially in the Pacific. In the following, an overview of the findings for the mean state and also for transport variability associated with the horizontal branches of the Atlantic STCs is provided. In the Atlantic, the north- and south-easterly wind convergence in the equatorial region forces poleward Ekman transport in both hemispheres. The Ekman divergence between  $10^\circ$  N and  $10^\circ$  S is on the order of  $20 - 25 \text{ Sv}$  (e.g. Schott *et al.*, 2004) and can be well estimated by satellite wind data. The rather symmetric Ekman divergence is reduced but not exceeded by geostrophic convergence in the surface layer. At

thermocline level, estimates of the equatorward geostrophic transport are hindered by sparse hydrographic observations. Naturally, the meridional pathways of the horizontal branches are rather complex since they are distorted by the equatorial and tropical surface and subsurface current system and interaction with zonally propagating Rossby waves (e.g. *Gu and Philander, 1997; Lee and Fukumori, 2003; Capotondi et al., 2005*). In the schematic view of the Atlantic STC components by *Schott et al. (2004)* (Fig. 1.1) three possible pathways for subducted water parcels are visualized. Only water parcels that reach the equator along the western boundary or through the interior of the basin, participate in the water mass exchange associated with the STCs (*Malanotte-Rizzoli et al., 2000*). The third pathway is the recirculation at the western boundary. Recirculation is mainly observed poleward of the bifurcation points of the South Equatorial Current (SEC) and of the North Equatorial Current (NEC). Therefore, STC transport estimates are typically derived along latitudes that are equatorward of the bifurcation zones. However, at around  $5^\circ$  off the equator a relative Ekman convergence causes local Ekman pumping and drives additional shallow overturning circulations, the Tropical Cells (TCs) (*Molinari et al., 2003; Perez et al., 2014*). Since the TCs are superimposed on the STCs at low latitudes, STC estimates must be derived poleward of the TCs in order to isolate meridional transport associated with the STCs (e.g. *Zhang et al., 2003; Rabe et al., 2008*). Hence, in each hemisphere, an STC estimate must be realized between the TCs and the bifurcation of the NEC/SEC.

In a temporal mean state, the Atlantic STCs, in contrast to the Pacific STCs, exhibit an interhemispheric asymmetry of equatorward transport with only about one third of the overall thermocline layer transport convergence originating from the northern hemisphere (*Zhang et al., 2003; Hazeleger and Drijfhout, 2006*). This asymmetry is predominantly caused by the superposition of the northward return flow of the AMOC on the STCs along the western boundary (*Fratantoni et al., 2000*). In their model study, *Fratantoni et al. (2000)* show that a wind-only forcing generates rather symmetric cells, as in the Pacific Ocean. In contrast, in their more realistic experiment including winds and meridional overturning, the observed asymmetric distribution is evident. The AMOC supports the northward transport of the southern hemisphere STC and at the same time suppresses southward transport of the northern STC. In addition, in each hemisphere, a zonal asymmetry between equatorward transport along the western boundary and through the interior evolves. The presence of the mean ITCZ in the northern hemisphere creates an area of relatively high potential vorticity which forces subducted water with relatively low potential vorticity to a westward detour on their equatorward pathway (e.g. *Jochum and Malanotte-Rizzoli, 2001*). Hence, interior transport in the northern hemisphere is largely prevented and most equatorward transport is observed close to the western boundary (*Zhang et al., 2003*). Overall, observational estimates account for about  $5\text{ Sv}$  of equatorward transport from the northern hemisphere and  $16\text{ Sv}$  from the southern hemisphere (*Zhang et al., 2003*) of which  $12\text{ Sv}$  ( $6\text{ Sv}$  as part of the AMOC) reach the equator along the western boundary in the southern hemisphere and  $3\text{ Sv}$  along the northern hemisphere

western boundary which is comparable to model results (*Fratantoni et al.*, 2000; *Hazeleger and Drijfhout*, 2006). To date, the study of *Zhang et al.* (2003) marks the only observation-based analysis of the mean Atlantic STCs and serves as an important reference throughout this thesis. So far, an accurate estimate of the mean state of the Atlantic STCs is complicated by sparse observations. As a consequence, in the Atlantic, STC transport time series analysis has been limited to general circulation (*Hüttl and Böning*, 2006) and data assimilation model studies (*Rabe et al.*, 2008).

However, for the Pacific Ocean, only *McPhaden and Zhang* (2002) derived an STC transport time series based on hydrographic observations. They were able to derive decadal averages of anomalous thermocline layer transport convergence covering a period of about 50 years. In the Pacific, especially the western boundary is characterized as a region of insufficient data coverage and therefore *McPhaden and Zhang* (2002) could only relate the STC interior transport component to tropical SST anomalies. They observed a clear anti-correlation between STC interior transport and SST anomalies concluding that a stronger subsurface STC branch coincides with lower SST in the tropics. At decadal time scales, several further studies supported the finding of *McPhaden and Zhang* (2002) for the Pacific STCs (*Nonaka et al.*, 2002; *McPhaden and Zhang*, 2004; *Zhang and McPhaden*, 2006; *Lübbecke et al.*, 2008; *Farneti et al.*, 2014). The Pacific STCs are further suggested to respond to ENSO as they show enhanced meridional transport during La-Niña and weaker meridional transport during El-Niño (*Zilberman et al.*, 2013).

The favored mechanism for how the STCs modulate tropical SST anomalies at decadal time scales was proposed by *Kleeman et al.* (1999). It describes how changes in thermocline layer equatorward transport are able to modulate SST while the temperature of the subducted water is kept constant ( $v'\bar{T}$  mechanism). Another hypothesized mechanism ( $\bar{v}T'$ ) includes the propagation of subducted temperature anomalies towards the equator with a relatively constant equatorward transport (*Gu and Philander*, 1997). However, this mechanism did not achieve comparable acceptance. For instance, neither *Schneider et al.* (1999) nor *Hazeleger et al.* (2001) could observe a significant propagation of subtropical temperature anomalies into the equatorial regions. In the Atlantic Ocean no such relation has been shown yet. Therefore, the results by *McPhaden and Zhang* (2002) raise the question whether a comparable connection can be found in the Atlantic and if so which mechanism could be at work.

Since *McPhaden and Zhang* (2002) could only resolve the interior part of the thermocline layer transport convergence and relate a weakening to an increase in tropical SST, several model studies focused on the relation between western boundary and interior transport anomalies. *Lee and Fukumori* (2003) and *Capotondi et al.* (2005) show that in both hemispheres Pacific STC transport anomalies through the western boundary and the interior are generally anti-correlated. This is in contrast to the mean state in which both the western boundary and interior thermocline layer transport is equatorward in both hemispheres. These transport anomalies are partly compensating each other at both interannual and decadal time scales.

[Capotondi et al. \(2005\)](#) attribute this see-saw relation to baroclinic ocean adjustment due to large-scale off-equatorial wind stress curl changes.

In the Atlantic, predominantly the study of [Rabe et al. \(2008\)](#) showed STC-related transport variability in the data assimilation model GECCO. They conclude that at time scales longer than  $\sim 5$  years the surface layer branches lead changes in the EUC as the upwelling branch of the STCs which are then followed by a response in the thermocline layer branches. The so-called STC loop is only observed at longer time scales and the study of [Rabe et al. \(2008\)](#) sets an important reference for the analysis of STC transport variability in the Atlantic Ocean.



# 3 The mean Atlantic Subtropical Cells inferred from observations

To date, the mean transport associated with the Atlantic STCs has only been derived once based on sparse observations (*Zhang et al., 2003*). With the start of the Argo program about 20 years ago, the hydrographic data density of the world oceans has increased fundamentally and facilitates an updated estimate of the mean Atlantic STCs. In this chapter, a combination of Argo float data (as available at the time of publication), ship sections, reanalysis and satellite data is used to first localize and then quantify the horizontal transport branches of the Atlantic STCs. The results of this chapter provide new detailed insights into the vertical and horizontal structure of the Atlantic STCs and build the foundation of the time series analysis carried out in chapter 4.

The manuscript was published in *Journal of Geophysical Research: Oceans* in November 2019.

---

**Tuchen, F. P.**, Lübbecke, J. F., Schmidtko, S., Hummels, R., and Böning, C. W. (2019): The Atlantic Subtropical Cells Inferred From Observations, *Journal of Geophysical Research: Oceans*, 124, 7591-7605, <https://doi.org/10.1029/2019JC015396>

---

The candidate designed the study and carried out the analysis of observational, reanalysis and satellite data products, produced all figures and authored the manuscript from the first draft to the final published version.

## Abstract

The Atlantic Subtropical Cells (STCs) are shallow wind-driven overturning circulations connecting the tropical upwelling areas to the subtropical subduction regions. In both hemispheres, they are characterized by equatorward transport at thermocline level, upwelling at the equator, and poleward Ekman transport in the surface layer. This study uses recent data from Argo floats complemented by ship sections at the western boundary as well as reanalysis products to estimate the meridional water mass transports and to investigate the vertical and horizontal structure of the STCs from an observational perspective. The seasonally varying depth of meridional velocity reversal is used as the interface between the surface poleward flow and the thermocline equatorward flow. The latter is bounded by the  $26.0 \text{ kg m}^{-3}$  isopycnal at depth. We find that the thermocline layer convergence is dominated by the southern hemisphere water mass transport ( $9.0 \pm 1.1 \text{ Sv}$  from the southern hemisphere compared to  $2.9 \pm 1.3 \text{ Sv}$  from the northern hemisphere) and that this transport is mostly confined to the western boundary. Compared to the asymmetric convergence at thermocline level, the wind-driven Ekman divergence in the surface layer is more symmetric, being  $20.4 \pm 3.1 \text{ Sv}$  between  $10^\circ \text{ N}$  and  $10^\circ \text{ S}$ . The net poleward transports (Ekman minus geostrophy) in the surface layer concur with values derived from reanalysis data ( $5.5 \pm 0.8 \text{ Sv}$  at  $10^\circ \text{ S}$  and  $6.4 \pm 1.4 \text{ Sv}$  at  $10^\circ \text{ S}$ ). A diapycnal transport of about  $3 \text{ Sv}$  across the  $26.0 \text{ kg m}^{-3}$  isopycnal is required in order to maintain the mass balance of the STC circulation.

## Plain Language Summary

The Atlantic Subtropical Cells (STCs) are shallow wind-driven overturning circulations connecting the tropics to the subtropical regions within the upper 300 m. In both hemispheres, they are characterized by equatorward transport at subsurface level and poleward transport in the surface layers. They are closed by upwelling at the equator and subduction in the subtropics. STCs are suggested to impact sea-surface temperature variability in tropical upwelling regions thereby influencing, for example, precipitation patterns. The boundary between the two branches is approximated by the depth at which the meridional velocity reverses. The lower boundary of the deep equatorward branch is defined by an isoline of potential density. We find that at subsurface level, the equatorward branches converge in the tropics with more transport coming from the southern hemisphere. At the surface, a more symmetric divergence of water mass is observed in the tropics. The surface layers are also influenced by geostrophic transport generally counteracting the wind-driven divergence. In total, the net surface divergence and the subsurface convergence yield a residual. It is suggested that this water mass volume deficit originates from below the STCs and enters the subsurface layers in the tropics where it is lifted to the surface.

## 3.1 Introduction

The subduction zones in the oceanic subtropical gyres are linked to the tropics by shallow meridional overturning circulations confined to the upper approximately 300 m: the Subtropical Cells (STCs). The STCs are driven by poleward Ekman transport within the surface layer in the tropics, forming the equatorial divergence. In the subtropics, Ekman pumping causes subduction of water masses to thermocline level. From here, geostrophic transport brings the water back toward the equator along isopycnal surfaces. In the tropics, equatorial upwelling due to Ekman divergence or coastal upwelling forms the last branch of the STCs (e.g. [Liu et al., 1994](#); [McCreary and Lu, 1994](#); [Schott et al., 2004](#)).

The STCs upwell cool subsurface waters and thereby maintain the tropical thermocline ([Schott et al., 2004](#)). Variations in the mean water mass transports due to STC dynamics enable advection of hydrographic and/or transport anomalies from the subtropics to the equator. Hence, STCs are suggested to influence equatorial sea-surface temperature (SST) variability on inter-annual to decadal time scales in the tropical Atlantic Ocean via two different processes ([Schott et al., 2004](#)). In the first process, temperature anomalies are subducted in the subtropics and transported at the thermocline level toward the equatorial or eastern tropical upwelling regions impacting tropical SST ([Gu and Philander, 1997](#)). The second process describes an anomalous equatorward thermocline transport that changes the amount of thermocline water entering the upwelling regions rather than its properties ([Kleeman et al., 1999](#)). For the Pacific Ocean, the second process has been shown to play an active role in both models and observations, resulting in pronounced SST anomalies in the eastern equatorial upwelling area ([Farneti et al., 2014](#); [Lübbecke et al., 2008](#); [McPhaden and Zhang, 2002, 2004](#)).

Despite the simplified model of overturning described above, STCs are far from being two-dimensional and exhibit rather complex pathways. Subduction in the subtropical Atlantic generally occurs in the eastern parts of the basins driven mainly by Ekman pumping. From there, subducted water flows westward and equatorward (e.g. [Lazar et al., 2002](#)) while zonal currents distort their pathways. [Malanotte-Rizzoli et al. \(2000\)](#) showed that for subducted water masses, three different pathways exist between the subtropics and tropics. First, thermocline water can reach the equatorial upwelling zones on interior routes. Second, depending on the latitude of subduction, thermocline water can reach the western boundary where it is entrained in the western boundary current and travels equatorward. Third, thermocline water that reaches the western boundary too far south in the southern hemisphere or too far north in the northern hemisphere is recirculated poleward within the subtropical gyre and does not participate in the subtropical-tropical exchange. These theoretical pathways are modified in the northern hemisphere by the presence of the Intertropical Convergence Zone (ITCZ) between  $5 - 15^\circ$  N. Upwelled waters within the ITCZ have a higher potential vorticity (PV) and are more stratified than subducted waters at the same density range. Thermocline water is forced to circumvent the PV barrier which extends roughly from  $15^\circ$  N in the central eastern part

of the basin to  $10^{\circ}$  N near the western boundary (*Harper, 2000*) causing thermocline water on equatorward pathways to take a westward detour (*Zhang et al., 2003*) largely hindering interior pathways in the northern hemisphere.

The interhemispheric asymmetry is increased by the return flow of the Atlantic Meridional Overturning Circulation (AMOC) superimposed upon the Atlantic STCs which is particularly apparent at the western boundary (e.g. *Fratantoni et al., 2000; Hazeleger and Drijfhout, 2006*). In the southern tropical Atlantic, the upper ocean return flow of the AMOC is focused in the northward flowing North Brazil Undercurrent (NBUc) which loses its undercurrent character on its equatorward pathway after being augmented by the shallower inflow of the South Equatorial Current (*Schott et al., 2004*). It then continues as the surface-intensified North Brazil Current (NBC) crossing the equator and transporting warm water northward. Hence, the upper ocean return flow of the AMOC strengthens the southern hemisphere STC while counteracting southward thermocline transports in the northern hemisphere STC (*Schott et al., 2004*) along the western boundary. As a consequence, the Equatorial Undercurrent (EUC) is predominantly fed by thermocline water of South Atlantic origin (*Fratantoni et al., 2000; Harper, 2000; Hazeleger et al., 2003; Liu et al., 1994; Tsuchiya, 1986*) leading to an asymmetry of origins of water masses within the density range of the equatorward branch (*Peña-Izquierdo et al., 2015; Oschlies et al., 2018*). Therefore, central and intermediate waters in the tropical North Atlantic are mainly ventilated by waters originating in the South Atlantic. Analogously, the Indonesian throughflow is responsible for a similar asymmetry of the STCs in the Pacific Ocean. There, an estimated 80 – 90 % of EUC water originates in the southern hemisphere (*Kuntz and Schrag, 2018; Schott et al., 2004*) which is comparable to Atlantic Ocean estimates by *Fratantoni et al. (2000)* that 85 % of the water masses transported by the EUC in the western Atlantic originate in the South Atlantic.

Most of the STC characteristics described so far have been derived from model studies. Observational estimates of transport values for the individual branches of the Atlantic STCs (thermocline layer transport and surface layer transport in both hemispheres) have been provided by *Zhang et al. (2003)* based on five decades of hydrographic data mainly from the World Ocean Database and the World Ocean Circulation Experiment. Their calculations showed that on average, 5 Sv ( $= 10^6 \text{ m}^3 \text{ s}^{-1}$ ) northern hemisphere waters (2 Sv interior and 3 Sv western boundary) and 10 Sv southern hemisphere waters (4 Sv interior and 6 Sv western boundary) reach the equator. Aside from *Zhang et al. (2003)*, observational efforts studying the Atlantic STCs have been rare. However, numerical model studies such as *Hazeleger and Drijfhout (2006)* estimate STC transports from a high-resolution model to be more than a factor of 2 smaller than the observational estimates (4 Sv from the south and 1.5 Sv from the north). Moreover, *Fratantoni et al. (2000)* use an eddy-resolving ocean circulation model to design different model experiments with and without a meridional overturning circulation. Their results show that the combination of wind and MOC forcing yields an asymmetric thermocline convergence of 14 Sv southern hemisphere and 2 Sv northern hemisphere contribution while their

wind-only experiment shows a symmetric thermocline convergence among hemispheres of 8 Sv from the southern hemisphere and 7 Sv from the northern hemisphere. However, the asymmetry between interior transport and western boundary transport remains. In addition, the transports of the solutions of the wind+MOC forced run are a superposition of the transports of the wind-only and MOC-only runs. The linearity does not hold for the mesoscale variability which is greatly enhanced in the MOC including runs. Other studies further emphasize how the choice of wind stress forcing influences the overall circulation patterns and the exchange windows in general circulation models. For instance, [Inui et al. \(2002\)](#) and [Lazar et al. \(2002\)](#) both show that a stronger wind stress forcing causes the interior exchange windows to be of smaller extent. However, the discrepancy in STC transports between model studies and [Zhang et al. \(2003\)](#) emphasizes the need of further studies based on observations.

When estimating their transport, STCs have to be distinguished from the tropical cells (TCs) which are shallow tropical overturning circulations close to equator. The latitudinal extent of the TCs is approximately  $\pm 3.5^\circ$  off the equator (e.g. [Lu et al., 1998](#)) suggesting that the TCs mainly recirculate tropical water masses and do not participate in the subtropical-tropical water mass exchange. However, at equatorial latitudes, they superimpose upon the STCs and therefore zonal sections of thermocline equatorward transport associated with the STCs should be calculated poleward of the TCs. The present study focuses on the Atlantic STCs, and in the following, any use of the abbreviation STC will refer to the cells of the Atlantic Ocean, unless otherwise noted. Observations in the Atlantic Ocean have multiplied — especially due to the Argo program — since the transport estimates of [Zhang et al. \(2003\)](#). Furthermore, the enhanced spatial and temporal coverage of the last two decades calls for an updated observational estimate of the STC transports to allow for a more detailed investigation of their structure.

This study is structured as follows. First, the different data sets are described in section 3.2. Section 3.3 provides a summary of the methods used to calculate the individual STC branches and their error estimate. Section 3.4 describes the results which are divided into thermocline transports and surface transports. In section 3.5 the presented results are summarized and discussed.

## 3.2 Data

### 3.2.1 Argo Climatological Data

Since its start in 2000, the Argo program has grown into a global array of nearly 4,000 profiling floats. This coverage has been sustained for more than a decade, providing temperature and salinity profiles in the upper 2000 m (Fig. 3.1). Overall, more than 160,000 Argo profiles are available between  $20^\circ$  S and  $20^\circ$  N in the Atlantic for the time period of 2004 to 2016. This is approximately the same number of hydrographic profiles that [Zhang et al. \(2003\)](#) used for

a period spanning five decades, though their latitudinal range (40° S to 50° N) is more than twice the range analyzed here (see their Fig. 1), indicating a data density half of what is available for this study.

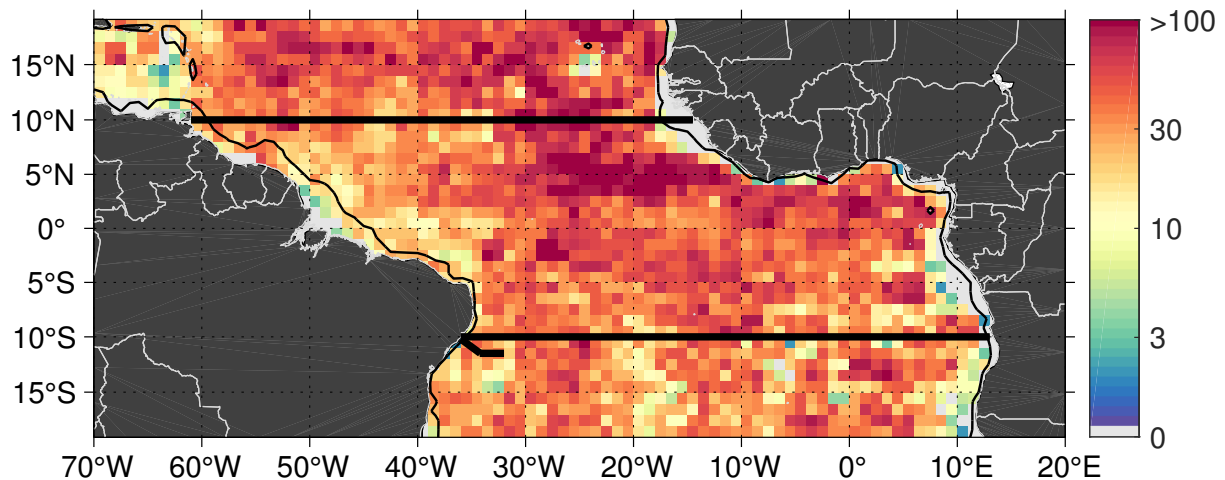


**Figure 3.1:** Number of Argo profiles (delayed mode) within horizontal boxes of  $(1^\circ)^2$  between 2004 and 2016. Note the logarithmic color scale. Zonal sections at 10° N, 10° S and a repeated ship section at the western boundary are marked (thick black lines). The 1000 m isobath from the ETOPO1 bathymetry (Amante and Eakins, 2009) is superimposed (black contours).

Within the framework of this study, monthly geostrophic transports are calculated from the 2017 version of the Roemmich-Gilson Argo climatology (from here on called RG-clim; Roemmich and Gilson, 2009). The updated version of the RG-clim is based on a similar analysis method as in Roemmich and Gilson (2009) and available for the time period from 2004 to 2016 providing (a) a climatological mean and (b) monthly anomalies of temperature and salinity both mapped on a  $1^\circ \times 1^\circ$  grid and on 58 depth levels. For a detailed description of how the RG-clim is derived, the mapping methods and the additional quality control criteria applied to the available Argo profiles, see Roemmich and Gilson (2009).

### 3.2.2 Western Boundary Ship Section

The western boundary is generally a region of sparse Argo float coverage (Fig. 3.1). However, it is a key region for equatorward STC transports. In order to better resolve the southern hemisphere western boundary, five individual sections of hydrographic and acoustic Doppler current profiler (ADCP) measurements are used to construct mean sections of conservative temperature, absolute salinity, and alongshore/meridional velocity. All cruises were carried out with the RV Meteor in July 2013 (M98), May 2014 (M106), October 2015 (M119), September 2016 (M130), and March 2018 (M145). Shipboard ADCP data are combined with lowered ADCP profiles at hydrographic stations to construct full-depth velocity sections (e.g. Hummels *et al.*, 2015).

The mean section is an update of Hummels *et al.* (2015) but only implements sections from

2013 onward. All cruise tracks followed  $11.5^{\circ}$  S between  $32^{\circ}$  W and  $34.15^{\circ}$  W before turning northwestward toward the Brazilian coast where the sections end at  $36^{\circ}$  W and  $10.2^{\circ}$  S (Fig. 3.1). Alongshore velocity from the cross-shore ship section is combined with meridional velocities from the zonal part of the ship section.

Shipboard velocity measurements used in this study are in good agreement with the mean alongshore velocity section derived from moored observations along  $11.5^{\circ}$  S (e.g. [Hummels et al., 2015](#)). Variability on seasonal time scales has been estimated by [Schott et al. \(2005\)](#) for an earlier period of the mooring array. They found a seasonal cycle of NBUC transport with a range of about  $4Sv$  between a maximum in July and a minimum in October/November which is most likely covered by the somewhat evenly distributed sections (March, May, July, September, and October). This encouraged us to use the spatially high-resolved mean ship section for further analysis.

### 3.2.3 Monthly Isopycnal and Mixed-layer Ocean Climatology

The Monthly Isopycnal and Mixed-layer Ocean Climatology (MIMOC; [Schmidtke et al., 2013](#)) provides hydrographic climatological monthly means based on Argo profiles, shipboard, and ice-tethered CTD data and profiles archived in the World Ocean Database. Climatological profiles are mapped with a horizontal resolution of  $(0.5^{\circ})^2$  and on 81 pressure levels between 0 and 1950 dbar. MIMOC is intended to represent the modern state of the world oceans meaning that recent observations are emphasized. However, in regions with poor data coverage, the climatology relaxes to historic data from as early as the 1970s. Due to the incorporation of CTD data, MIMOC can provide useful insights inshore of the 1000 m isobath where Argo profiles are absent.

### 3.2.4 Ocean Reanalysis 4

Thermocline transport estimates are evaluated by comparison of observational data with the ECMWF-Ocean Reanalysis 4 (ORA-S4; [Balmaseda et al., 2013](#)). ORA-S4 has a horizontal resolution of  $(1^{\circ})^2$  and covers a time period between 1958 and 2017 of which we use hydrographic and velocity data between 2000 and 2017. In addition to potential temperature and practical salinity profiles which are converted into conservative temperature and absolute salinity profiles and from which geostrophic transports are calculated, ORA-S4 further provides zonal and meridional velocity data on 42 depth levels. Absolute velocity data are used here for comparison and to determine the depth at which the meridional velocity reverses from poleward at the surface to equatorward at thermocline depth. This depth is taken to represent the interface between the upper and the lower STC branches as described in section 3.4.1.

### 3.2.5 Wind Products

Surface transports of the STCs are associated with poleward Ekman transport. In order to estimate the meridional Ekman transport, wind stress data from several products are used. The Advanced Scatterometer (ASCAT) satellite observations provide daily maps of surface wind speed with a horizontal resolution of 25 km for the time period between 2007 and 2018. Satellite observations from ASCAT are complemented by the NCEP/NCAR Reanalysis I which provides 6-hourly wind speed data on a  $(2.5^\circ)^2$  horizontal grid and by JRA-55 6-hourly wind speed data on a  $(0.5^\circ)^2$  grid from which the zonal surface wind stress ( $\tau_x$ ) is calculated via the Bulk formula:

$$\tau_x = \rho_a * c_d * u^2 \quad (3.1)$$

using a reference density  $\rho_a = 1.22 \text{ kg m}^{-3}$ , a drag coefficient  $c_d = 0.0013$  (used e.g. in [Kopte et al., 2018](#)) and the zonal surface wind speed  $u$ .

## 3.3 Methods

### 3.3.1 Thermocline Transport

In a first step, the gridded hydrographic data (available either as in situ temperature or potential temperature and practical salinity) are converted into conservative temperature (CT) and absolute salinity (SA) following the definitions of the TEOS-10 ([McDougall and Barker, 2011](#)). From CT and SA, profiles of dynamic height are calculated at each longitude of the zonal sections at  $10^\circ \text{ N}$  and  $10^\circ \text{ S}$ . These latitudes are chosen because of their sufficient distance from the TCs close to the equator on the one side and to the subtropical subduction zones on the other side. In addition, we can combine estimates at  $10^\circ \text{ S}$  with the close-by repeated ship section at  $11.5^\circ \text{ S}$ . All thermocline water associated with the STCs has to pass these latitudes on either interior or western boundary pathways. Zonal sections of dynamic height are used to derive zonal pressure gradients ( $p_x$ ) from which relative meridional geostrophic velocities ( $v_g$ ) perpendicular to the zonal sections are calculated:

$$-f(y) v_g = -\frac{1}{\rho_0} p_x \quad (3.2)$$

where  $f$  represents the Coriolis parameter at the specific latitude ( $y$ ) of the section and  $\rho_0$  a reference density. Absolute geostrophic velocities are inferred with a reference level based on the time-mean meridional displacement of Argo floats at their parking level derived from the YoMaHa'07 data set ([Lebedev et al., 2007](#)). The majority of the Argo floats drift at a deep parking level of around 1000 dbar. Consequently, absolute geostrophic velocities derived from the RG-clim and MIMOC are referenced to this level of known motion. Note that absolute velocities at 1000 dbar from ORA-S4 are indistinguishable from zero. Therefore, geostrophic



velocities from ORA-S4 are inferred with an assumed reference level of no motion at 1000 dbar. CT and SA are used to calculate mean sections of potential density along 10° N and 10° S. Equatorward transports from geostrophic and absolute velocities are calculated between an upper boundary and a lower boundary which is discussed in detail below in section 3.4.1. The layer thickness ( $\Delta z$ ) between these boundaries at each longitude, latitude, and time step, the zonal grid space ( $\Delta x$ ), and the monthly meridional (geostrophic or total) velocity ( $v$ ) within the layer are needed to calculate the monthly meridional (geostrophic or total) volume transport ( $T$ ) at each longitude ( $x$ ), latitude ( $y$ ), and time step ( $t$ ):

$$T(x, y, t) = \Delta x \Delta z(x, y, t) v(x, y, t) \quad (3.3)$$

The estimate of transport uncertainties in thermocline layer and surface layer transport (shown in Tabs. 3.1 and 3.2) is given by the temporal standard deviation at each longitude along the zonal sections at 10° N and 10° S. While the transport is accumulated along zonal sections by summing from east to west, the uncertainties of the cumulative transport estimates ( $\epsilon$ ) are calculated by using the rules of error propagation:

$$\epsilon = \sqrt{\sum_i \sigma_i^2} \quad (3.4)$$

where  $\sigma_i$  is the temporal standard deviation at longitude  $i$ .

### 3.3.2 Surface Transport

The poleward surface transport of the STCs is calculated using wind stress data derived from several wind products (see section 3.2.5): ASCAT, JRA-55, and NCEP/NCAR Reanalysis I. Under the assumption that the poleward surface transport associated with the upper branch of the STCs is driven by the meridional Ekman transport, the surface transport ( $T_E$ ) is defined by:

$$T_E(x, y, t) = -\frac{1}{\rho_0} \frac{\tau_x(x, y, t)}{f(y)} \Delta x \quad (3.5)$$

where  $\tau_x$  represents the zonal wind stress for a given horizontal cell ( $\Delta x$ ). Surface transports are calculated for each time step ( $t$ ) before averaging over time.

## 3.4 Results

### 3.4.1 Thermocline Transports

The STCs are divided into a subsurface equatorward and a surface poleward branch. In the following, the transports of the equatorward branches are estimated individually along two zonal

sections at  $10^\circ$  N and  $10^\circ$  S. Hydrographic properties, CT and SA, along these sections are presented from the RG-clim (Figs. 3.2a-d). They show the tilted thermocline/halocline/pycnocline toward the east of the basin, which is steeper in the southern hemisphere, as well as a fresh water lens at  $10^\circ$  N (Fig. 3.2c) close to the western boundary that is most likely associated with the Amazon and Orinoco river outflow a few degrees to the south. In the central and eastern part of the northern section, the mean position of the ITCZ leads to decreased sea surface salinity and a subsurface salinity maximum. The southern section generally exhibits higher salinity in the surface layer and shows a subsurface maximum close to the western boundary.

Zonal sections of CT and SA are used to calculate meridional geostrophic velocity across  $10^\circ$  N and  $10^\circ$  S (Figs. 3.2e-f). Between the surface and approximately the  $26.0 \text{ kg m}^{-3}$  isopycnal, the meridional geostrophic flow is mainly equatorward except for at the eastern boundary where both sections reveal poleward flow. At  $10^\circ$  S, the western boundary shows the geostrophic part of the equatorward flowing NBUC with maximum geostrophic velocities of about  $0.2 \text{ m s}^{-1}$ . This is about half the magnitude of absolute velocities measured by [Hummels et al. \(2015\)](#). Since western boundary currents are mainly in geostrophic balance, this difference likely indicates an underestimation of the NBUC by the RG-clim. On its equatorward path, the NBUC is augmented by the shallower inflow of the low-latitude South Equatorial Current and continues northward as the surface intensified NBC (e.g. [Schott et al., 1998](#)). The NBC is poorly sampled at the northern section due to sparse data coverage (Fig. 3.1). Potential consequences of the deficient representation of the NBC for the transport estimates of the STCs are discussed below in section 3.5. Nevertheless, the southward recirculation of the NBC between  $50 - 55^\circ$  W at  $10^\circ$  N is well captured.

In order to calculate equatorward volume transports associated with the STCs, first, the vertical extent of the layer in which the lower branches of the STCs reside has to be defined. This layer is called the thermocline layer. First, we focus on the lower boundary.

In general, the vertical structure of meridional geostrophic transports per  $0.2 \text{ kg m}^{-3}$  density bin agrees well for the different geostrophic products (Fig. 3.3). At  $10^\circ$  N, the deepest layers below  $26.0 \text{ kg m}^{-3}$  show poleward transport in all products, with a peak at about  $26.5 \text{ kg m}^{-3}$  in the RG-clim and slightly deeper in ORA-S4 and MIMOC indicating the interior northward pathway of the thermohaline circulation (Fig. 3.3a). Generally, the sign of transport changes from poleward to equatorward right above  $26.0 \text{ kg m}^{-3}$ . Hence, the  $26.0 \text{ kg m}^{-3}$  isopycnal is chosen as the lower boundary of the northern STC. Total meridional transport derived from absolute velocity data from ORA-S4 includes the poleward Ekman transport in the surface layer and therefore differs from the geostrophic transports above a certain isopycnal surface which can be seen as a proxy for the zonal mean potential density equivalent of the annual mean Ekman depth. At  $10^\circ$  S, the vertical structure of meridional transport is basically mirroring the structure of the northern section (Fig. 3.3b). Below  $26.0 \text{ kg m}^{-3}$ , poleward transport represents the recirculation of the South Equatorial Undercurrent ([Stramma and England, 1999](#)).

Northward transport below  $26.5 \text{ kg m}^{-3}$  as seen in RG-clim and MIMOC indicates the northward flow of Antarctic Intermediate Water which is not seen in ORA-S4 transports. Closer to the surface and above  $26.0 \text{ kg m}^{-3}$ , equatorward transport is observed with peak values between  $23.5 - 25.0 \text{ kg m}^{-3}$ . Analogously to the northern section, we choose the  $26.0 \text{ kg m}^{-3}$  isopycnal as the lower boundary of the equatorward branch of the STC at  $10^\circ \text{ S}$ .

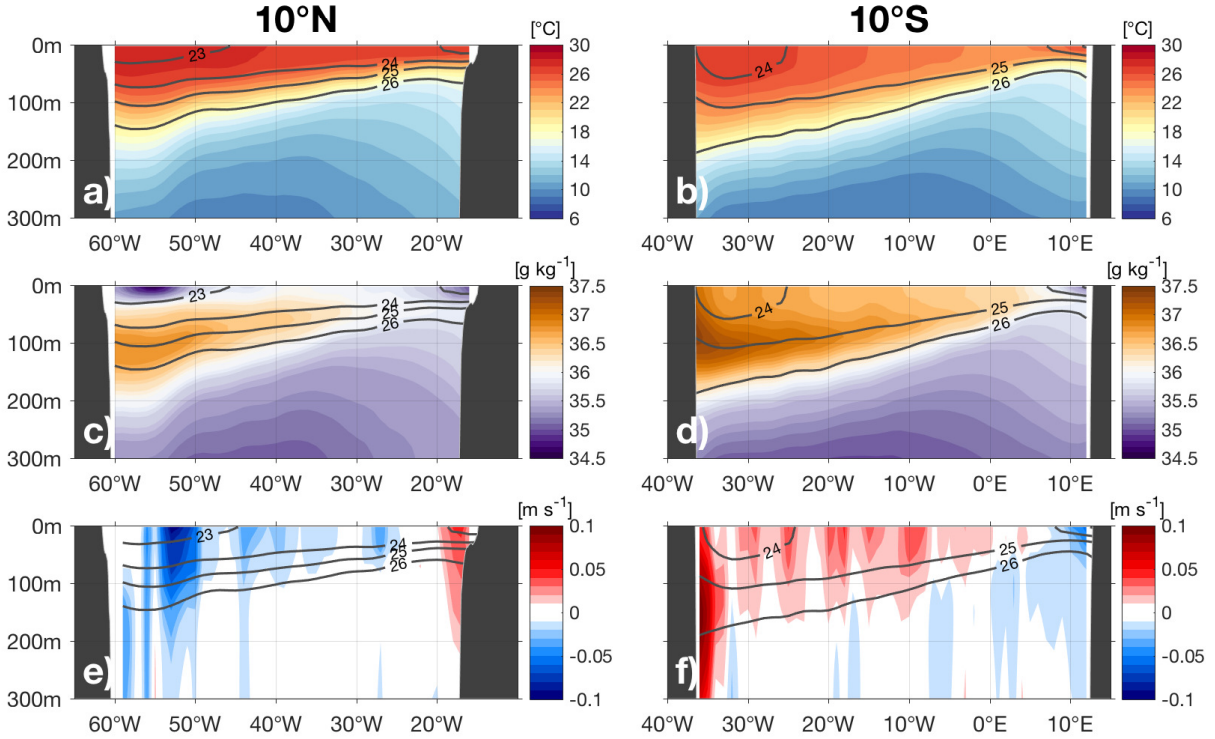


**Figure 3.2:** Zonal sections of (a)-(b) conservative temperature, (c)-(d) absolute salinity and (e)-(f) meridional geostrophic velocity along  $10^\circ \text{ N}$  (left column) and  $10^\circ \text{ S}$  (right column) from the RG-clim mean (see section 3.2.1 for detailed description). Isopycnal surfaces are shown as black contour lines. A realistic topography from the ETOPO1 data set shows the eastern and western boundaries of the sections.

In Fig. 3.3, we observe a change of sign in ORA-S4 data at lighter water masses and therefore closer to the surface, which could be indicative for the upper boundary of the lower STC branches. However, Fig. 3.2 shows that choosing an isopycnal for the lower boundary is justified as the sign of flow follows isopycnal surfaces while in the surface layers, isopycnal surfaces could intersect the Ekman layer in the east and the flow is not only a function of potential density anymore. The choice of the upper boundary is crucial as the geostrophic velocities and consequently the geostrophic transport increases toward the surface. Hence, in this study, we define the upper boundary of the lower STC branch by using the seasonally varying depth of meridional velocity reversal.

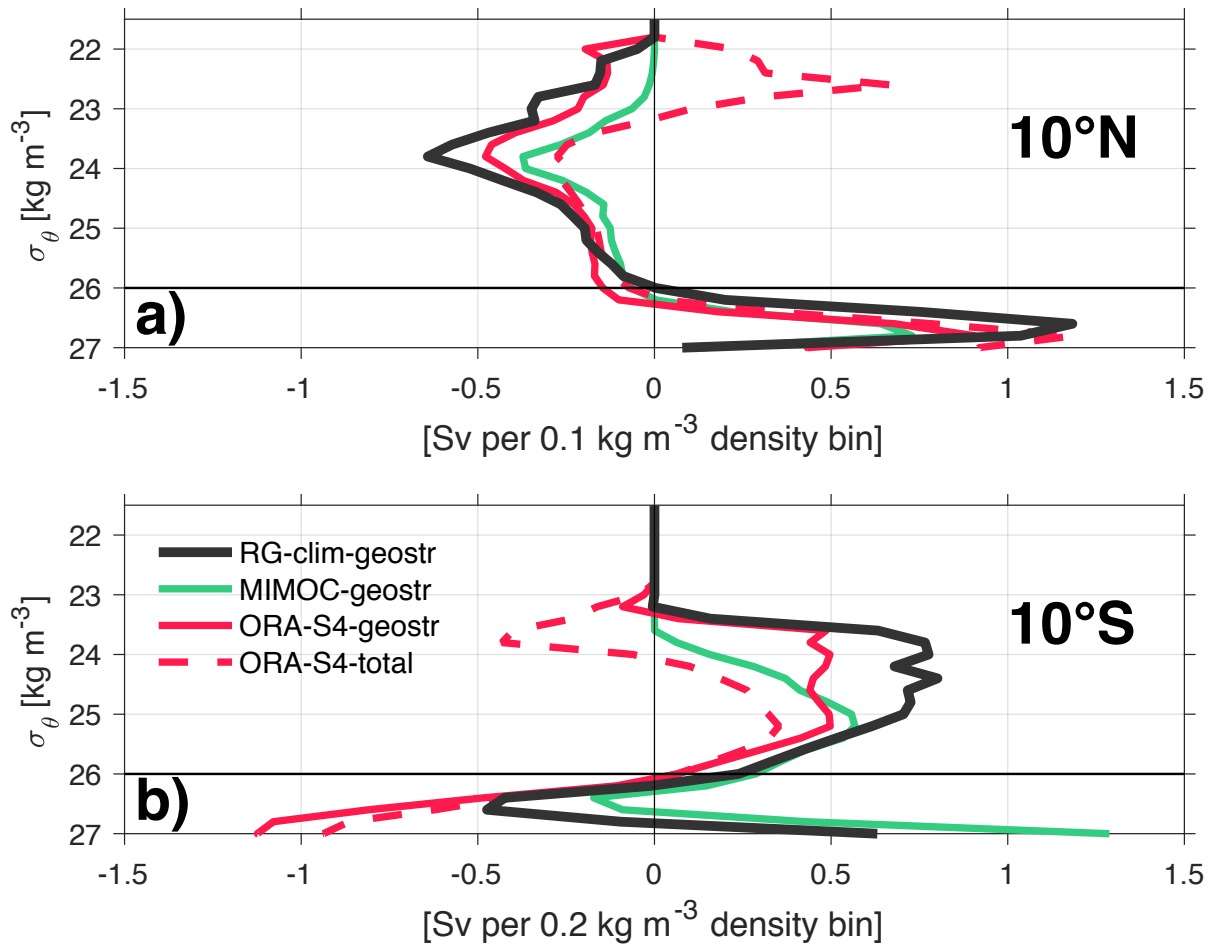


**Figure 3.3:** Averaged meridional transport per  $0.2 \text{ kg m}^{-3}$  density bin for (a)  $10^\circ \text{ N}$  and (b)  $10^\circ \text{ S}$  from the African coast to (a)  $55^\circ \text{ W}$  and (b)  $32^\circ \text{ W}$  thereby excluding the western boundary. Values show the transport within  $\pm 0.1 \text{ kg m}^{-3}$  of the isopycnal on the y-axis.

ORA-S4 provides absolute zonal and meridional velocity data of which the latter are used to determine the depth of meridional velocity reversal  $d_i$  (interface depth). The annual mean depth at which poleward velocities change to equatorward velocities at  $10^\circ \text{ N}$  and  $10^\circ \text{ S}$  is 60 m. However, the interface depth undergoes a strong seasonal cycle at both latitudes (Fig. 3.4). Consequently, the interface between the horizontal branches of the STCs is defined by a seasonally varying interface depth. The seasonal interface depths for  $10^\circ \text{ N}$  are 65, 65, 50 and 30 m respectively for winter, spring, summer, and autumn; the corresponding depths for  $10^\circ \text{ S}$  are 45, 50, 70 and 65 m (Fig. 3.4). In the zonal mean, the equatorward transports are accomplished in the density layer between the seasonally varying interface depth and the  $26.0 \text{ kg m}^{-3}$  isopycnal in both hemispheres.

The zonal mean is instructive to define the boundaries of the thermocline layer. With this definition, the horizontal distribution of the different meridional pathways of thermocline layer transport can be estimated (Fig. 3.5). Note that at the equator, geostrophic balance does not hold due to the vanishing Coriolis force.

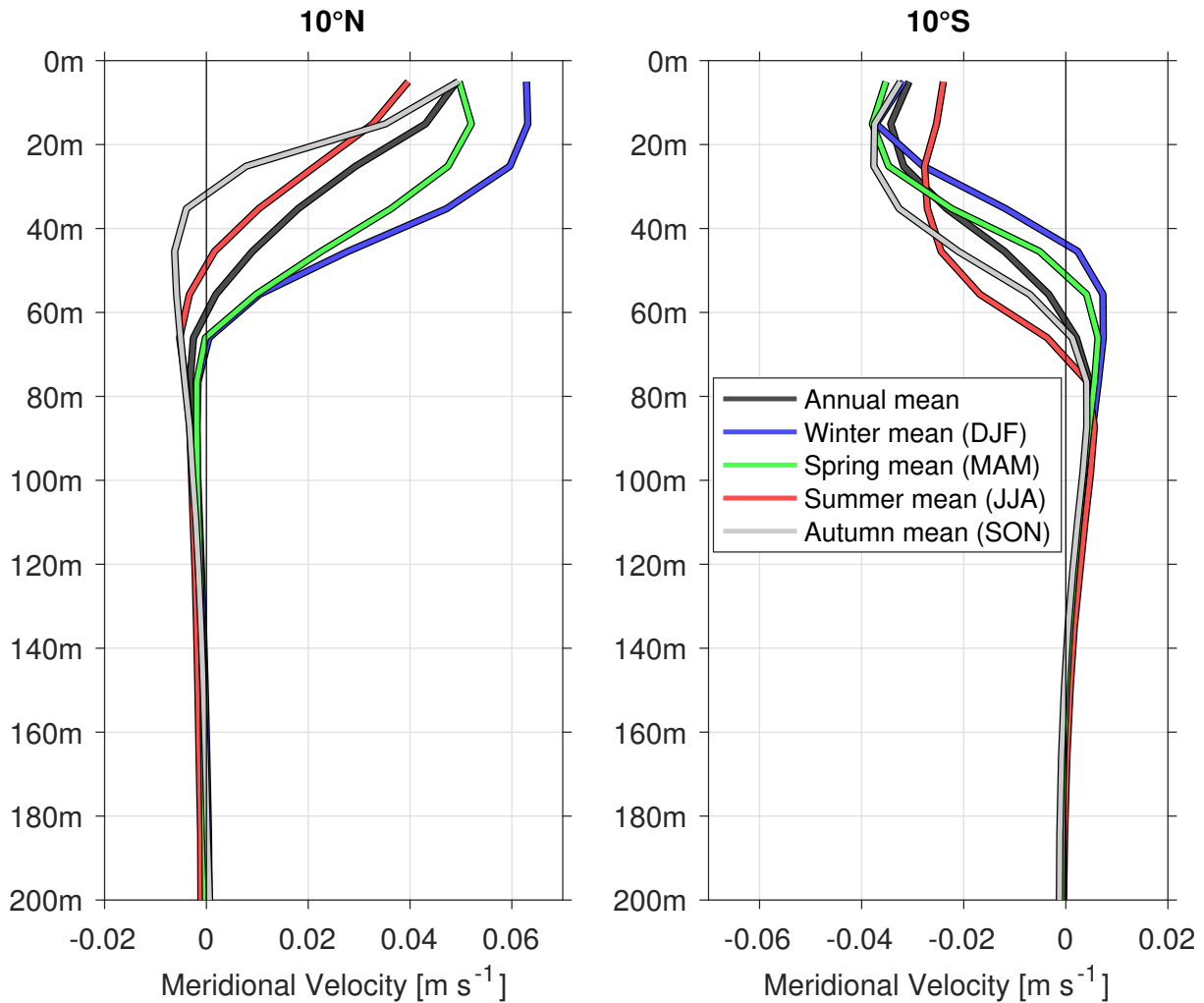


**Figure 3.4:** Zonally averaged vertical profiles of meridional velocity for boreal winter (blue), spring (green), summer (red) and autumn (gray) composites as well as for an annual mean (black) along the two sections at  $10^{\circ}$  N and  $10^{\circ}$  S from ORA-S4.

Hence, the calculations were only carried out poleward of  $\pm 2.5^{\circ}$ . In both hemispheres, the highest transport values occur at the western boundary with values of more than  $2Sv$  per  $1^{\circ}$  close to the equator. The intensified transports at the western boundary are a consistent feature starting at around  $15^{\circ}$  off the equator in both hemispheres and increasing toward lower latitudes. Transports associated with the southern STC are slightly higher compared to northern hemisphere values. Larger differences in thermocline layer transport are revealed in the interior part of the basin. At  $10^{\circ}$  S, substantial equatorward transport is observed in the interior basin. Although transport values do not reach the magnitude of the western boundary transports, the interior exchange window at  $10^{\circ}$  S exists between  $30^{\circ}$  W to  $10^{\circ}$  W. In contrast, at  $10^{\circ}$  N, interior transports east of the western boundary are almost absent in our analysis. However, closer to the equator, meridional transports are observed, though these are more likely to be associated with the TCs due to the missing connection to the subtropics. At  $10^{\circ}$  N, weak poleward transport is present east of about  $30^{\circ}$  W (Fig. 3.6). West of  $30^{\circ}$  W

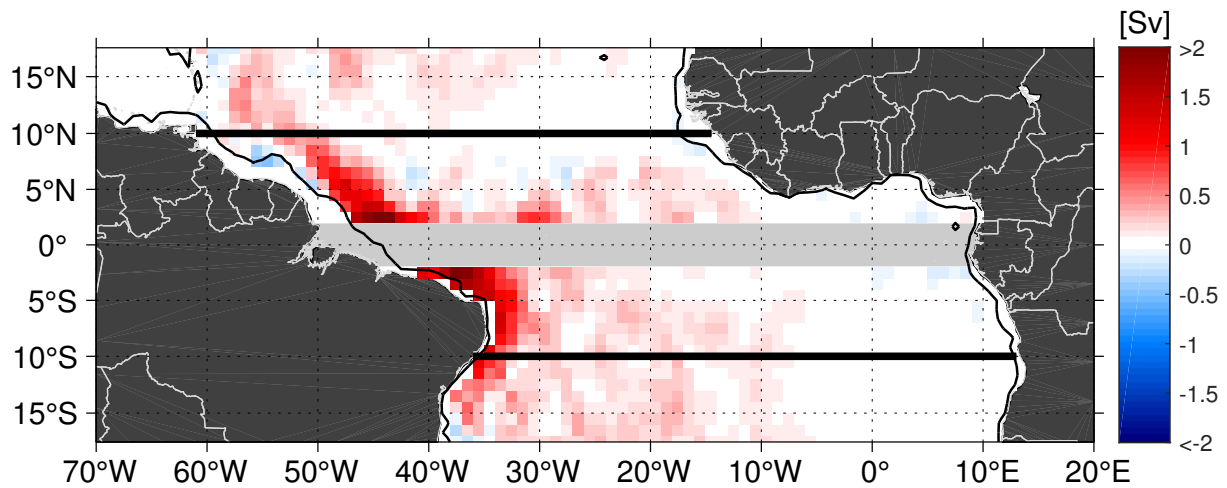


**Figure 3.5:** *Integrated equatorward geostrophic transport (from the RG-clim) between the seasonally varying interface depth and the  $26.0 \text{ kg m}^{-3}$  isopycnal for zonal boxes of  $1^\circ$  together with the 1000 m isobath from the ETOPO1 data set (black contour). The thick black lines indicate the zonal sections at  $10^\circ \text{ N}$  and  $10^\circ \text{ S}$ .*

weak equatorward transport in the interior basin steadily reduces the accumulated poleward transport leading to a net equatorward transport between  $0.2 - 1.2 \text{ Sv}$  at  $50^\circ \text{ W}$  (Tab. 3.1). Interior transport at  $10^\circ \text{ N}$  is not obvious in Fig. 3.5 consistent with close to zero accumulated transport east of about  $45^\circ \text{ W}$ . From  $50^\circ \text{ W}$  toward the western boundary, additional transport estimates vary between  $1.0 \text{ Sv}$  (ORA-S4-total) and  $2.7 \text{ Sv}$  (RG-clim) with MIMOC ( $1.4 \text{ Sv}$ ) and ORA-S4-geostr ( $2.3 \text{ Sv}$ ) in between this range. Transports from MIMOC-geostr are about  $1 \text{ Sv}$  smaller, presumably due to the northward flowing NBC at the western boundary which is better resolved due to included hydrographic data from CTD profiles close to the coast and boundary current mapping algorithm. In summary, all products agree for the majority of the  $10^\circ \text{ N}$  section apart from the most western part of the section where the spread in equatorward transport is highest.

Along  $10^\circ \text{ S}$ , all geostrophic estimates agree well from the African coast to  $32^\circ \text{ W}$  (the easternmost longitude of the western boundary ship section). Interior transports in the southern hemisphere add up to about  $3.8 \text{ Sv}$  (RG-clim). At the western boundary, the transport estimates from RG-clim and ORA-S4-geostr further agree on  $3.3 - 3.9 \text{ Sv}$  additional transport while MIMOC shows slightly less transport with  $2.0 \text{ Sv}$ . As an independent measure of the western boundary current transport, we use data from the repeated ship section at  $11.5^\circ \text{ S}$  (Fig. 3.7). Geostrophic velocity data from the  $11.5^\circ \text{ S}$  mean ship section at the western boundary produce a contribution of  $5.2 \text{ Sv}$  resulting in a total southern STC thermocline layer transport of  $9.0 \text{ Sv}$  (Fig. 3.6b) when added to the RG-clim value at  $32^\circ \text{ W}$ . In summary, we find a thermocline convergence between  $8.8$  and  $10.9 \text{ Sv}$  of which about  $2.2 - 3.0 \text{ Sv}$  come from the northern and  $6.5 - 8.7 \text{ Sv}$  are provided by the southern STC. The difference between interior and western boundary transport is most prominent in the northern hemisphere in the RG-clim estimates with essentially no interior transport.

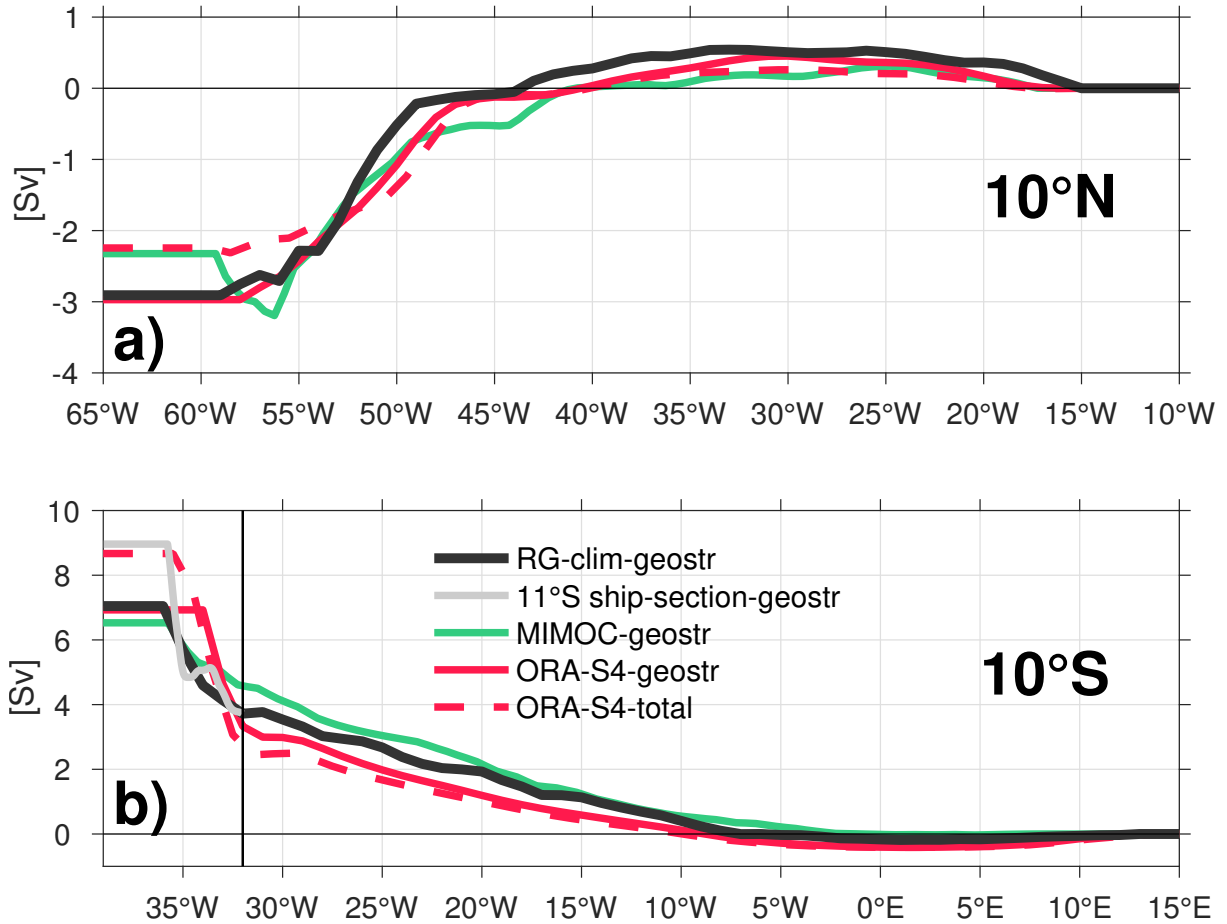


**Figure 3.6:** Cumulative meridional transport along (a)  $10^\circ$  N and (b)  $10^\circ$  S integrated from east to west and between the seasonally varying interface depth and the  $26.0 \text{ kg m}^{-3}$  isopycnal. The black line at  $32^\circ$  W in (b) indicates the most eastern extent of the repeated ship section at  $11.5^\circ$  S at which the western boundary transport from the ship section is added to the accumulated transport of RG-clim at  $32^\circ$  W.

### 3.4.2 Surface Transports

We have shown that the lower branches of the STCs encompass water masses toward the equator in a layer between the seasonally varying interface depth and the  $26.0 \text{ kg m}^{-3}$  isopycnal with a contribution from the southern hemisphere three times higher than that from the northern hemisphere and a higher contribution from the western boundaries than from the interior ocean basins. Equatorward transport leads to convergence in the equatorial regions at thermocline level. There, thermocline water is entrained into the EUC and upwells either along its eastward pathway or reaches the eastern boundary upwelling systems. The STCs are eventually closed by poleward transport in the surface layer driven by meridional Ekman transport. In order to estimate the poleward transport of the upper branches of the STCs,

10° N					
	RG-clim	MIMOC	ORA-geostr	ORA-total	ship section
INT $\pm\epsilon$	0.2 $\pm$ 0.5	0.9 $\pm$ 0.3	0.7 $\pm$ 0.7	1.2 $\pm$ 0.7	-
WB $\pm\epsilon$	2.7 $\pm$ 1.2	1.4 $\pm$ 0.5	2.3 $\pm$ 0.7	1.0 $\pm$ 0.8	-
TOTAL $\pm\epsilon$	2.9 $\pm$ 1.3	2.3 $\pm$ 0.5	3.0 $\pm$ 1.0	2.2 $\pm$ 1.1	-
10° S					
	RG-clim	MIMOC	ORA-geostr	ORA-total	ship section
INT $\pm\epsilon$	3.8 $\pm$ 0.8	4.6 $\pm$ 0.2	3.0 $\pm$ 0.6	2.5 $\pm$ 0.5	-
WB $\pm\epsilon$	3.3 $\pm$ 0.6	2.0 $\pm$ 0.2	3.9 $\pm$ 0.5	6.2 $\pm$ 0.7	5.2 $\pm$ 0.8
TOTAL $\pm\epsilon$	7.1 $\pm$ 1.0	6.5 $\pm$ 0.3	6.9 $\pm$ 0.7	8.7 $\pm$ 0.9	9.0 $\pm$ 1.1

**Table 3.1:** *Equatorward transport between the seasonally varying interface depth and the 26.0 kg m<sup>-3</sup> isopycnal for different products at the two zonal sections at 10° N/S. At 10° N (10° S) the 50° W (32° W) longitude divides the sections into an interior part (INT) and a western boundary part (WB). Shown is also the zonally accumulated transport (TOTAL) over the whole basin as well as the particular error estimates (see section 3.3.1 for details).*

several wind products are used (described in section 3.2.5). Both hemispheres are divided into an eastern part, where the mean zonal wind stress leads to weak or no equatorward Ekman transports and a western part with poleward Ekman transports generally intensifying toward the western boundary (Fig. 3.8). Meridional Ekman transport maps derived from the other wind products (not shown) agree well on this structure. The accumulated meridional Ekman transport values along the zonal sections at 10° N and 10° S are shown in Tab. 3.2. Here, negative transport values indicate southward transport while positive values indicate northward transport. For individual wind products, the Ekman divergence among 10° N and 10° S appears rather symmetric although differences in the strength of the Ekman divergence between the products are found. The symmetry of transport in the surface layer is in contrast to the asymmetric interhemispheric transport distribution at thermocline level. Hence, between 10° N and 10° S, an Ekman divergence of about 20.4 Sv (mean value derived from three wind products) is found and faces a thermocline convergence of about 11.9 Sv (RG-clim including western boundary ship section mean at 10° S).

However, as we have seen in Fig. 3.2, geostrophic flow is also present in the surface layer and generally counteracts the poleward Ekman transport. Hence, the upper branches of the STCs consist of two opposing meridional transports: poleward Ekman transport and equatorward geostrophic transport. Tab. 3.2 also shows the surface layer geostrophic transport from RG-clim, MIMOC, and ORA-S4. We find good agreement among the products as well as a further signature of the interhemispheric asymmetry in equatorward geostrophic transport with about twice as much transport originating in the southern hemisphere (3.6–5.1 Sv vs. 1.9–2.5 Sv). In contrast to the thermocline layer, geostrophic transport in the surface layer is higher in the interior basin, which is especially the case for the southern hemisphere. In the surface layer, geostrophic transports are opposite to Ekman transports derived from wind products (Tab.



3.2). Therefore, the sum of Ekman transport and geostrophic transport can be seen as a net transport.

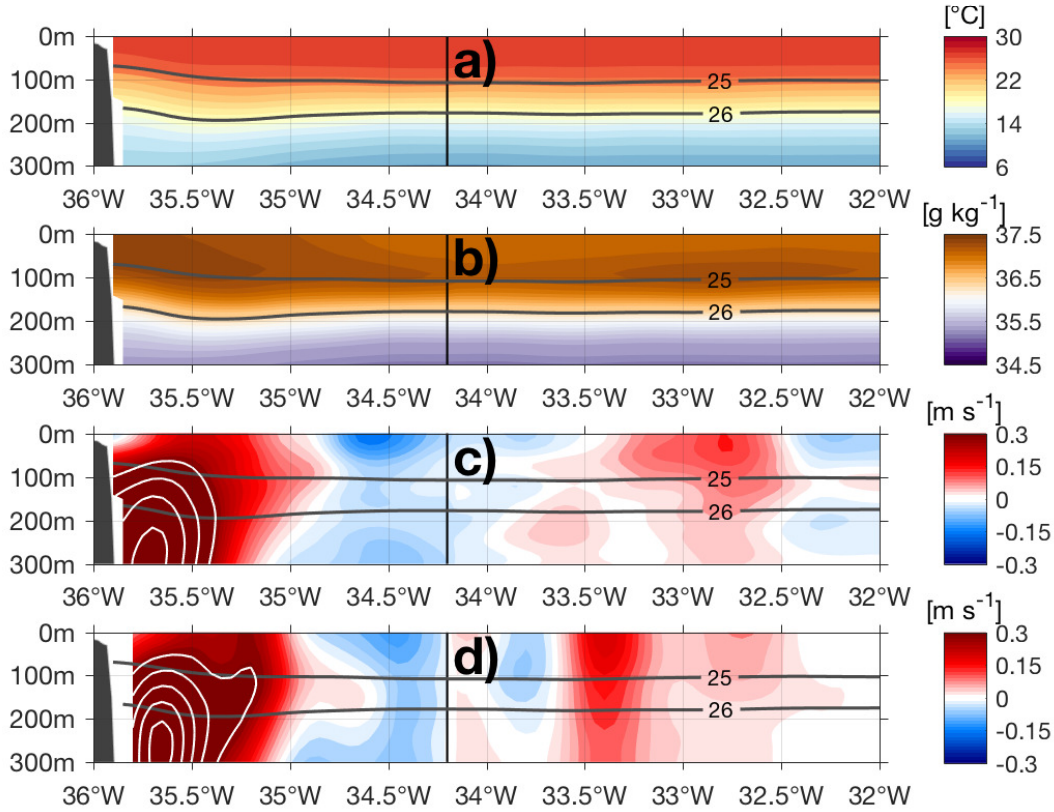


**Figure 3.7:** Mean (a) conservative temperature, (b) absolute salinity, (c) meridional/alongshore absolute velocity and (d) meridional/alongshore geostrophic velocity from the repeated ship section at  $11.5^{\circ}$  S. Isopycnal surfaces are shown as black contour lines. The black line at  $34.2^{\circ}$  W marks the longitude at which the ship section turns northwestward (see, e.g., Fig. 3.1). The western boundary of the section is depicted by the topography from the ETOPO1 data set.

However, the net transport can also be directly estimated from absolute velocities from ORAS4 (Tab. 3.2). Interestingly, interior and western boundary net transport at  $10^{\circ}$  N are close to being equal while the southern hemisphere net transport is clearly dominated by interior transport. The same way the subsurface NBUC in the southern hemisphere distributes water to the equator at thermocline level, the surface intensified NBC/Guyana Current in the northern hemisphere withdraws water poleward in the surface layer but to a lesser extent. The difference in net transports between both methods is relatively small (Tab. 3.2) and generally confirms the choice of layer boundaries in this study. It also indicates that the choice of the interface between the upper and the lower branch of the STCs (described in section 3.4.1) is plausible. In summary, we observe a surface layer divergence of meridional transport of  $14.6 \pm 3.4 S_V$  when

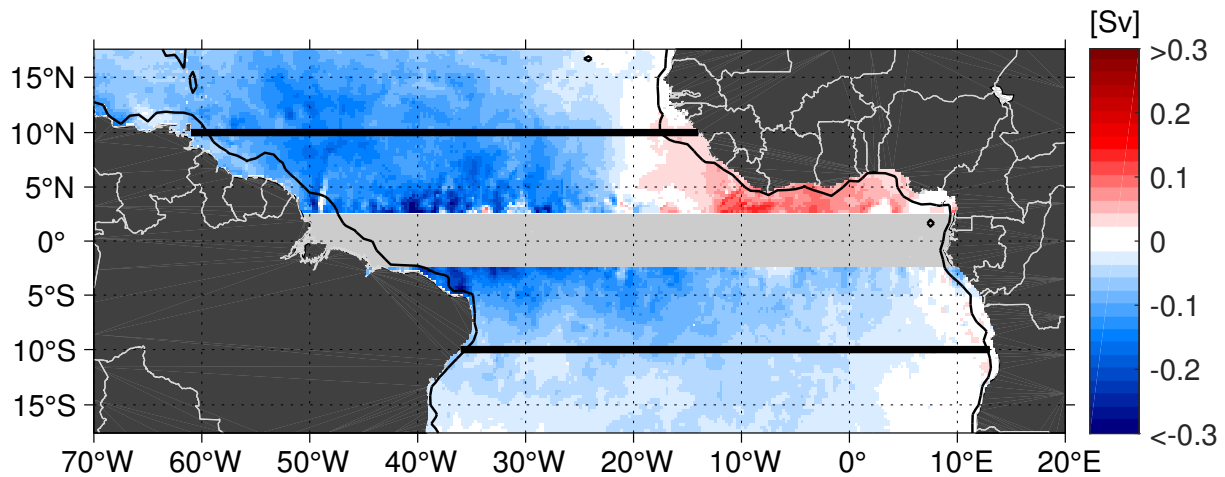


**Figure 3.8:** Mean meridional Ekman transport derived from daily ASCAT wind stress data between 2007 to 2018. The thick black lines indicate the zonal sections at  $10^{\circ}$  N and  $10^{\circ}$  S at which the meridional Ekman transport is accumulated from east to west and the black contour lines show the 1000 m isobath from the ETOPO1 data set. Note that red colours indicate equatorward transport and blue colours poleward transport.

considering the sum of an averaged Ekman divergence ( $20.4 \pm 3.1$  Sv) and the geostrophic surface convergence from RG-clim ( $5.8 \pm 1.4$  Sv). Overall, in combination with the thermocline layer convergence of  $11.9 \pm 1.7$  Sv, a residual of  $2.7 \pm 3.8$  Sv is required to maintain the balance of the STC circulation regime. Sources for the missing transport will be discussed in the next section.

### 3.5 Summary and Discussion

This study provides observational estimates for both branches of the Atlantic STCs and compares them to results from a reanalysis product and previous studies. Based on the rapidly increasing data coverage of the world's oceans by Argo floats within the last two decades, [Roemmich and Gilson \(2009\)](#) constructed a hydrographic climatology of which an updated version considering Argo profiles between January 2004 and December 2016 is available. Besides Argo float data, we have made use of another hydrographic climatology, MIMOC ([Schmidtke et al., 2013](#)), that additionally includes shipboard CTD data. In this study, the issue of sparse data coverage at the western boundary by Argo floats is further addressed by analyzing data from a repeated ship section at  $11.5^{\circ}$  S ([Hummels et al., 2015](#)) to derive reliable estimates of the western boundary transport in the STC density range. The analysis is complemented by hydrographic and velocity data from the ORA-S4 reanalysis ([Balmaseda et al., 2013](#)). Previous to the Argo era, the study of [Zhang et al. \(2003\)](#), who estimated STC transports based on hydrographic data, provided a benchmark against which numerical studies compared their results. Our study provides an update of the temporal mean transport estimates of

10° N											
Geostrophic			Ekman			Net					
	RG-clim	MIMOC	ORA-S4	ASCAT	NCEP/NCAR	JRA-55	ORA-S4	ASCAT + RG-clim			
INT ±ε	-0.7± 0.8	-1.5± 0.4	-1.0± 0.9	6.1± 0.6	5.8± 1.9	5.4± 0.7	3.4± 1.2	5.4			
WB ±ε	-1.4± 0.9	-1.0± 0.4	-0.9± 0.6	3.5± 0.3	4.4± 1.2	3.3± 0.4	3.0± 0.9	2.1			
TOTAL ±ε	-2.1± 1.2	-2.5± 0.6	-1.9± 1.0	9.6± 0.7	10.2± 2.2	8.7± 0.8	6.4± 1.4	7.5			
10° S											
Geostrophic			Ekman			Net					
	RG-clim	MIMOC	ORA-S4	ASCAT	NCEP/NCAR	JRA-55	ORA-S4	ASCAT + RG-clim			
INT ±ε	2.6± 0.6	4.8± 0.2	2.7± 0.7	-10.1± 0.5	-10.6± 1.6	-8.5± 0.5	-6.2± 0.7	-7.6			
WB ±ε	1.2± 0.3	0.3± 0.1	0.9± 0.4	-1.1± 0.1	-1.4± 0.6	-1.0± 0.2	0.7± 0.5	0.1			
TOTAL ±ε	3.7± 0.7	5.1± 0.3	3.6± 0.8	-11.2± 0.5	-12.0± 1.7	-9.5± 0.5	-5.5± 0.8	-7.5			

**Table 3.2:** Geostrophic, Ekman and net transport between the surface and the seasonally varying interface depth from different products at the two zonal sections at 10° N/S. At 10° N (10° S) the 50° W (32° W) longitude divides the sections into an interior part (INT) and a western boundary part (WB). Shown is also the zonally accumulated transport over the whole basin (TOTAL) as well as the particular error estimates (see section 3.3.1 for details).

the STCs thereby presenting a 21st century mean state of the Atlantic STCs based on hydrographic and velocity observations. Besides the data sets used here, the most significant changes from this study to the estimates by [Zhang et al. \(2003\)](#) are the definition of the vertical boundaries of the branches of the STCs and the choice of latitude for the southern section. In agreement with [Schott et al. \(2004\)](#) and [Rabe et al. \(2008\)](#), we focused our analysis on zonal sections at  $10^\circ$  N and  $10^\circ$  S while [Zhang et al. \(2003\)](#) chose a southern section along  $6^\circ$  S. Both,  $10^\circ$  N and  $10^\circ$  S, are sufficiently far away from the TCs and the subtropical subduction zones suggesting that transports associated with the STCs must pass these sections. The southern section at  $10^\circ$  S is mainly chosen due to the availability of a repeated ship section along  $11.5^\circ$  S close-by. With the help of spatially high-resolved observational data at the crucial western boundary region, we could show that Argo based observational products as RG-clim likely underestimate the transport at the western boundary at  $10^\circ$  S (e.g., Fig. 3.6 and Tab. 3.1). From hydrographic properties along the chosen sections, meridional geostrophic velocity — referenced to the 1000 dbar meridional displacement derived from YoMaHa'07 ([Lebedev et al., 2007](#)) — and isopycnal surfaces are calculated (Fig. 3.2). In general, equatorward geostrophic velocities are observed from the surface down to approximately  $26.0 \text{ kg m}^{-3}$ . However, in the surface layer, the wind-driven poleward Ekman transport is counteracting the geostrophic flow. Therefore, we suggest to identify the interface depth between the poleward and the equatorward STC branches as the depth at which the meridional velocity reverses and below which the flow is in geostrophic balance. As shown in Fig. 3.4, a seasonally varying interface depth (between 30 – 65 m at  $10^\circ$  N and 45 – 70 m at  $10^\circ$  S) is used for the transport estimation. This definition further takes into account that the isopycnals are sloping upward toward the east (Fig. 3.2). A purely isopycnal definition of the interface leads to an upper boundary that crosses the Ekman layer in the eastern part of the basin and underestimates the thickness of the thermocline layer in the western part. Consequently, it is suggested that the STCs transport water masses toward the equator in a layer between the interface depth and an isopycnal surface. This layer is called thermocline layer or pycnocline layer (e.g. [Zhang et al., 2003](#)). The lower boundary of this layer is defined using the zonal mean of meridional transport per  $0.2 \text{ kg m}^{-3}$  density bin (Fig. 3.4). In both hemispheres, the lower boundary of the thermocline layer is set to  $26.0 \text{ kg m}^{-3}$ . In previous studies, this thermocline layer has been enclosed by isopycnal layers at the top and bottom. For instance, [Zhang et al. \(2003\)](#) defined their northern hemisphere thermocline layer between  $23.2$  and  $26.0 \text{ kg m}^{-3}$  and their southern hemisphere thermocline layer between  $23.6$  and  $26.2 \text{ kg m}^{-3}$ , whereas [Fratantoni et al. \(2000\)](#) used two of their six model layers to describe thermocline transports between  $25.2$  and  $26.8 \text{ kg m}^{-3}$  and [Hazeleger and Drijfhout \(2006\)](#) used the mixed-layer-depth as the interface between the two STC branches. The vertical resolution in numerical studies is often too coarse to define more precise boundaries.

Following our definition of the thermocline layer boundaries, meridional transports within this layer have been calculated. Unless otherwise noted, the mentioned thermocline layer transports

refer to the estimates from the RG-clim. In general, equatorward transports can be divided into transports along the western boundary and within the interior ocean. The boundary is set to  $50^\circ$  W for the northern section and to  $32^\circ$  W for the southern section. We are able to show that for the northern hemisphere STC, the interior exchange window is extremely small (Fig. 3.5) and only exhibits a marginal equatorward transport, not significantly different from zero (Tab. 3.1). This is most likely due to the presence of the previously described PV barrier in the northeastern tropical Atlantic (e.g. Harper, 2000; Hazeleger and Drijfhout, 2006) forcing a detour of the equatorward flow. Hence, at  $10^\circ$  N, most of the equatorward transport is accomplished via the western boundary within the recirculation pathway of the NBC (about  $2.7\text{ Sv}$ ). Closer to the coast, the northward flow of the NBC at the western boundary within the thermocline layer is suggested to reduce the equatorward transport as indicated by MI-MOC (see Fig. 3.6a). Johns *et al.* (1998) found that the NBC at  $3^\circ - 4^\circ$  N transports about  $3 - 5\text{ Sv}$  over the continental shelf of which parts recirculate into the zonal current system in the tropical Atlantic and would not be observed at  $10^\circ$  N. As part of the North Brazil Current Rings Experiment, Garzoli *et al.* (2003) estimated the annual mean transport due to the rings to be  $8\text{ Sv}$  based on 11 rings between November 1998 and June 2000. Clearly, the data coverage at the western boundary in the northern hemisphere introduces an uncertainty to the budget-like transport estimates of the STC branches in this analysis. The thermocline convergence contribution of the northern hemisphere STC is estimated to be approximately  $2.9\text{ Sv}$  ( $2.7\text{ Sv}$  western boundary and  $0.2\text{ Sv}$  interior). Due to the superposition of the AMOC on equatorward transport at the western boundary and the absence of a PV barrier in the eastern part of the basin, the southern hemisphere STC is significantly stronger than its northern counterpart (e.g. Fratantoni *et al.*, 2000). We show that at  $10^\circ$  S, an interior transport of about  $3.8\text{ Sv}$  is observed in a window from about  $10^\circ$  W to  $32^\circ$  W (Fig. 3.6b). At the western boundary, the horizontal resolution and the representation of the western boundary current among the products introduce an uncertainty and a range of equatorward transport between  $2.0$  and  $6.2\text{ Sv}$  is estimated (Fig. 3.6b and Tab. 3.1). When transport from the mean ship section is added to the  $32^\circ$  W value of the RG-clim, an equatorward thermocline transport of  $9.0\text{ Sv}$  along  $10^\circ$  S results (Fig. 3.9). Note that the mean section consists of five individual sections of shipboard velocity measurements. Although those sections are distributed relatively even throughout the seasons, an uncertainty remains about the representation of the mean state. However, moored observations reassuringly show a similar mean (Hummels *et al.*, 2015). In summary, we find a thermocline layer convergence of  $11.9\text{ Sv}$  equatorward transport (considering RG-clim estimates in the northern hemisphere and combined RG-clim and ship section estimates in the southern hemisphere) between  $10^\circ$  N and  $10^\circ$  S which is about  $3\text{ Sv}$  less than previously estimated by Zhang *et al.* (2003). This difference can at least partly be explained by the different choices of vertical thermocline layer boundaries as described above. Especially in the eastern part of the basin, choosing the depth of meridional velocity reversal as the upper boundary leads to a smaller layer thickness compared to an isopycnal boundary as used by

Zhang *et al.* (2003).

In the surface layer, wind products are averaged to a mean Ekman divergence of 20.4 Sv (Tab. 3.2) which is slightly smaller than in previous studies such as Schott *et al.* (2004) who report 21 and 23 Sv of zonally integrated annual-mean Ekman divergence for NCEP reanalysis and ERS.1,2 scatterometer data respectively for an earlier time period. The wind-driven Ekman transport is reduced by the geostrophic transport (integrated from the surface to the interface depth) and results in the net meridional transport in the surface layer.

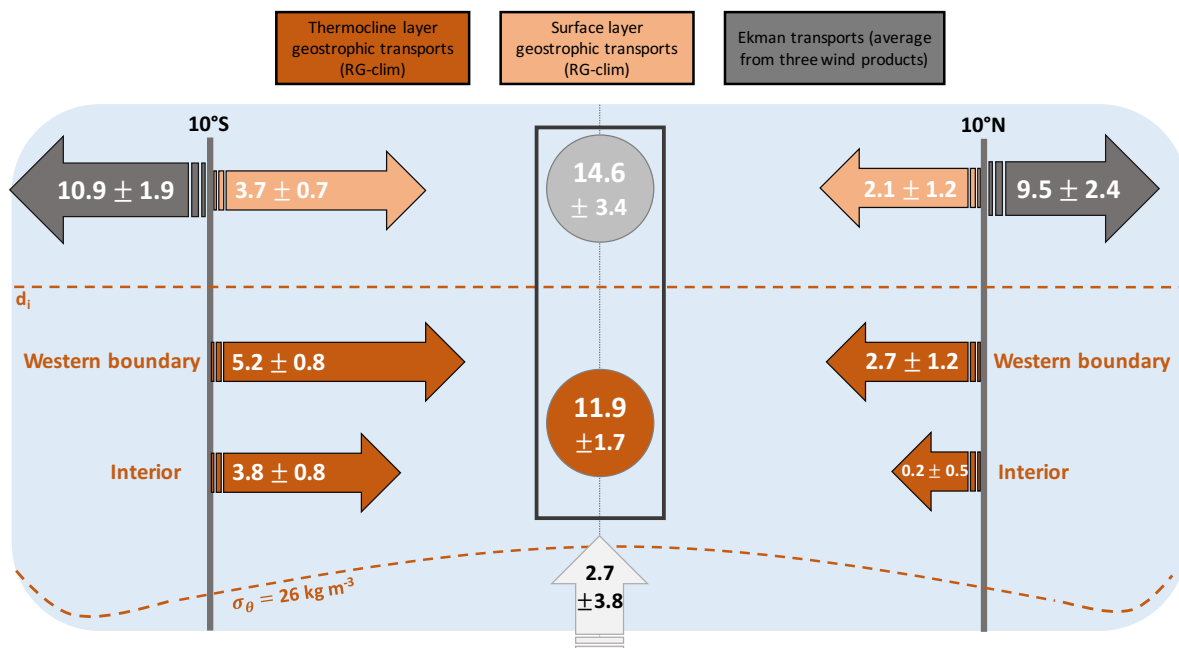


**Figure 3.9:** Schematic of particular meridional transport contributions to the Atlantic STCs in Sv. Shown are geostrophic transports as estimated by RG-clim (dark orange in the thermocline layer and light orange in the surface layer) in combination with mean ship sections for the western boundary in the southern hemisphere as well as the mean meridional Ekman transport derived from three different wind products (gray). The equatorward transport associated with the lower branch of the STCs occurs between the seasonally varying interface depth  $d_i$  and the  $26.0 \text{ kg m}^{-3}$  isopycnal. At the equator, Ekman divergence within the surface layer forces upwelling and poleward Ekman transport associated with the upper branch of the STCs. An estimated 2.7 Sv (light gray arrow) has to enter the thermocline layer in the tropics to balance the transport estimates. Note that due to the uncertainty at the western boundary at  $10^\circ \text{ N}$  this value is likely to be higher.

The sum of the STC related equatorward and poleward transport contributions yields a residual of 2.7 Sv which is suggested to be upwelled from below the thermocline as part of the interhemispheric AMOC return flow (Fig. 3.9). This number is smaller than in previous studies in which estimates of the return flow of the thermohaline circulation ranged between 6 and 10 Sv from below the thermocline layer across the  $26.2 \text{ kg m}^{-3}$  isopycnal (Roemmich, 1983).

*Hazeleger and Drijfhout (2006)* and *Lux et al. (2001)* arrived at similar values of 5.5 and 7.5 Sv, respectively. The most likely explanation for this discrepancy is the underestimation of the northward western boundary current north of the equator in our study. Especially estimates at the western boundary in the northern hemisphere are still uncertain and more ship sections and Argo float data are needed to derive more reliable transport values and to decrease the uncertainty.

This study provides an update for observational estimates of Atlantic STC transports and aims to represent the 21st century mean STCs from an observational perspective. Observations from the Argo program are suitable to represent the geostrophic branches of the Atlantic STCs. This improvement in data coverage is especially important when considering interannual to decadal variability of STC transports which so far could not be captured by observations. Building on the definitions for the STC branches and their boundaries developed here, future work will focus on the impact of seasonal to interannual variability of both transport and water mass properties on SST variability to gain more insight on the responsible mechanism (*Gu and Philander, 1997; Kleeman et al., 1999*).

## Acknowledgments

This study was supported by the Deutsche Forschungsgemeinschaft as part of the Sonderforschungsbereich 754 (SFB754) "Climate– Biogeochemistry Interactions in the Tropical Ocean" and through several research cruises with R/V Meteor by the German Federal Ministry of Education and Research as part of the cooperative projects RACE (03F0605B and 03F0824C) and SACUS II (03F0751A). We thank the captains and crew of the R/V Meteor as well as our technical group for their help with the field-work. Shipboard CTD measurements used in this study are available through PANGAEA at:

- <https://doi.org/10.1594/PANGAEA.868640> (M98)
- <https://doi.org/10.1594/PANGAEA.869361> (M106)
- <https://doi.org/10.1594/PANGAEA.860484> (M119)
- <https://doi.org/10.1594/PANGAEA.904367> (M130)
- <https://doi.org/10.1594/PANGAEA.904382> (M145)

The hydrographic climatology from Roemmich & Gilson is accessible via [http://sio-argo.ucsd.edu/RG\\_Climatology.html](http://sio-argo.ucsd.edu/RG_Climatology.html) (we used the latest update from December 19th 2017). Pressure gridded potential temperature and practical salinity from MIMOC is available at <https://www.pmel.noaa.gov/mimoc/>. Reanalysis data from ORA-S4 can be accessed via [ftp://ftp-icdc.cen.uni-hamburg.de/EASYInit/ORA-S4/monthly\\_1x1/](ftp://ftp-icdc.cen.uni-hamburg.de/EASYInit/ORA-S4/monthly_1x1/).

JRA-55 reanalysis data were provided by the NCAR/UCAR Research Data Archive (accessible via <http://rda.ucar.edu/> under data set number ds628.0). ASCAT data are produced by Remote Sensing Systems and sponsored by the NASA Ocean Vector Winds Science Team (data are available at <http://www.remss.com> or at <https://coastwatch.pfeg.noaa.gov/erddap/griddap/erdQMstress1day.html>). NCEP-NCAR Reanalysis 1 data is provided by the NOAA/OAR/ESRL PSD, Boulder, Colorado, USA, from their website at <https://www.esrl.noaa.gov/psd/>.



# 4 Observed transport variability of the Atlantic Subtropical Cells and their connection to tropical sea surface temperature variability

The following chapter is based on the definition of the mean Atlantic STCs in chapter 3 and further explores associated transport variability of the horizontal STC branches. First, the dominant time scales of transport variability are identified. Second, the relation between western boundary and interior transport anomalies is investigated. This chapter is completed by a detailed analysis of the connection between observed STC transport variability and SST anomalies in the tropical Atlantic Ocean with a focus on most affected regions, relevant time scales and time lags. Thereby, the mechanism behind the observed connection STC and SST anomalies is discussed.

The manuscript is currently under review in *Journal of Geophysical Research: Oceans*.

---

**Tuchen, F. P.**, Lübbecke, J. F., Brandt, P. and Fu, Y. (under review): Observed transport variability of the Atlantic Subtropical Cells and their connection to tropical sea surface temperature variability, *Journal of Geophysical Research: Oceans*.

---

The candidate designed the study and carried out the analysis of observational, reanalysis and satellite data products, produced all figures and authored the manuscript from the first draft to the submitted version.

## Abstract

The shallow meridional overturning cells of the Atlantic Ocean, the Subtropical Cells (STCs), consist of poleward Ekman transport at the surface, subduction in the subtropics, equatorward flow at thermocline level and upwelling along the equator and at the eastern boundary. In this study we provide the first observational estimate of transport variability associated with the horizontal branches of the Atlantic STCs in both hemispheres based on Argo float data and supplemented by reanalysis products. Thermocline layer transport convergence and surface layer transport divergence between  $10^{\circ}$  N and  $10^{\circ}$  S are dominated by seasonal variability. Meridional thermocline layer transport anomalies at the western boundary and in the interior basin are anti-correlated and partially compensate each other at all resolved time scales. It is suggested that the seesaw-like relation is forced by the large-scale off-equatorial wind stress changes through low baroclinic mode Rossby wave adjustment. We further show that anomalies of the thermocline layer interior transport convergence modulate sea surface temperature (SST) variability in the upwelling regions along the equator and at the eastern boundary at time scales longer than  $\sim 5$  years. Phases of weaker (stronger) interior transport are associated with phases of higher (lower) equatorial SST. At these time scales, STC transport variability is forced by off-equatorial wind stress changes, especially by those in the southern hemisphere. At shorter time scales, equatorial SST anomalies are, instead, mainly forced by local changes of zonal wind stress.

## Plain Language Summary

In both hemispheres of the Atlantic Ocean, meridional overturning circulations provide a connection between the subtropics and equatorial upwelling regions. The so-called Subtropical Cells (STCs) consist of poleward transport at the surface driven by the easterly trade winds, subduction in the subtropics, equatorward flow at subsurface level and upwelling along the equator and at the eastern boundary. In this study, we provide the first observational time series of transport variability associated with the horizontal branches of the STCs estimated at  $10^{\circ}$  N and  $10^{\circ}$  S. It shows that both branches are dominated by variability on seasonal time scales. On longer time scales, transport anomalies at the western boundary reveal a reversed relation to transport anomalies in the interior leading to partial compensation. It is suggested that transport anomalies are affected by adjustment to wind-forced oceanic planetary waves. We further show that the interior part of the subsurface transport anomalies is connected to equatorial sea surface temperature (SST) anomalies at time scales longer than  $\sim 5$  years. There, stronger (weaker) equatorward transport is associated with negative (positive) equatorial SST anomalies. At shorter time scales, equatorial SST anomalies are, instead, mainly forced by changes of local wind stress.

## 4.1 Introduction

The shallow tropical Atlantic Ocean is characterized by a superposition of the wind-driven and density-driven circulation (e.g. [Schott et al., 2004](#)). Most prominently, the warm water return flow of the Atlantic Meridional Overturning Circulation (AMOC) crosses the equator on its northward pathway along the Brazilian coast, first, as part of the North Brazil Undercurrent (NBUC) and, closer to the equator, as part of the North Brazil Undercurrent (NBUC)/North Brazil Current (NBC) ([Stramma et al., 1995](#)). Superimposed on the uppermost part of the AMOC return flow are shallow meridional overturning circulations, referred to as the subtropical cells (STCs), that connect the subduction zones of the subtropical gyres with the equatorial and eastern tropical upwelling regions ([Luyten et al., 1983](#); [McCreary and Lu, 1994](#); [Liu et al., 1994](#)). The STCs are confined to approximately the upper 300 m and are forced by equatorial Ekman divergence due to the easterly trade winds. In a zonal average of each hemisphere, they consist of poleward Ekman transport in the surface layer, subduction in the subtropics, equatorward geostrophic transport at thermocline level and are eventually closed by upwelling along the equator and at the eastern boundary (e.g. [Fratantoni et al., 2000](#); [Malanotte-Rizzoli et al., 2000](#); [Schott et al., 2004](#)). As a consequence of the superposition of STCs and AMOC at the western boundary, an interhemispheric asymmetry in terms of mean equatorward STC transport at thermocline level exists in which the southern hemisphere STC carries about 2 to 3 times more water towards the equator than its counterpart in the northern hemisphere ([Fratantoni et al., 2000](#); [Zhang et al., 2003](#); [Tuchen et al., 2019](#)). Besides this interhemispheric asymmetry, the mean state of the Atlantic STCs further exhibits a zonal asymmetry between equatorward transport at the western boundary and in the interior basin in both hemispheres ([Zhang et al., 2003](#); [Tuchen et al., 2019](#)). Generally, the western boundary pathways contribute more to the overall thermocline layer transport convergence due to both a limitation of interior transport in the northern hemisphere caused by a potential vorticity ridge ([Malanotte-Rizzoli et al., 2000](#)) and a strong western boundary current in the southern hemisphere supported by the AMOC return flow ([Schott et al., 2002a](#)). However, a general lack of Argo observations at the shelf and continental slope and diverging results from model simulations of western boundary current transport introduce a considerable uncertainty when compared to one of the few observational long-term records, e.g. along 11° S ([Hummels et al., 2015](#); [Tuchen et al., 2019](#)). While there have been several studies describing the mean state of the Atlantic STCs both from a model (e.g. [Hazeleger et al., 2003](#); [Hazeleger and Drijfhout, 2006](#)) and from an observational perspective ([Zhang et al., 2003](#); [Tuchen et al., 2019](#)), less is known about the temporal variability of the Atlantic STCs. The majority of studies on STC variability has focused on the Pacific STCs. From these studies, two findings stand out: First, numerical studies show that on interannual to decadal time scales transport anomalies at the western boundary and in the interior basin are anti-correlated showing a seesaw-like relation ([Lee and Fukumori, 2003](#); [Capotondi et al., 2005](#); [Schott et al., 2007](#)). On these time scales western

boundary and interior transport anomalies partly compensate each other. *Lee and Fukumori (2003)* attribute the partial compensation to two different mechanisms: changes at the western boundary are suggested to be forced by adjustment to variations in Ekman pumping while interior transport changes are associated with near-equatorial wind stress changes. In contrast, *Capotondi et al. (2005)* argue that both western boundary and interior transport variations are associated with baroclinic adjustment to Rossby waves due to large scale changes of the wind stress curl. Knowledge about this anti-correlation is based on numerical studies for the Pacific Ocean and has so far not been shown for the Atlantic Ocean. Second, in observational (*McPhaden and Zhang, 2002, 2004*) and numerical studies (*Zhang and McPhaden, 2006; Lübbecke et al., 2008; Farneti et al., 2014*) it has been shown that transport variations of the Pacific STCs on decadal time scales can be linked to tropical sea surface temperature (SST) variability on the same time scales. Phases of anomalously large STC transport coincide with phases of anomalously low tropical Pacific SST and vice versa (e.g. *McPhaden and Zhang, 2002, 2004*). Two possible mechanisms on how the STCs can drive SST variability have been proposed. First, *Gu and Philander (1997)* described how temperature anomalies are subducted in the subtropics and transported equatorward by a constant geostrophic transport as part of the lower branch of the STCs ( $\overline{vT'}$  mechanism; with  $v$  being the meridional transport and  $T$  the temperature with the overbar marking the mean and the prime marking anomalies relative to the mean). This scenario implies that subducted temperature anomalies are observed in the upwelling regions with a considerable time lag. In fact, travel times of subducted particles could range from years to even decades when considering the possibility of multiple recirculations before eventually reaching the upwelling areas. In the second mechanism ( $v'\overline{T}$ ), subducted water with constant temperature is brought towards the tropics by an anomalously strong or weak equatorward thermocline layer transport (*Kleeman et al., 1999*). It is proposed that the rate at which subtropical water is transported towards the tropics rather than its temperature anomaly drives tropical SST anomalies by dynamical changes in the equatorial and eastern boundary upwelling rate. The  $v'\overline{T}$  mechanism could explain the fast response of SST anomalies to transport changes described in previous studies. For the Pacific Ocean the model study of *Hazeleger et al. (2001)* could show that the response of tropical temperature anomalies to extra-tropical forcing is small and rather local wind stress anomalies are suggested to drive variability both in the subtropics and tropics. Based on this and other studies, the  $v'\overline{T}$  mechanism by *Kleeman et al. (1999)* is deemed more likely (e.g. *McPhaden and Zhang, 2002; Schott et al., 2004*). However, in the model by *Kleeman et al. (1999)* tropical SST anomalies are mainly driven by subtropical wind stress changes (poleward of  $\pm 23^\circ$ ) whereas *Nonaka et al. (2002)* show that equatorial wind stress variability plays an equally important role in modulating equatorial SST anomalies on interannual to decadal time scales. Recently, *Graffino et al. (2019)* analyzed the role of differing magnitudes and locations of wind stress forcing in driving Pacific STC and SST variability. They conclude that equatorial wind stress anomalies are not responsible for STC changes but force local SST anomalies through thermocline adjustment

to local wind stress anomalies, whereas subtropical wind stress anomalies have the strongest impact on changes in STC transport. To date, studies on STC transport variability in the Atlantic Ocean have been limited to using either a forced ocean model ([Hüttl and Böning, 2006](#)) or an ocean assimilation model ([Rabe et al., 2008](#)). These studies focus mainly on the impact on the equatorial current system. [Rabe et al. \(2008\)](#) suggest that the STCs and the Equatorial Undercurrent (EUC) are connected on pentadal (5-year) and longer time scales. In a so-called loop response, changes in the wind-driven surface branches of the STCs, first lead to a response in the EUC followed by the thermocline layer transport convergence. On global warming time scales, [Oschlies et al. \(2018\)](#) suggested that the ventilated tropical thermocline becomes shallower and stronger leading to reduced oxygen undersaturation in upwelling regions and thus to a reduction in oxygen uptake emphasizing the possible role of the STCs in ocean deoxygenation. Since the start of the Argo program in the early 2000s, the number of observational data in all oceans increased dramatically and has already been used to derive a realistic mean-state of the Atlantic STCs ([Tuchen et al., 2019](#)). The first aim of this study is to provide transport time series of the horizontal STC branches from observations such as Argo float data, moored velocity data at the western boundary and satellite wind data accompanied by reanalysis products to extend the analysis further into the past. The dominant temporal scales of transport variability of the horizontal STC branches and their components are identified followed by a quantification of both the relation between thermocline layer transport anomalies at the western boundary and in the interior and the relation between STC transport variability and SST variability in the tropical Atlantic Ocean. SST fluctuations are known to have considerable effects on various climate parameters. On interannual and decadal time scales tropical Atlantic SST anomalies are connected to climate hazards such as extreme rainfall or droughts both over Brazil and Africa (e.g. [Carton et al., 1996](#)) mostly associated with the meridional or zonal mode. Therefore, skillful prediction of tropical SST variations has been the subject of numerous studies in order to better forecast future extreme events (e.g. [Chang et al., 1998](#)). The present study is structured as follows. Section [4.2](#) describes the data products which were used to derive the transport time series of the horizontal branches of the STCs and the SST time series. Section [4.3](#) provides an overview of the methods. In section [4.4](#) we present the results which are divided into a description of the observed transport variability, the relation between western boundary and interior transport anomalies and the connection of STC variability to tropical SST variability. The presented results are then summarized and complemented with a conclusion in section [4.5](#).

## 4.2 Data

In this section, we provide an overview of the data that were used in this work. Transports at thermocline level are mainly derived from hydrographic data from the Roemmich-Gilson Argo climatology (from here on referred to as RG-clim; [Roemmich and Gilson, 2009](#)) and from

the ECMWF Ocean Reanalysis System version 4 (ORAS4; [Balmaseda et al., 2013](#)). RG-clim and ORAS4 provide monthly temperature and salinity data on a  $1^\circ \times 1^\circ$  grid for a time period from 2004 to 2019 (RG-clim) and 1980 to 2017 (ORAS4), respectively. Additionally, ORAS4 provides horizontal ocean velocities. Under the assumption that below the wind-driven surface layer the flow is generally in geostrophic balance we use total velocities from ORAS4 for comparison. In order to quantify transport uncertainties at the western boundary due to sparse coverage by Argo floats, thermocline layer transport calculations in the southern hemisphere are complemented by moored velocity data at  $11^\circ$  S from 2013 to 2018 (update of [Hummels et al., 2015](#)). At  $11^\circ$  S, four moorings - arranged on a cross-shore array - have been operating from 2013 to present. By applying a gap filling method described in [Schott et al. \(2005\)](#) and [Hummels et al. \(2015\)](#) an alongshore velocity data set with a temporal resolution of 2.5 days and a spatial resolution of 5 km (horizontal) and 10 m (vertical) is derived.

Ekman transports are calculated from ocean surface wind speed data (typically 10 m above sea surface). Here, we use two long-term reanalysis products with a monthly resolution, ERA-interim ([Dee et al., 2011](#)) and ERA5 ([Hersbach and Dee, 2016](#)), and two consecutive satellite scatterometer missions with weekly resolution and an overlap of about 2.5 years, QuikSCAT ([Ricciardulli and Wentz, 2015](#)) from July 1999 to November 2009 and ASCAT ([Ricciardulli and Wentz, 2016](#)) from March 2007 to present. Both wind reanalysis products span the time period from 1980 to 2019. ERA-interim is being phased out and data stopped in August 2019 whereas ERA5 provides data to present. All wind products are provided at a  $1/4^\circ$  horizontal resolution. To analyze the link between STC transport variability and tropical SST variability on interannual to decadal time scales, SST time series from the Optimum Interpolation SST Analysis Version 2 (OI-SST; [Reynolds et al., 2007](#)) are used. Daily maps with a horizontal resolution of  $1/4^\circ$  are provided from January 1982 to present.

## 4.3 Methods

### 4.3.1 Thermocline Transports

Equatorward transport within the thermocline layer is primarily associated with geostrophic flow. However, geostrophic flow is also present above the thermocline layer where it reduces the wind-driven poleward transport in the tropics ([Schott et al., 2004](#)). In order to derive geostrophic transports from hydrographic properties we mainly follow the approach of [Tuchen et al. \(2019\)](#) and only give a brief overview of their methods and definitions of the horizontal STC branches. In a first step, hydrography from RG-clim and ORAS4 are used to obtain maps of dynamic height for the tropical Atlantic Ocean. From the zonal pressure gradient, which is a consequence of zonal differences in dynamic height, meridional geostrophic velocities relative to a level of no motion at 1000 dbar are calculated. Zonal geostrophic velocities are derived analogously from the meridional dynamic height gradients. Here, we reference relative

geostrophic velocities from RG-clim by prescribing the time-mean (2004-2019) horizontal displacement from Argo floats within a parking pressure level range between 850 – 1150 dbar as the reference velocity at 1000 dbar. Therefore, horizontal displacement values are binned and averaged in  $1^\circ \times 1^\circ$  boxes before being smoothed with an objective mapping routine (influence radius of  $2^\circ$  and a cut-off radius of  $4^\circ$ ). Close to the western boundary, coverage by Argo floats is naturally sparse and RG-clim fails to resolve the westernmost part of the tropical Atlantic introducing a transport uncertainty which has already been described in [Tuchen et al. \(2019\)](#). Here, we address the transport uncertainty at the western boundary by comparison to moored velocity data along  $11^\circ$  S and to velocity data provided by ORAS4. In the mean state, ORAS4 and mean ship section data along  $11^\circ$  S both reveal an underestimation of transport of about  $2\text{ Sv}$  at the western boundary in the southern hemisphere by Argo data ([Tuchen et al., 2019](#)). At  $10^\circ$  N, there is no comparable observational data set for the northern hemisphere western boundary transport. However, meridional geostrophic velocity from Argo float data shows a mean northward transport west of  $55^\circ$  W which appears to be cut off due to data coverage. It is therefore suggested that meridional transport from Argo float data rather overestimates the mean zonally accumulated equatorward transport at  $10^\circ$  N by missing parts of the northward transport at the western boundary.

Geostrophic transport derived from the hydrographic properties of ORAS4 is also missing the westernmost part of the western boundaries due to the calculation of meridional geostrophic velocities between zonal grid points of temperature and salinity leading to an overall reduction of  $0.5^\circ$  at each site of the basin. While RG-clim is referenced with Argo float displacement data, we use 370 dbar velocities provided by ORAS4 to reference geostrophic velocities derived from the hydrographic properties in ORAS4. This pressure level is chosen in order to cover as many grid points as possible at the western boundary that are still deeper than the lower boundary of the STCs.

Eventually, thermocline layer transports at  $10^\circ$  N and  $10^\circ$  S are derived by integrating meridional geostrophic velocities between a lower ( $26.0\text{ kg m}^{-3}$  isopycnal) and an upper boundary (seasonally varying depth between 30 – 70 m) following the definitions of [Tuchen et al. \(2019\)](#). At  $26.0\text{ kg m}^{-3}$  the sign of meridional geostrophic transport reverses. This is true for both the mean state and for the time series (not shown). Seasonal outcropping of isopycnals of the thermocline layer is only observed in the eastern parts of the subtropics and is treated as an absence of thermocline layer transport in our calculation. However, the surface layer transport, which is chosen according to the depth at which the absolute meridional velocity changes its sign from poleward to equatorward, is unaffected by outcropping of isopycnals as it is bounded by depth. In the case of the  $11^\circ$  S moored velocity data, the lower boundary of the thermocline layer is derived from the mean density field from five cross-shore ship sections along the mooring array ( $26.0\text{ kg m}^{-3}$  isopycnal as well). The upper boundary is set to 60 m which marks the zonally averaged annual mean depth of meridional velocity reversal from ORAS4 at this latitude ([Tuchen et al., 2019](#)).

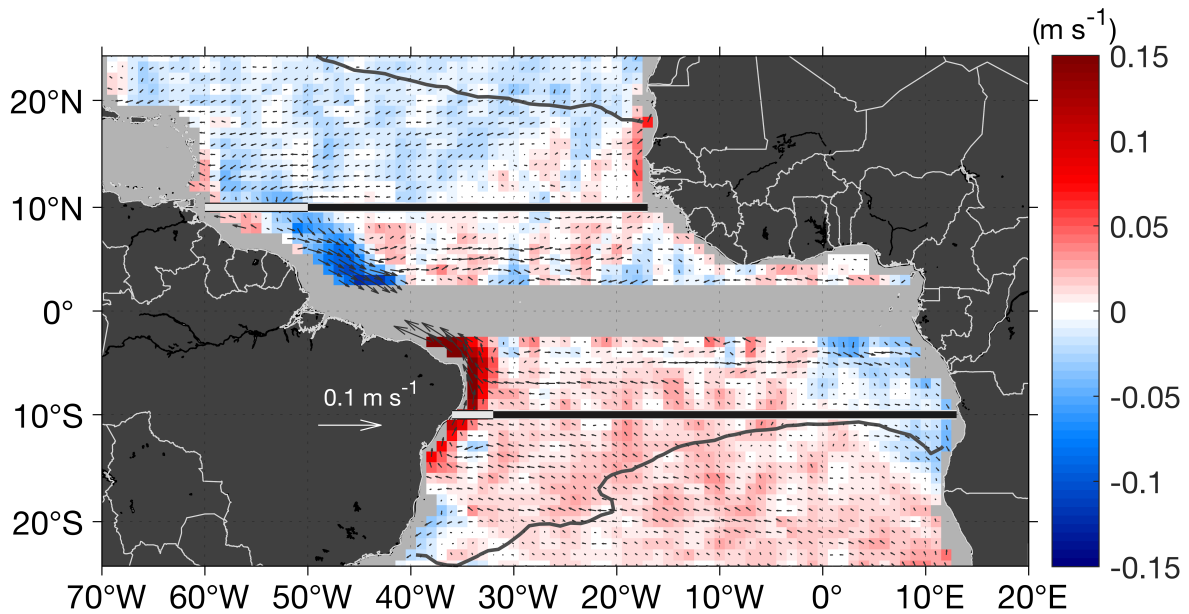


**Figure 4.1:** Mean absolute geostrophic velocities in the tropical Atlantic Ocean between 2004-2019 within the thermocline layer ( $25.5 \text{ kg m}^{-3}$  isopycnal) derived from the Roemmich & Gilson Argo climatology (Roemmich and Gilson, 2009). Arrows show the horizontal geostrophic velocity; the color shading indicates the magnitude of the meridional component of the absolute geostrophic velocity with red (blue) showing northward (southward) flow. The seasonal outcropping of the  $25.5 \text{ kg m}^{-3}$  isopycnal is superimposed (grey isoline) in both hemispheres. Zonal sections at  $10^\circ \text{ N}$  and  $10^\circ \text{ S}$  are divided into a western boundary (white line) and an interior part (black line) at  $50^\circ \text{ W}$  and  $32^\circ \text{ W}$  respectively.

Within the thermocline layer the pattern of the mean horizontal geostrophic velocity reveals the pathways of the equatorward transport of the STCs (Fig. 4.1). At around  $15^\circ \text{ S}$ , the bifurcation of the South Equatorial Current (SEC) into the northward flowing NBUC and the southward flowing Brazil Current marks the division between subducted water moving equatorward as part of the southern STC or AMOC and water being recirculated within the subtropical gyre of the southern hemisphere. The southern section at  $10^\circ \text{ S}$  is therefore chosen to be equatorward of the bifurcation area (see Fig. 4.1). The southern STC exhibits a substantial exchange window in the interior basin in the 16-year Argo climatological mean. The interior pathway is largely limited in the northern hemisphere by the mean position of the Intertropical Convergence Zone (ITCZ) and the resulting potential vorticity barrier (Malanotte-Rizzoli et al., 2000). In order to examine the variability of STC transport in more detail, the zonal sections at  $10^\circ \text{ N}$  and  $10^\circ \text{ S}$ , at which transport time series are derived, are divided into a western boundary and an interior part at  $50^\circ \text{ W}$  ( $32^\circ \text{ W}$ ) at  $10^\circ \text{ N}$  ( $10^\circ \text{ S}$ ) as indicated in Fig. 4.1.



### 4.3.2 Ekman and surface layer transports

Poleward transport in the surface layer of the tropical Atlantic is mainly driven by the north- and south-easterly trade winds forcing poleward Ekman transport in both hemispheres and leading to Ekman divergence at the equator. Here, we use four different wind products which provide zonal and meridional wind speed at 10 m height above the sea surface. From wind speed ( $\vec{u}$ ), we obtain wind stress ( $\vec{\tau}$ ) via the Bulk formula calculation:

$$\vec{\tau} = \rho_a * c_d * |\vec{u}| * \vec{u} \quad (4.1)$$

using a reference density  $\rho_a = 1.22 \text{ kg m}^{-3}$  and a drag coefficient  $c_d = 0.0013$ . Meridional Ekman transport is a function of zonal wind stress and the latitude-dependent Coriolis parameter. In case the products are providing weekly data (ASCAT and QuikSCAT) monthly means are derived for all months which provide at least four data points.

In the surface layer of the tropical oceans, poleward Ekman transport is in opposition to generally equatorward geostrophic transport due to zonal pressure gradients. Therefore, when combining both components, we refer to the net surface layer transport divergence since the Ekman divergence dominates the surface layer but is reduced by the geostrophic convergence. Different approaches are compared: surface layer transports are derived directly from velocity data (ORAS4 and 11° S mooring) or calculated as the sum of between Ekman transport and geostrophic transports. The lower boundary of the surface layer is the same seasonally varying depth used as the upper boundary for the thermocline layer described in 4.3.1.

## 4.4 Results

### 4.4.1 Transport variability of the horizontal STC branches

Monthly thermocline layer transports are derived and cumulated along the zonal sections at 10° N and 10° S, from the eastern to the western boundary. The difference between both hemispheres yields the monthly thermocline layer transport convergence time series (Fig. 3.2a). Transports vary between approximately 7 – 14 Sv. In general, we find good agreement between ORAS4 and ORAS4-geostr as expected. However, there are larger differences between the geostrophic transport of RG-clim and both ORAS4-based products which mainly originate from differences at the western boundary (Fig. 3.2b and d). As already indicated in Fig. 3.2a the dominant signal in all time series is the seasonal cycle with a minimum in boreal summer and a maximum in boreal winter which is most pronounced in RG-clim. A spectral analysis (not shown) confirms the dominance of the annual signal but also reveals elevated variability at the semiannual cycle and the 120-day period. At periods longer than one year, no spectral peaks that are significant against an AR-1 red noise spectrum could be observed. Nevertheless, interannual and longer-period fluctuations are evident throughout the time series. For

instance, we observe a transport convergence weakening from 2005 until about 2010 followed by a strengthening until about 2016. Interannual transport fluctuations will be further discussed in the next sections.

By separating the thermocline layer transport convergence into its components at  $10^{\circ}$  N and  $10^{\circ}$  S, both further divided into a western boundary and an interior contribution (see also Fig. 4.1), good agreement between the three products in the interior parts is observed (Fig. 4.2c and e), whereas especially the southern hemisphere western boundary transport reveals obvious differences between RG-clim and the ORAS4 products. This is mainly due to a better coverage of the western boundary by ORAS4 leading to both enhanced northward western boundary transport at  $10^{\circ}$  S (Fig. 4.2b) and reduced equatorward transport at  $10^{\circ}$  N (Fig. 4.2d). When comparing western boundary transport in the southern hemisphere from ORAS4 to mooring data at around  $11^{\circ}$  S we find a similar seasonal evolution and comparable magnitude (Fig. 4.2d). Note that the  $11^{\circ}$  S-mooring transport is limited to longitudes west of about  $33.85^{\circ}$  W. However, when considering thermocline layer transports from ORAS4-geostr only between  $36^{\circ}$  W and  $34^{\circ}$  W, both time series still agree well (not shown). In contrast, thermocline layer transport at the western boundary derived from RG-clim appears to underestimate this particular branch of the STCs. Thermocline layer meridional transport is on average southward in the northern hemisphere with occasional transport reversals both at the western boundary and in the interior basin (Fig. 4.2b-c). In comparison, transport in the southern hemisphere is generally stronger and persistently northward throughout the presented time period (Fig. 4.2d-e).

Above the thermocline layer, equatorward geostrophic transport is largely exceeded by the wind-driven poleward Ekman transport. In total, a net surface layer transport divergence exists between  $10^{\circ}$  N and  $10^{\circ}$  S (Fig. 4.3a). Here, we subtract the geostrophic transport convergence of RG-clim (ORAS4-geostr) from the Ekman divergence of ASCAT (ERA5) for the period in which the particular time series overlap. In addition, surface layer transports are directly calculated from total velocities provided by ORAS4. All products agree well on the seasonality which is mainly in phase with the seasonal evolution of the thermocline layer transport convergence: a maximum in boreal winter and a minimum in boreal summer. However, analogously to the thermocline layer, the largest differences in magnitude are observed at the western boundary in both hemispheres (Fig. 4.3b and d) while interior transports show good agreement (Fig. 4.3c and e). At  $10^{\circ}$  S, geostrophic transport in the surface layer is northward at the western boundary compensating the poleward Ekman transport (Fig. 4.3d), while western boundary surface layer transport at  $10^{\circ}$  N is mainly northward supporting the wind-driven transport. Note that due to the small zonal extent of the western boundary component as part of the zonal sections at  $10^{\circ}$  N and, especially,  $10^{\circ}$  S, the Ekman transport component is rather small compared to Ekman transport in the interior which is cumulated over a larger distance. Besides the dominant annual and semiannual cycle, again, no statistically significant spectral peaks are present at interannual to decadal time scales, although a similar oscillation

as described before for the thermocline layer transport convergence can be observed: a minimum of transport divergence at around 2010 is followed by a strengthening until about 2013.

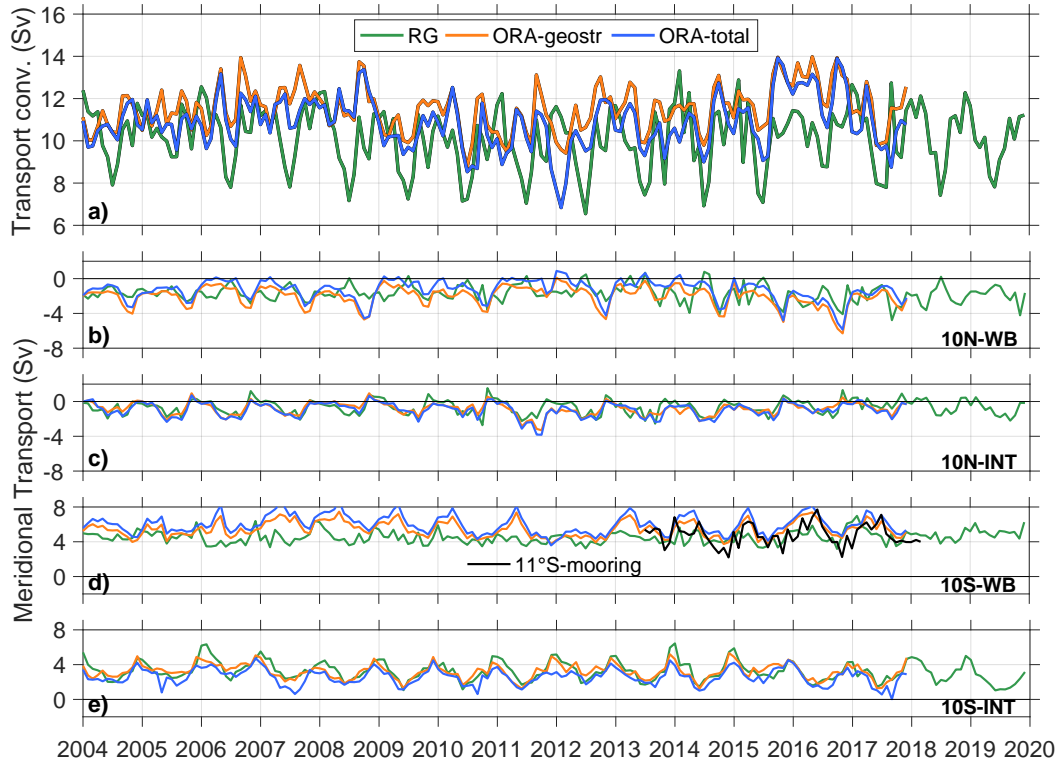


**Figure 4.2:** Monthly time series of (a) thermocline layer transport convergence between  $10^{\circ}$  N and  $10^{\circ}$  S from RG-clim (green), from the geostrophic component of ORAS4 (orange) and from total ORAS4 (blue) and thermocline layer transport (b) along the western boundary at  $10^{\circ}$  N, (c) within the interior at  $10^{\circ}$  N, (d) along the western boundary at  $10^{\circ}$  S and (e) within the interior at  $10^{\circ}$  S. Note that the  $11^{\circ}$  S mooring transport time series in (d) is calculated between  $35.85^{\circ}$  W and  $33.85^{\circ}$  W. Positive (negative) values indicate northward (southward) transport (b-e).

The relative importance of the representation of the western boundary in the data products becomes even more obvious in the climatological cycles of the thermocline layer and surface layer transport components (Fig. 4.4). In the thermocline layer, the seasonal cycle is most pronounced in RG-clim with minimum convergence values around 8 Sv in boreal summer (Fig. 4.4a). This is due to a distinct minimum of equatorward transport at  $10^{\circ}$  N at the western boundary in boreal summer which is not reproduced in the ORAS4 products (Fig. 4.4b). Generally, in both hemispheres all three products agree well for the interior but show considerable differences at the western boundary (Fig. 4.4b-c). The differences between the two transport estimates based on ORAS4 must essentially originate from the 0.5 data loss that the geostrophic transport derivation requires and emphasizes the importance of a good representation of the western boundary. Overall, at thermocline level, the climatological cycles from

RG-clim suggest that the seasonal cycle of the convergence is mainly driven by the seasonality at the western boundary in the north and the interior in the south which shows concurrent minimum equatorward transport in boreal summer.

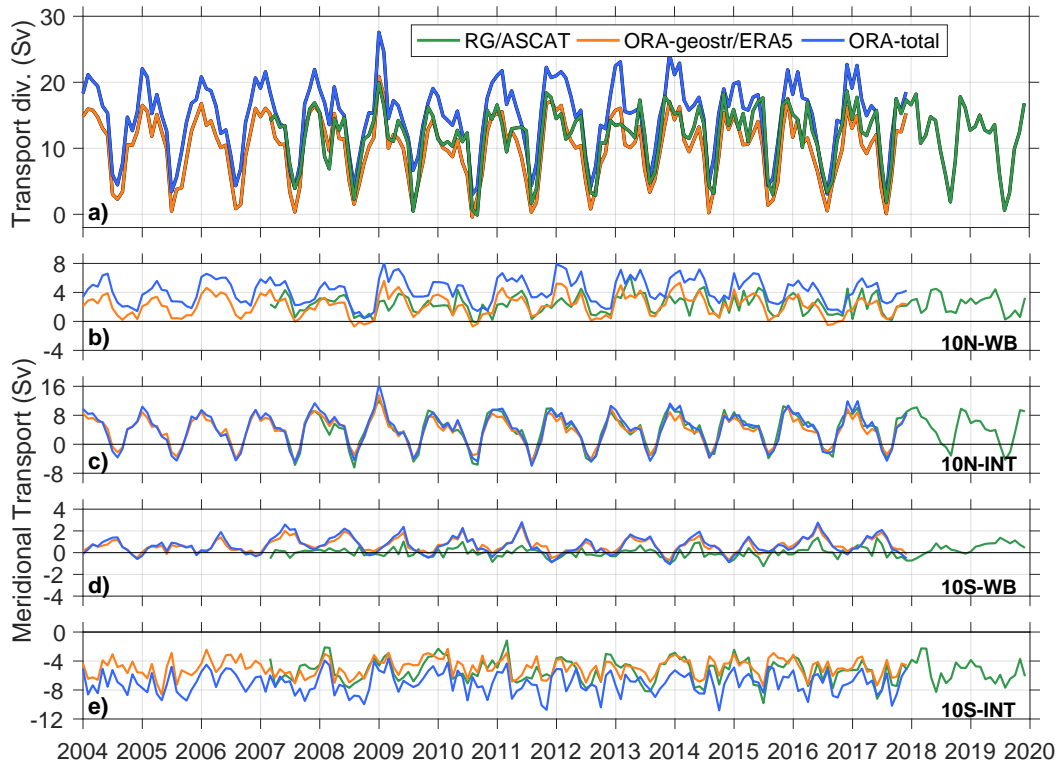


**Figure 4.3:** Monthly time series of (a) surface layer transport net divergence (geostrophy + Ekman) between  $10^{\circ}\text{N}$  and  $10^{\circ}\text{S}$  from RG-clim / ASCAT (green), from ORAS4 / ERA5 (orange) and total ORAS4 (blue), meridional surface layer net transport (b) along the western boundary at  $10^{\circ}\text{N}$ , (c) within the interior basin at  $10^{\circ}\text{N}$ , (d) along the western boundary at  $10^{\circ}\text{S}$ , and (e) within the interior basin at  $10^{\circ}\text{S}$ . Positive (negative) values indicate northward (southward) transport (b-e).

The Ekman divergence climatologies are calculated for the four different wind products which all agree well on the seasonality (Fig. 4.4d) and show some difference in magnitude away from the annual minimum which occurs in late boreal summer. The seasonal cycle of Ekman divergence exhibits peak-to-peak amplitudes of more than  $10\text{ Sv}$  and is mainly driven by the northern hemisphere interior component where Ekman transports even reverse to equatorward transport to show a distinct minimum during late boreal summer (Fig. 4.4e). However, besides a statistically significant annual cycle we also observe a semiannual cycle likely due to a relative minimum of poleward Ekman transport in the interior at  $10^{\circ}\text{N}$  in boreal winter to spring superimposed by a minimum in Feb/March in the interior at  $10^{\circ}\text{S}$ . In general, all four components of the Ekman divergence (Fig. 4.4e-f) are in good agreement in terms of both seasonality and magnitude. In the following, because of the good agreement between all wind

products, further analysis involving Ekman transports is carried out using data from one re-analysis product (ERA5) and one satellite product (ASCAT) only. ASCAT aligns with RG-clim better in time compared to QuikSCAT. It is recently shown that ERA5 wind speeds have a 20% improvement in comparison to ERA-interim (*Belmonte Rivas and Stoffelen, 2019*).

As previously described, the overall surface layer transport is a combination of Ekman transport and geostrophic transport. Here, we estimate both components individually and also compare them to surface layer transports directly derived from ORAS4 (Fig. 4.4g). Since the Ekman transport is dominating the surface layer, all products show poleward transport throughout the whole year leading to an overall surface layer divergence while also agreeing on the same seasonality as the Ekman divergence (Fig. 4.4d). The geostrophic component reduces all four transport components in the surface layer to less poleward or even equatorward. In the southern hemisphere the strong northward western boundary current exceeds the southward Ekman transport in the surface layer and shows an overall equatorward transport of up to 2 Sv in boreal summer (Fig. 4.4i).

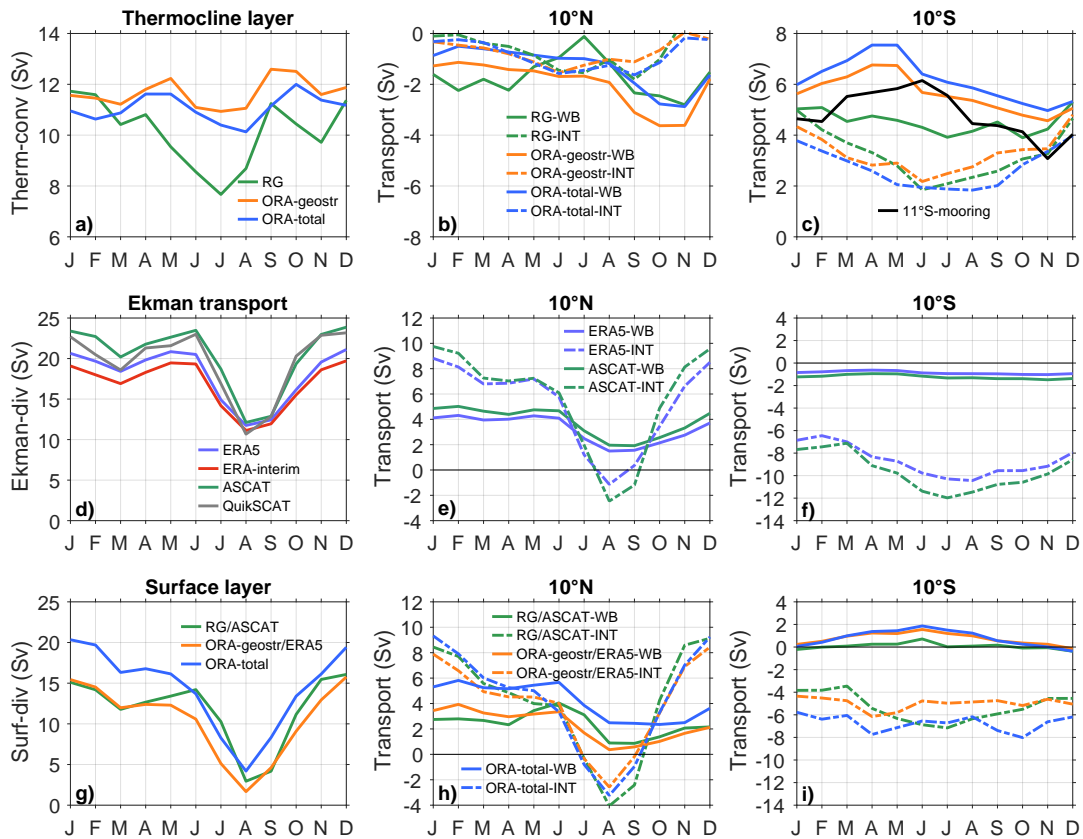


**Figure 4.4:** Monthly climatology of (a-c) thermocline layer transport convergence, (d-f) Ekman divergence and (g-i) surface layer net divergence. (a), (d) and (g) are further separated into their individual transport components at 10° N (b, e, h) and 10° S (c, f, i). In each hemisphere, the transport is divided into a western boundary (WB, solid line) and an interior (INT, dashed line) transport contribution.

#### 4.4.2 Western boundary vs. interior transport anomalies

As shown in the previous section, the thermocline layer transport convergence and the surface layer transport divergence vary dominantly on seasonal time scales with a modulation on interannual and longer scales. In this section we will show that even though interannual variability of the total thermocline layer transport convergence might be relatively weak, interannual transport anomalies at the western boundary and in the interior basin show a remarkable relation. First, we separate the thermocline layer transport convergence time series into the western boundary and the interior components in both hemispheres (as indicated in Fig. 4.1) before filtering out the dominating seasonal signal by applying a 2-year running mean.

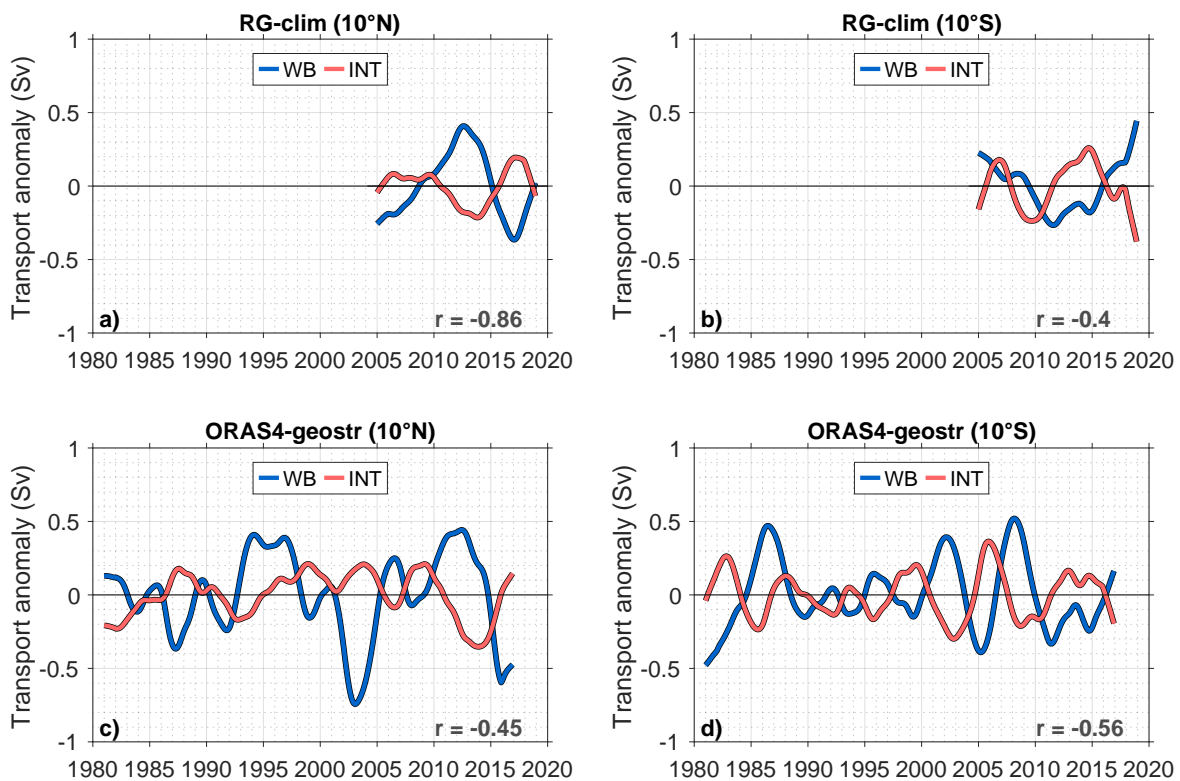


**Figure 4.5:** Time series of thermocline layer transport anomaly at  $10^{\circ}$  N (left panels) and  $10^{\circ}$  S (right panels) for RG-clim (upper panels) and ORAS4-geostr (lower panels). Transport anomalies are separated into a western boundary (WB; blue) and interior (INT; red) component within each hemisphere. A 2-year running mean is applied to all time series. Cross-correlation coefficients are significant at the 95% confidence interval.

In both hemispheres, the time series of interannual transport fluctuations at the western boundary (WB) and in the interior (INT) are out of phase for both RG-clim and ORAS4-geostr (Fig. 4.5). Transport anomalies at the western boundaries and anomalies in the interior basin are highly anti-correlated on interannual time scales and as a result partly compensate each other.

In the northern hemisphere, maximum cross-correlation coefficients are as high as  $-0.86$  for RG-clim (Fig. 4.5a) and  $-0.45$  for ORAS4-geostr (Fig. 4.5c) respectively. Note that the anti-correlation in ORAS4-geostr is more pronounced in the later phase of the time series that overlaps with RG-clim. The observed WB-INT relation can essentially be described as a seesaw in which the two components are generally in opposite phases. For both products, meridional transport anomalies in the interior reach about  $0.3\text{ Sv}$  and are slightly smaller compared to western boundary transport anomalies (up to  $0.5\text{ Sv}$  and occasionally above at the western boundary in ORAS4-geostr). In the southern hemisphere, a similar anti-correlation is observed (Fig. 4.5b and d). There, transport anomalies show comparable amplitudes as in the northern hemisphere and cross-correlation coefficients are lower for RG-clim ( $r = -0.40$ ) and about comparable for ORAS4-geostr ( $r = -0.56$ ). Similar to  $10^\circ\text{ N}$ , in the beginning of time series, the anti-correlation in ORAS4-geostr is not as pronounced as it is in the later part from about 1996 onward. Interestingly, although in the mean state of the Atlantic STCs, the northern hemisphere components only contribute with about a third to the total mean convergence, their fluctuations are similar in amplitude compared to those in the southern hemisphere. In order to identify the dominant time scale of this anti-correlation a cross-spectrum analysis was carried out (not shown) which does not favor a certain time scale but rather shows a similar anti-correlation at all time scales. Longer time series will be needed to gain more insight into the time scale dependence of the WB vs. INT relation.

Transport anomalies at the western boundary and in the interior are derived from integrated geostrophic velocities separated at a fixed longitude at  $50^\circ\text{ W}$  ( $32^\circ\text{ W}$ ) at  $10^\circ\text{ N}$  ( $10^\circ\text{ S}$ ) and are zonally cumulated. In order to find out which part of these zonal subsections dominates the WB and INT variability in each hemisphere we linearly regress the thermocline layer meridional geostrophic velocities at  $25.5\text{ kg m}^{-3}$  point-by-point onto the interannual interior transport anomaly time series of both hemispheres (Fig. 4.6).

Positive values indicate a strong connection between INT transport anomalies and geostrophic velocity anomalies on interannual time scales. In the northern hemisphere the zonal section along  $10^\circ\text{ N}$  shows negative values at the western boundary and positive values east of  $50^\circ\text{ W}$  confirming the previously described general anti-correlation between WB and INT. In the southern hemisphere the INT transport anomalies are mainly driven by geostrophic velocity anomalies between  $30^\circ\text{ W}$  to  $20^\circ\text{ W}$  which are clearly anti-correlated to geostrophic velocity anomalies at the western boundary. In the eastern part, seasonal outcropping at this particular isopycnal further emphasizes the role of the western part of the subsection for the overall INT transport anomalies on interannual time scales. The linear regression of geostrophic velocity anomalies onto the hemispheric WB transport anomaly (not shown) reveals a much wavier pattern suggesting a larger role of e.g. Rossby waves which are excited close to the western boundary due to wind stress changes.

From the mean state of the STCs it is known that about three times more equatorward transport occurs at  $10^\circ\text{ S}$  compared to  $10^\circ\text{ N}$ . Is this interhemispheric asymmetry also observed

for interannual fluctuations? In order to find out which hemisphere ultimately dominates the interannual variability of the overall thermocline layer transport convergence, we use the combined hemispheric components (WB + INT) of the STCs. It shows that the thermocline layer transport convergence anomaly of the STCs undergoes an about pentadal oscillation (Fig. 4.7).

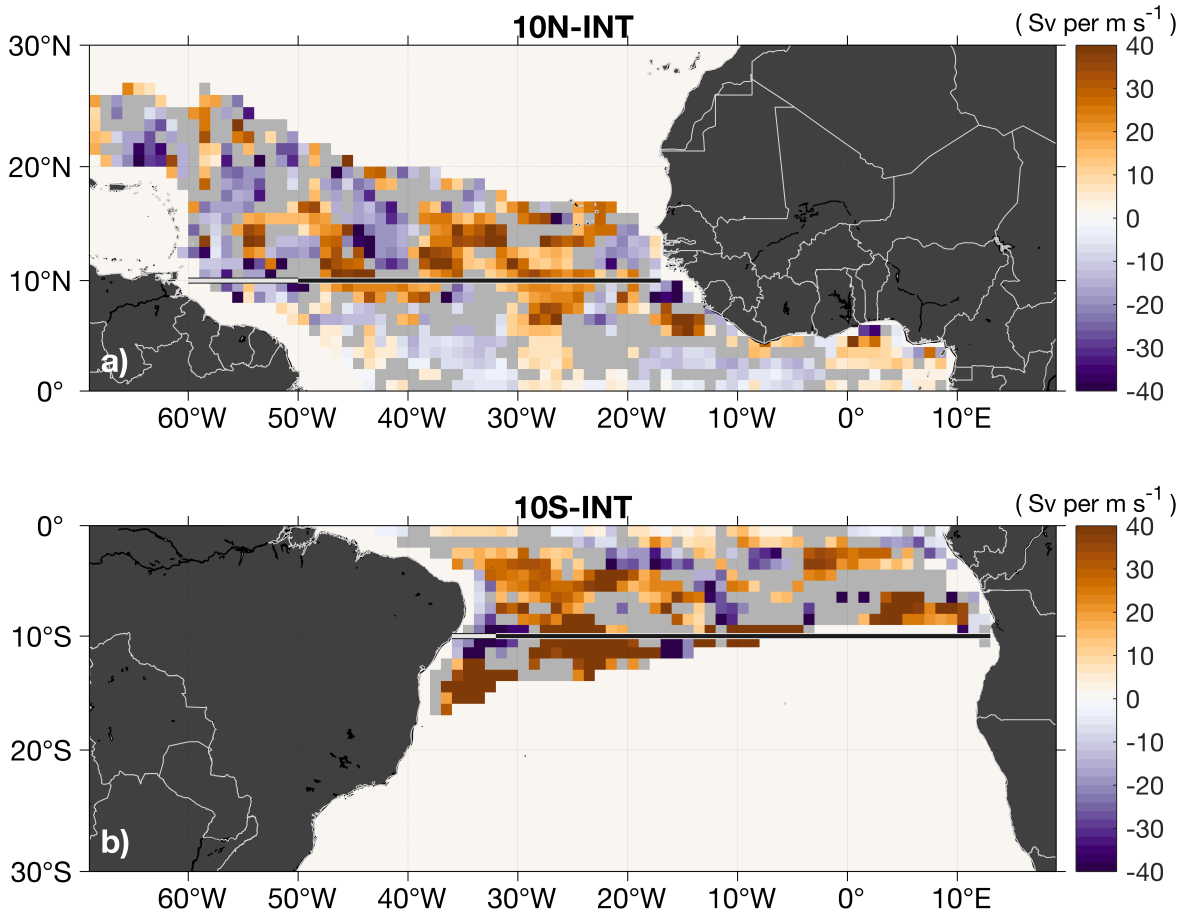


**Figure 4.6:** *Linear regression of meridional geostrophic velocity anomalies ( $25.5 \text{ kg m}^{-3}$  isopycnal) onto the interior thermocline layer transport anomaly for (a) the northern hemisphere and (b) the southern hemisphere from RG-clim. Statistically insignificant values are masked in grey. Shown are only grid points without seasonal outcropping of the  $25.5 \text{ kg m}^{-3}$  isopycnal. The zonal sections at  $10^\circ \text{ N}$  and  $10^\circ \text{ S}$  and their division into western boundary (white) and interior (black) are superimposed. A 2-year running mean is applied to the time series.*

RG-clim data reveals a weakening of thermocline layer transport convergence of about  $1 \text{ Sv}$  from the beginning of the time series in 2005 to 2010. From then on, the thermocline layer transport convergence strengthened by about  $1 \text{ Sv}$  over a time period of six years. However, it appears that generally one hemisphere dominates the total convergence. For RG-clim, first, mainly the southern hemisphere is responsible for the mentioned weakening of the thermocline layer transport convergence followed by a phase of equal contribution from both hemispheres



before a strengthening of the northern hemisphere STC causes the total convergence to also strengthen.

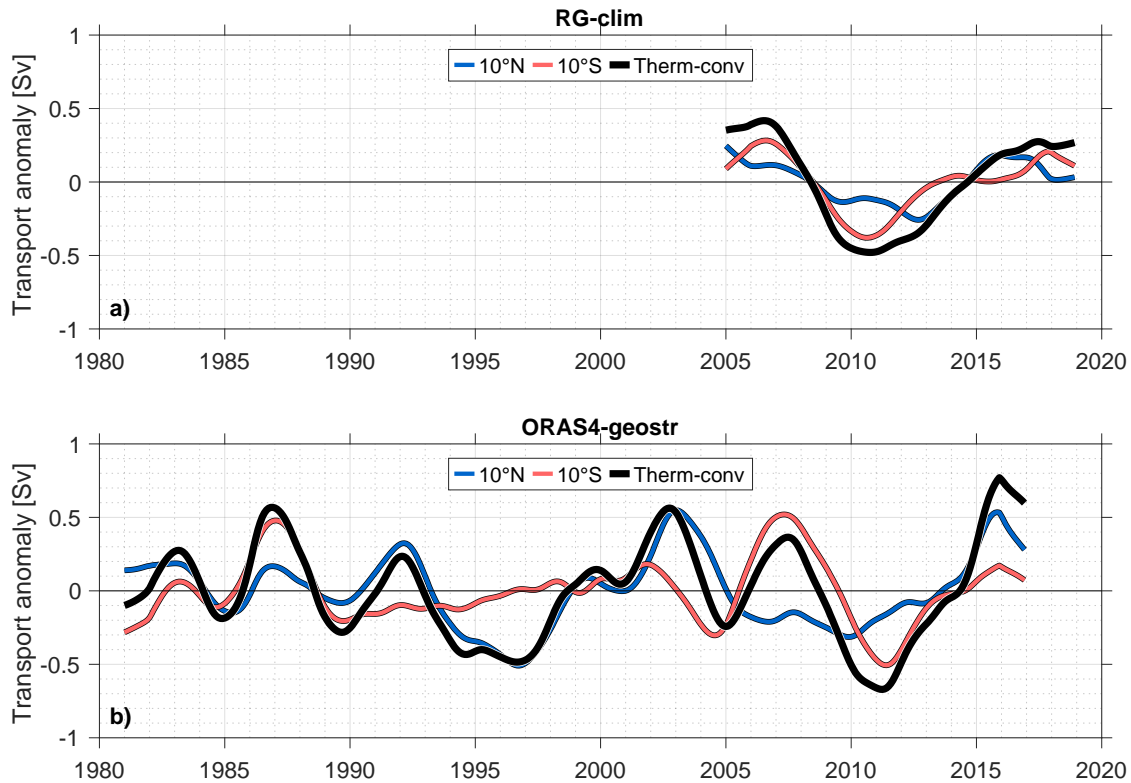


**Figure 4.7:** Time series of thermocline layer transport anomalies for (a) *RG-clim* and (b) *ORAS4*. Thermocline layer transport convergence anomalies (black) are separated into their northern hemisphere (blue) and southern hemisphere (red) component. A 2-year running mean is applied to the time series.

This change of dominant hemisphere is also found for the thermocline layer transport convergence anomaly time series from *ORAS4-geostr* (Fig. 4.7b). Besides agreeing on the dominant hemisphere for the time period in which both data products overlap, it further shows that before 2005 the northern hemisphere apparently dominated the thermocline layer transport convergence anomaly for about 15 years.

#### 4.4.3 Impact on sea surface temperature variability

The STCs are connecting the subtropical subduction regions with tropical upwelling areas along the equator and at the eastern boundary. In this section, we will analyze the connection of the different horizontal STC branches to equatorial SST variability on interannual to decadal time scales and discuss the observed time lags between the different STC components.

Smoothed time series (2-year running mean) of thermocline layer transport convergence anomalies from RG-clim and ORAS4-geostr are in good agreement and show variations on interannual to decadal time scales (Fig. 4.8a) and they lead equatorial SST anomalies by about 2 to 3 years (Fig. 4.8b). The particular cross-correlation coefficients at zero lag are rather small (Fig. 4.8a). Here, SST anomalies are based on a spatial average between 30° W to 10° W and 3° S to 1° N, where we find the strongest relation in a lag regression analysis of SST anomalies onto interior transport convergence anomalies (Fig. 4.11; described in more detail in the later part of this section). Transport anomalies vary between 0.7 Sv while SST anomalies are mainly observed in a range between 0.4° C. Notably, the cross-correlation indicates that stronger thermocline layer transport is followed by warmer SSTs.

For the Ekman divergence ( $r = -0.42$ ) and the surface layer net divergence anomalies ( $r = -0.51$ ) we find considerable anti-correlations at zero lag (Fig. 4.8c). However, maximum cross-correlation occurs for the surface layer transport anomalies when leading SST anomalies by about 3 months while Ekman transport anomalies appear to follow SST anomalies with a lag of about 4 months (Fig. 4.8d). When considering variability on longer time scales (here accomplished by applying a 5-year running mean to all time series), the sign of the previously observed time lags is not affected but the lags are more pronounced (Fig. 4.9b and d). At these time scales thermocline layer transport convergence anomalies appear to be clearly leading SST anomalies (Fig. 4.9a) but curiously, an increase of thermocline layer transport appears to be again related to increased equatorial SST. In the surface layer, the time lags increase for both ERA5 and ORAS4-total and the anti-correlations decrease at longer time scales but are still visible in the second half of the time series (Fig. 4.9c-d) possibly indicating less time scale dependence in terms of connection to equatorial SST anomalies than in the thermocline layer.

Following the results from the previous section 4.4.2, it is suggested that by analyzing the total thermocline layer transport convergence anomaly the individual contributions of the interior and western boundary components could be compensating each other. We therefore split the total thermocline layer transport convergence into a western boundary convergence and an interior convergence (Fig. 4.10) with the same boundaries as defined in section 4.3.1 (as indicated in Fig. 4.1) and analyze the observed variability both on shorter (2-year running mean smoothing) and longer (5-year running mean smoothing) time scales. For RG-clim the zero lag cross-correlation with SST anomalies increases drastically when considering only the interior convergence ( $r = -0.89$ ) while the convergence at the western boundary is positively correlated to SST anomalies ( $r = 0.64$ ) for the 2-year running mean case (Fig. 4.10a). However, RG-INT is led by SST anomalies by a small lag of 2 months while RG-WB is leading SST anomalies by about 1 year (Fig. 4.10b). At first, the lag between RG-INT and SST might be counter-intuitive. However, *Klinger et al. (2002)* and also *Capotondi et al. (2005)* noted for the Pacific Ocean that SST anomalies lead interior transport anomalies as well. *Capotondi et al. (2005)* attributed this striking temporal order to the continuous zonal evolution of the

STCs at  $10^\circ\text{N}/10^\circ\text{S}$ . They suggested that by zonally averaging along these sections an artificial time lag could evolve.

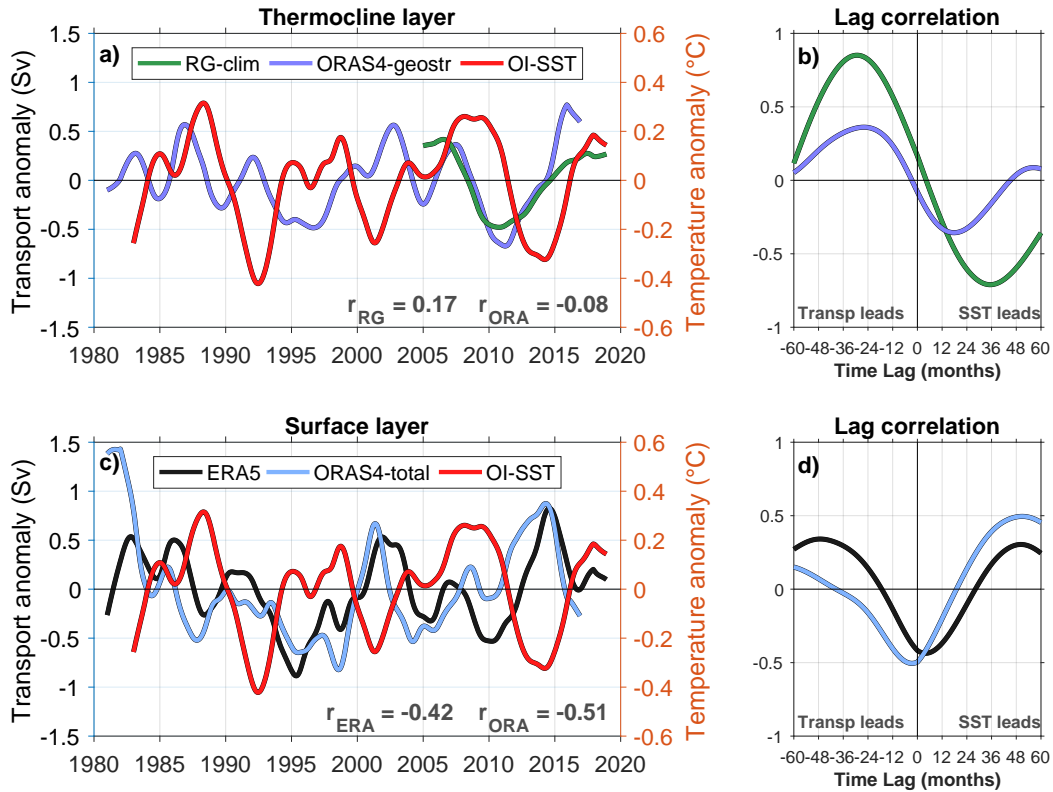


**Figure 4.8:** (a) Time series of anomalous thermocline layer transport convergence from RG-clim (green) and ORAS4-geostr (blue) with equatorial Atlantic ( $30^\circ\text{W}$ - $10^\circ\text{W}$ ,  $3^\circ\text{S}$ - $1^\circ\text{N}$ ) sea surface temperature anomaly from OI-SST (red) and (b) lag correlation analysis between the SST anomaly time series and RG-clim (green) and ORAS4-geostr (blue) thermocline layer transport convergence anomalies. (c) Time series of anomalous Ekman transport divergence from ERA5 (black), anomalous surface layer transport divergence from ORAS4 (light blue) and the same equatorial SST anomaly from OI-SST (red) as above and (d) lag correlation analysis between the SST anomaly time series and ERA5 (black) and ORAS4 (light blue) transport divergence anomalies. A 2-year running mean is applied to all time series. The zero lag cross-correlation coefficients with SST in (c) are significant at the 95% confidence interval.

Another possible explanation could be that SST and interior transport convergence anomalies are fluctuating more or less in parallel and are not impacting each other at shorter time scales. Initially, changes in zonal wind stress force anomalous Ekman transport and a net surface divergence anomaly evolves which, on the one hand, drives equatorial SST anomalies with a small temporal lag. On the other hand, by changing equatorial upwelling rates, the EUC must respond to less (more) demand of water with a weakening (strengthening) transport which ultimately affects the interior STC branches as a supplier of the EUC (e.g. [Rabe et al., 2008](#)).

By the time this signal reaches the interior transport branches, equatorial SST has already reacted to the wind forcing and appears to lead the interior transport convergence. Therefore, at shorter time scales, the interior thermocline layer branches of the STCs are suggested to not have a direct impact on equatorial SST but could rather respond with some delay to the same surface wind forcing.

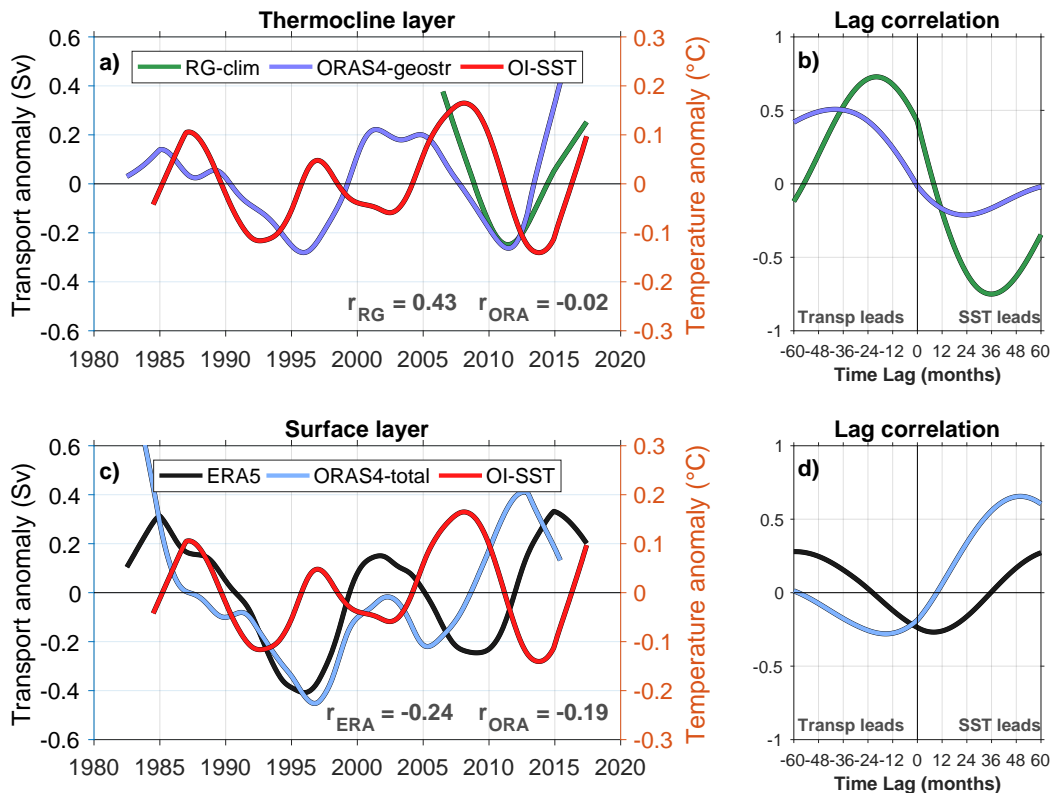


**Figure 4.9:** Same as Fig. 4.8 but with a 5-year running mean applied to all time series. The zero lag cross-correlation coefficients with SST in (a) between ORAS4-geostr and SST and both in (c) are significant at the 95% confidence interval.

For anomaly time series smoothed with a 5-year running mean, we find comparable anti-correlation coefficients between interior transport convergence anomalies and equatorial SST anomalies, but both RG-INT and ORA-INT now lead SST anomalies with a lag of about 2 months in RG-INT and a longer lag of about 6 months in ORA-INT (Fig. 4.10d). Importantly, the correlation between interior transport convergence and SST anomalies is negative on these time scales, implying that stronger interior transport is related to lower SSTs, in agreement with studies for the Pacific Ocean (e.g. [McPhaden and Zhang, 2002, 2004](#)).

The comparison between the results for the 2-year and 5-year running mean time series suggests that the STCs are modulating equatorial SST rather on longer time scales which is consistent with model studies for the equatorial Pacific showing that while the SST variability on interannual time scales is predominantly driven by equatorial wind forcing, a significant part

of the variability on decadal time scales is related to changes in the equatorward STC transport (*Nonaka et al., 2002; Lohmann and Latif, 2007; Lübbecke et al., 2008; Farneti et al., 2014*).

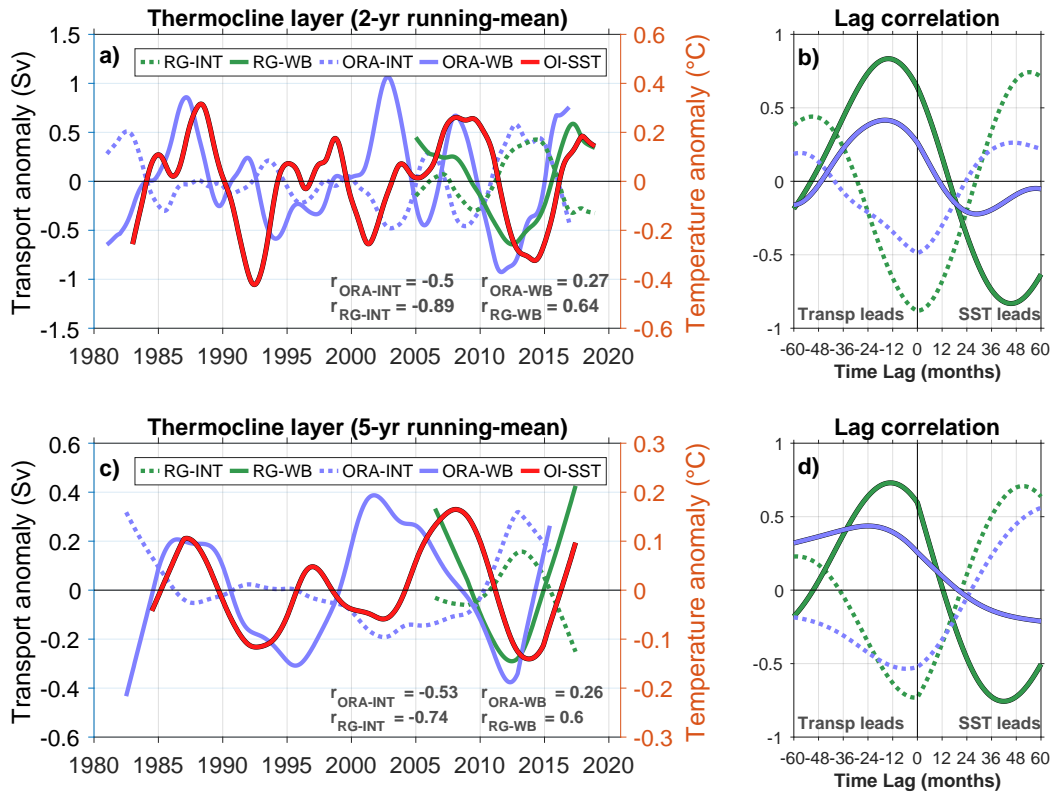


**Figure 4.10:** Time series of thermocline layer transport convergence anomaly divided into interior (dashed lines) and western boundary (solid lines) components for RG-clim (green) and ORAS4-geostr (blue) smoothed with (a) a 2-year running mean and (c) a 5-year running mean. Equatorial SST anomaly time series in (a) and (c) is the same as in Fig. 4.8 and Fig. 4.9, respectively. The lag correlation analysis between the equatorial SST anomaly time series and individual thermocline layer transport convergence anomalies for (b) 2-year running mean and (d) 5-year running mean smoothed time series. The individual cross-correlation coefficients with SST (95% significance level) are shown.

In order to quantify the SST response to STC changes, a linear point-by-point regression of the decadal (5-year running mean) RG-INT-CONV anomaly time series on decadal SST anomalies at the lag with maximum cross-correlation is carried out (Fig. 4.11a). The SST response at this time lag reaches values of more than  $-2^{\circ}\text{C}$  per Sv along an equatorial region between  $30^{\circ}\text{W}$  to  $10^{\circ}\text{W}$ . Another region with a strong negative SST response to positive INT-CONV changes exists in the eastern boundary upwelling region off Angola in the southern hemisphere. In contrast to decadal variations in the lower STC branch, we have seen that changes in the upper horizontal branches of the STCs are leading SST anomalies by about 12 months (Fig. 4.9d). The SST response to surface layer transport anomalies shows the strongest regression

coefficients in three regions: (1) southern central equatorial Atlantic, (2) along the eastern boundary upwelling off Mauritania and Senegal and (3) along the Angolan upwelling region.

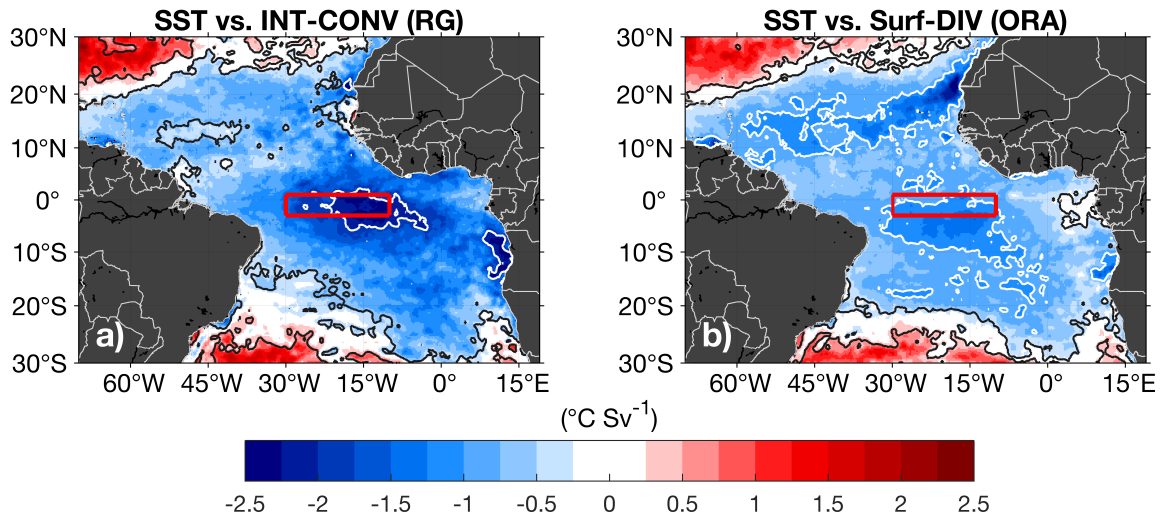


**Figure 4.11:** Linear regression of (a) interior transport convergence anomalies (RG) and (b) surface transport divergence anomalies (ORAS4) point-by-point onto SST anomalies at the time lag defined in Fig. 4.10b: INT-CONV leads by 2 months and Surf-DIV leads by 12 months. The time lags are based on lag correlations between transport and equatorial SST anomalies (averaged within the red box). Black contours mark significant regression coefficients, whereas white contours mark regions where than  $1 \text{ Sv}$  of INT-CONV (Surf-DIV) forces a negative SST anomaly of  $-2^\circ \text{C}$  ( $-1^\circ \text{C}$ ). A 5-year running mean is applied to all time series.

Finally, the temporal and spatial role of wind for equatorial SST anomalies and the horizontal STC branches is examined both on interannual (2-year running mean) and on decadal time scales (5-year running mean). A lag correlation analysis between zonally averaged zonal wind stress anomalies at each latitude and equatorial SST anomalies (Fig. 4.12a-b) reveals two things. First, a relatively instant connection (correlation coefficients above 0.5) is observed between local zonal wind stress and equatorial SST anomalies at both time scales. Second, away from local forcing, the southern hemisphere appears to be more closely linked to equatorial SST anomalies as indicated by high correlation coefficients between  $15^\circ - 25^\circ \text{S}$  with short lag (Fig. 4.12a). However, in the northern hemisphere, with a lag of about 2 years, we also find considerable correlation coefficients of more than 0.5 at both time scales.

Previous model studies discussed the role of local vs. remote forcing of equatorial SST variations, focusing on the Pacific. For instance, *Nonaka et al. (2002)* disagree with *Kleeman et al. (1999)* by showing that for decadal equatorial SST variations, the near-equatorial wind stress is as important as off-equatorial wind stress while *Kleeman et al. (1999)* proposed changes of wind stress and subduction mainly poleward of  $23^\circ \text{N/S}$  to impact equatorial SST changes. However, the findings of *Nonaka et al. (2002)* have later been questioned by *Kröger et al.*

(2005) who showed that the relative contributions of equatorial and off-equatorial wind stress in driving SST variability on interannual to decadal time scales are significantly different. Most recently, *Graffino et al.* (2019) showed that equatorial SST anomalies are mainly driven by local wind stress anomalies while changes in the STC transport are rather forced by off-equatorial wind stress anomalies. For the interior STC branches we observe maximum correlation with zonal wind stress anomalies slightly south of the equator and at a lead of about 3 months (Fig. 4.12c). At longer time scales the southern hemisphere still dominates interior transport anomalies (Fig. 4.12d) although the highest correlation is observed along the equator with wind leading RG-INT by about 6 months possibly indicating that interior transport is rather forced by their dynamical connection to equatorial upwelling rather than local wind stress.

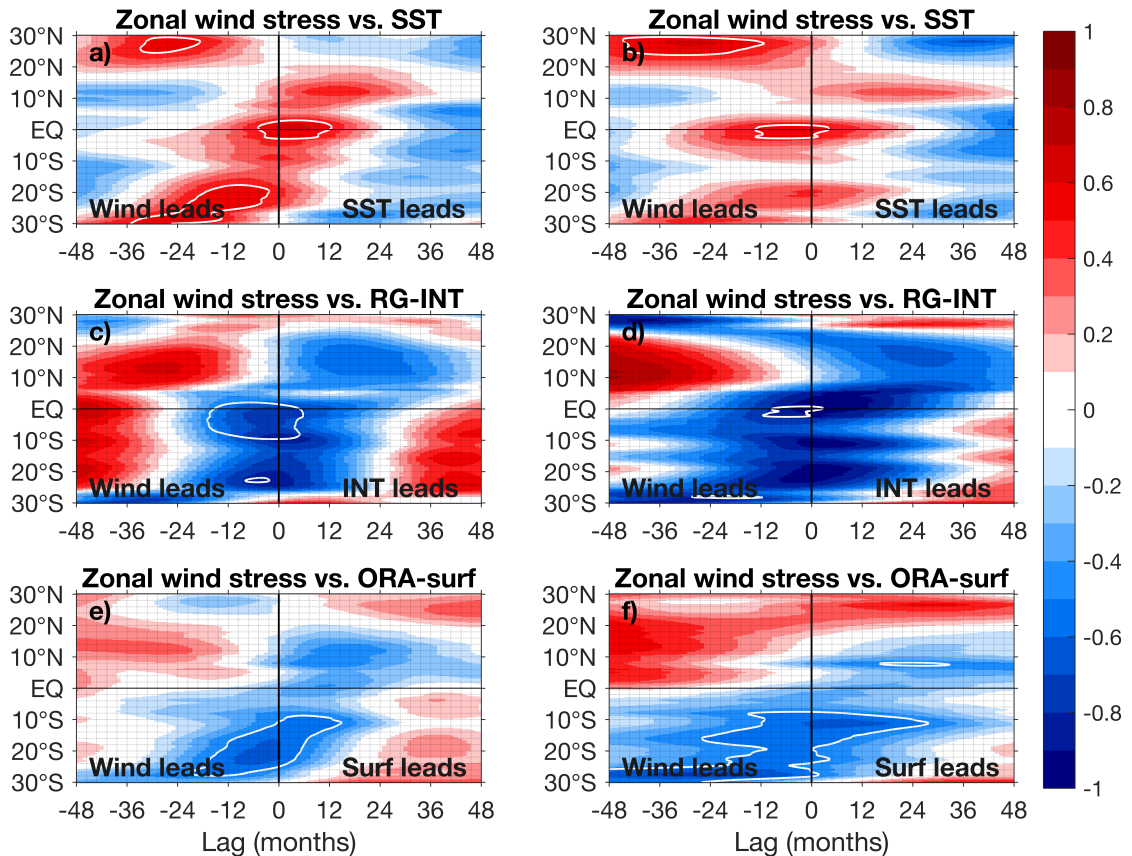


**Figure 4.12:** Lag correlation analysis as a function of latitude between zonal wind stress anomalies and (a, b) equatorial SST anomalies ( $30^{\circ}$  W- $10^{\circ}$  W,  $3^{\circ}$  S- $1^{\circ}$  N), (c, d) interior transport convergence anomalies and (e, f) surface transport divergence anomalies. All time series of the left (right) panels are smoothed by a 2-year (5-year) running mean. The -0.5 (0.5 for (a) and (b)) correlation isoline is marked by the white contours.

Lastly, in both surface layer STC branches, off-equatorial zonal wind stress changes in the southern hemisphere are dominating transport anomalies with close to no time lag around

10° S at both time scales (Fig. 4.12e-f) indicating that mainly the south-easterly trade winds force the observed surface layer transport divergence between 10° N and 10° S.

## 4.5 Summary and conclusion

In this study, the variability of transport associated with the individual horizontal branches of the Atlantic STCs and their impact on tropical SST variability on interannual to decadal time scales has been investigated by using a variety of observational and reanalysis products.

The study provides a first observational estimate of the temporal evolution of thermocline layer transport convergence and surface layer transport divergence (Ekman + geostrophy). In both horizontal STC branches, the seasonal cycle clearly dominates the time series (Fig. 4.2 and Fig. 4.3). Thermocline layer transport convergence calculated between 10° N and 10° S shows a seasonal cycle with minimum values of about 7–9 Sv in boreal summer and maximum values of about 12–14 Sv in boreal winter. By separating the total thermocline layer transport convergence into its hemispheric and western boundary/interior components, we show that the western boundary in the northern hemisphere and the interior part of the southern hemisphere section dominate the observed annual cycle (Fig. 4.2 and Fig. 4.4). While no statistically significant peaks are found on interannual or decadal time scales, which is likely a consequence of the rather short time period analyzed, the time series are clearly modulated on those longer time scales. Previous numerical studies also found rather small interannual variations of less than 2 Sv amplitude (Hüttel and Böning, 2006; Rabe et al., 2008). In the surface layer, the Ekman divergence between 10° N and 10° S exhibits a pronounced annual cycle of more than 10 Sv peak-to-peak amplitude (Fig. 4.4) which is eventually reduced by an out-of-phase annual cycle of the geostrophic transport convergence. Comparison between different products for western boundary transports reveals considerable differences depending on data coverage and handling. Here, we made use of the 11° S mooring array providing almost 5 years of velocity data at the western boundary for the time period 2013 to 2018 (update of Hummels et al., 2015). We conclude that the seasonal cycle of western boundary transport is best captured by ORAS4 whereas the transport calculation from the Argo data product underestimates the magnitude and shows larger differences in the seasonality of western boundary transport.

In a next step, we focused on the relation between interannual anomalies of western boundary and interior thermocline layer transports which are zonally separated at 10° W (32° W) in the northern (southern hemisphere) based on previous observational studies (Zhang et al., 2003; Tuchen et al., 2019). In both hemispheres, observations and reanalysis data show that contributions from the western boundary and the interior basin are anti-correlated and partially compensate each other (Fig. 4.5). This relation is weakest for the Argo product for the southern hemisphere which is likely a consequence of the mentioned misrepresentation of magnitude and seasonality of western boundary current transport. However, to our knowledge, this relation has not yet been derived from observations but shown in numerical studies



for the Pacific and Atlantic Ocean before. For the Pacific, *Capotondi et al. (2005)* show that variations at the western boundary and in the interior basin can both be associated with baroclinic Rossby wave adjustment. In their numerical study, large-scale changes of the wind stress curl drive instantaneous changes in the Ekman transport and Ekman pumping finally leading to changes of the subtropical gyres through an excitation of baroclinic Rossby waves. On their westward path Rossby waves are suggested to first impact the interior parts of the basins before reaching the western boundary. Rossby waves alter the density structure and the zonal slope of the thermocline which eventually leads to changes in meridional transport. The higher the baroclinic mode and the further away from the equator the larger the lag between changes in the interior and changes at the western boundary. In this study, we find an almost instantaneous anti-correlation (Fig. 4.5) suggesting that rather low-baroclinic Rossby wave adjustment dominates. The highest anti-correlation is found at a time lag of about 1 month with the western boundary leading interior transport anomalies consistent with *Rabe et al. (2008)* but contradicting to the theory of locally generated Rossby wave propagation. However, wind-curl forcing in the western parts of the basins and poleward of  $10^{\circ}$  N/ $10^{\circ}$  S could result in equatorward propagating coastally-trapped waves whose signature is then observed in our western boundary transport components and could therefore distort the phase relation to interior transport anomalies.

Overall, the total thermocline layer transport convergence undergoes a weakening from 2005 to 2010 which is followed by a strengthening until about 2015/2016 (Fig. 4.2). The northern hemisphere seems to dominate the recent strengthening while the southern hemisphere appears to be responsible for the previous weakening (Fig. 4.7). However, reanalysis data suggests that previous interannual thermocline layer transport variations have been alternatingly dominated by contributions from the southern and northern hemisphere.

The final focus of this study was to analyze the impact of STC transport variability on equatorial SST variability at longer time scales. We observe the highest anti-correlations between anomalies of the interior part of the thermocline layer transport convergence and equatorial SST ( $-0.89$  for RG-clim and  $-0.50$  for ORAS4-geostr; Fig. 4.10a). Including the western boundary thermocline layer transport convergence drastically reduces this anti-correlation (Fig. 4.8a and 4.9a) emphasizing the importance of the interior pathway as the link to the tropics. This is remarkable since, in the mean, the interior pathways are contributing less to the overall thermocline layer transport convergence but on pentadal time scales seem to be more closely related to SST variability. Another curious finding is that variations in the western boundary current transport and the total thermocline convergence are positively correlated with equatorial SST anomalies on both interannual and decadal time scales, suggesting that stronger STCs are associated with warmer SSTs. When considering thermocline layer convergence and surface layer divergence as the only contributors to the warm water volume (WWV) above the lower boundary of the thermocline layer (i.e. neglecting diapycnal transport), a thermocline layer convergence leads to an increase in WWV which is generally associated with an increase

in SST. Our results suggest that on longer time scales thermocline layer convergence and the surface layer divergence anomalies are more correlated indicating a smaller impact on WWV changes so that rather an anti-correlation between thermocline layer convergence anomalies and SST anomalies is established. The relation of transport anomalies and WWV deserves further attention and will require further analysis.

In the Pacific, *McPhaden and Zhang* (2002, 2004) found an anti-correlation between interior meridional transport and tropically averaged SST, similar to our results for the interior convergence. However, in their studies, due to sparse observational data at the western boundary only the interior transport convergence could be related to SST variability and transport at the western boundary had to be derived as a residual between Ekman transport and interior transport. Also, the sparseness of observations forced the authors to calculate meridional transport in temporal bins of 7 to 10 years. Consequently, *McPhaden and Zhang* (2002) were not able to cover interannual variability and rather focused on decadal timescales. However, their analysis generally supports the mechanism proposed by *Kleeman et al.* (1999). Our results partially question the previously assumed mechanism of how the thermocline layer branch of the STCs modulates equatorial SST temperature. It appears that only on longer time scales the STCs play a role in modulating SST anomalies along the equator and at the eastern boundary (Fig. 4.10c and 4.11a) while at shorter time scales the local wind stress forcing dominates SST changes (Fig. 4.10a-b, Fig. 4.12a-b). This is consistent with the findings of *Rabe et al.* (2008) who show that on time scales longer than 5 years to decadal an initial wind stress change is followed by, first, a response in the EUC and later in the STC transport convergence. However, in their study, the time lags between the responses of the different STC components was about 1 year which is considerably longer than observed in this analysis (Fig. 4.10d).

The presented study aims to serve as a first observational estimate of transport variability associated with the Atlantic STCs. The absence of observational studies on Atlantic STC variability emphasizes the need for an analysis of the temporal evolution of the horizontal branches of the STCs and a discussion of their link to equatorial SST anomalies – a relation which for the Atlantic Ocean, so far, is only discussed in a few model studies. The presented results challenge the view of how the STCs have an impact on equatorial SST anomalies and provide approaches for future numerical models to further investigate this relation. However, the role of STC driven SST anomalies in contrast or in combination with the tropical Atlantic modes remains unsolved and demands further analysis beyond the scope of this study. In addition, extensive observational efforts are needed to better resolve the spatial structure of the Atlantic STCs. Especially the western boundaries are sparsely sampled and introduce uncertainties to the analysis (*Tuchen et al.*, 2019). Long-term mooring arrays and repeated ship sections in the tropical Atlantic (e.g. *Hummels et al.*, 2015) are essential to resolve the temporal and spatial evolution of the Atlantic STCs.

## Acknowledgments

This study was supported by the German Federal Ministry of Education and Research (BMBF) as part of the BANINO project (03F0795A), RACE-Synthese (03F0824C) and by EU H2020 under grant agreement 817578 TRIATLAS project. We thank the captains, crews, scientists and technicians involved in several research cruises with RV Meteor in the tropical Atlantic that contributed to collecting data used in this study. The Argo climatology from Roemmich & Gilson is accessible via [http://sio-argo.ucsd.edu/RG\\_Climatology.html](http://sio-argo.ucsd.edu/RG_Climatology.html) (we used the latest update of the climatological values from January 17th 2020 and monthly anomalies from 2004-2019). Reanalysis data from ORA-S4 can be accessed via [ftp://ftp-icdc.cen.uni-hamburg.de/EASYInit/ORA-S4/monthly\\_1x1/](ftp://ftp-icdc.cen.uni-hamburg.de/EASYInit/ORA-S4/monthly_1x1/). C-2015 ASCAT and QuikScat data are produced by Remote Sensing Systems and sponsored by the NASA Ocean Vector Winds Science Team. Data are available at [www.remss.com](http://www.remss.com). ERA5 monthly averaged data on single levels from 1979 to present is distributed by the Copernicus Climate Change Service (C3S) (2017) under <https://doi.org/10.24381/cds.f17050d7>. ERA-interim monthly means of daily means can be accessed under [https://apps.ecmwf.int/datasets/data/interim-full-moda/levtype=sfc/?month\\_years=1996&param=165.128,166.128](https://apps.ecmwf.int/datasets/data/interim-full-moda/levtype=sfc/?month_years=1996&param=165.128,166.128). Microwave OI SST data are produced by Remote Sensing Systems and sponsored by National Oceanographic Partnership Program (NOPP) and the NASA Earth Science Physical Oceanography Program. Data are available at [www.remss.com](http://www.remss.com).



# 5 Conclusion

This thesis provides the first observational estimate of the mean characteristics of the Atlantic Subtropical Cells (STCs, chapter 3) mainly based on Argo data as well as an investigation of their observed transport variability and connection to tropical sea surface temperature (SST) anomalies (chapter 4). The individual studies are mainly based on Argo float observations and are complemented by ship section data, moored observations of velocity as well as reanalysis and satellite products. In this chapter the scientific questions raised in chapter 1 are revisited and discussed. The results of this thesis are thereby integrated into the current level of knowledge and the scientific progress is pointed out. First, the benefits and limitations of the Argo data set available at the time of publication, will be discussed (question 1) followed by a summary and discussion of the main characteristics of the mean Atlantic STCs (question 2). On this basis, transport time series of the individual horizontal STC components are derived and the dominant time scales of variability are identified (question 3) before their connection to tropical SST anomalies is examined (question 4). The chapter closes with an outlook providing an overview about ongoing research and possible future projects.

## 5.1 Scientific progress

- **Is the data density provided by Argo floats sufficient to realistically derive the mean characteristics of the Atlantic STC circulation?**

In the last 15 years, Argo floats have become a powerful source of hydrographic data that is used to address various scientific questions within the world oceans. The Roemmich and Gilson Argo climatology ([Roemmich and Gilson, 2009](#)) provides gridded three-dimensional fields of temperature and salinity of the upper 2000 m on a monthly basis. Here, it is used to derive an estimate of the 21st century mean state of the Atlantic STCs based on data between 2004 and 2016. Hydrographic sections along 10° N and 10° S, based on Argo data, reassuringly reproduce characteristic features like e.g. the eastward shoaling of the pycnocline (e.g. [Rabe et al., 2008](#)) and also signatures of fresh water input by the Amazon river (Fig. 3.2). A tremendous advantage of Argo float data comes into play when geostrophic velocities are derived from hydrographic properties (as described in sections 2.1 and 3.3). In this thesis, the horizontal displacement between

two float cycles is used as a reference for the relative geostrophic velocities obtained from the hydrographic measurements with a level of known motion, whereas previous observational studies relied on the assumption of a level of no motion in a certain depth layer (e.g. *Zhang et al., 2003*). Although meridional displacement at 1000 dbar is generally weak, this approach provides a more consistent derivation of geostrophic transport from Argo float data. However, despite the increased number of Argo float deployments in recent years, to date, only a mean displacement field at 1000 dbar can be obtained because the spatial-temporal coverage by Argo floats still is not sufficient enough to resolve seasonal variability of horizontal displacement. In the future, a temporally varying meridional displacement field is suggested for presumably even more accurate estimates. Naturally, the data density varies regionally (e.g. *Roemmich and Gilson, 2009*). Especially along the western boundary, data coverage through Argo float observations is sparser than in the open ocean (Fig. 3.1). Here, it is shown that sparse observations introduce transport uncertainty when compared to reanalysis products and ship section data (Fig. 3.6). In this thesis, an estimated difference of 2 Sv of equatorward thermocline layer transport is observed at the western boundary at 10° S when compared to ship section data.

In conclusion, vertical hydrographic profiles provided by Argo floats reproduce the characteristic sections of temperature, salinity and derived variables when compared to reanalysis products and regional observational records. However, transport estimates at the western boundary yet have to be complemented by ship section or moored velocity data as shown in chapter 3. Reanalysis data may help to identify differences in transport keeping in mind that they contain inherent uncertainties depending on their forcing, the assimilated observations and the assimilation methods.

- **Given a sufficient Argo float data distribution, what are the mean characteristics of the Atlantic STCs in terms of meridional transport, pathways and interhemispheric differences?**

An overview of the mean transports and horizontal pathways of the Atlantic STCs is provided by the schematic in chapter 3 (Fig. 3.9). On the basis of Argo float and reanalysis data, the vertical layers in which the Atlantic STC branches exchange water masses are identified in a first step. In previous studies the thermocline layer has mainly been assumed to be bounded by isopycnal surfaces. For instance, in *Zhang et al. (2003)* the thermocline layer is defined between  $23.4 - 26.0 \text{ kg m}^{-3}$  ( $23.6 - 26.4 \text{ kg m}^{-3}$ ) at 10° N (6° S). Model studies generally used a comparable density range (*Fratantoni et al., 2000; Malanotte-Rizzoli et al., 2000; Inui et al., 2002; Lazar et al., 2002; Hüttl and Böning, 2006*) although the vertical resolution among the mentioned models differs. In this thesis, only the lower boundary of the thermocline layer is defined as a fixed

isopycnal surface, whereas the interface between the surface and thermocline layer is defined by a seasonally varying depth. The eastward shoaling of the pycnocline leads to outcropping of isopycnals in the eastern part of the basin which would result in an interference of the thermocline layer with the wind-driven surface layer. Hence, in this thesis, the interface between the surface layer and the thermocline layer at  $10^\circ$  N and  $10^\circ$  S is defined as the depth at which the meridional velocity reverses sign from poleward to equatorward. This depth is set by the impact of wind stress on the ocean surface and the resulting ageostrophic Ekman flow. Therefore, it can only be estimated by reanalysis data providing absolute velocities. Reanalysis data shows that the interface depth is subject to a considerable seasonal cycle and generally varies between 30 – 70 m in both hemispheres (Fig. 3.4). It is important to note that only the implementation of a seasonally varying interface depth, instead of an annual mean, leads to good agreement between the different data products in deriving accumulated equatorward transport in the interior ocean (Fig. 3.6).

Based on vertical profiles of mean meridional geostrophic transport (Fig. 3.3), the lower boundary in both hemispheres is identified as the  $26.0 \text{ kg m}^{-3}$  isopycnal. Below, a mean poleward transport is observed that is not associated with the ventilation of the tropical thermocline by the STCs.

Having defined the vertical boundaries of the horizontal STC branches, meridional transports are derived and averaged for a time period between 2004 to 2016. A total of  $9 \text{ Sv}$  of equatorward transport is found at  $10^\circ$  S with  $5.2 \text{ Sv}$  west and  $3.8 \text{ Sv}$  east of  $32^\circ$  W. This is in good agreement with [Zhang et al. \(2003\)](#) who found about  $10 \text{ Sv}$  of STC transport at the same latitude with  $6 \text{ Sv}$  along the western boundary and  $4 \text{ Sv}$  within the interior ocean. It has been noted that it is nearly impossible for observational studies to distinguish between STC and MOC transport at the western boundary since multiple recirculations of the MOC within the STCs would lead to a loss of water mass characteristics making it impossible to differentiate between sources of STC and MOC water (e.g. [Hazeleger and Drijfhout, 2006](#)). As described in section 2.2, overall three different transport components are superimposed within the Atlantic western boundary current: the STCs, the AMOC and a Sverdrup compensation flow. The relative role of the western boundary transport components is therefore investigated in models. In differently forced experiments, the impact of wind and MOC on the western boundary transport can be separated showing that the MOC transport within the thermocline layer at the western boundary could account for about  $6 \text{ Sv}$  ([Fratantoni et al., 2000](#)). The western boundary thermocline layer transport derived in this thesis includes all transport components within this layer. In the northern hemisphere the northward flowing AMOC largely suppresses equatorward transport at thermocline level (e.g. [Jochum and Malanotte-Rizzoli, 2001](#)) resulting in a southward transport of about  $3 \text{ Sv}$  along  $10^\circ$  N of which more than 90% are observed west of  $50^\circ$  W (Fig. 3.9). In comparison, [Zhang et al. \(2003\)](#) obtain

slightly stronger equatorward transport with 3 Sv at the western boundary and 2 Sv in the interior. Overall, the southern hemisphere contributes about three times more water to the thermocline layer transport convergence (Fig. 3.9). Note that at 10° N the equatorward transport in the thermocline layer at the western boundary is largely fed by southern hemisphere water masses through the NBC retroflexion. Thus, the EUC is mainly fed by waters originating in the southern hemisphere (e.g. *Schott et al., 1998*). The western boundary transport at 10° S is derived from repeated ship sections (Fig. 3.9). The equatorward transport derived from ship sections is about 2 Sv higher than estimated by Argo data (Fig. 3.6). This transport difference emphasizes the necessity to complement Argo data with ship sections or moored velocity data which, unfortunately, are rare along the western boundary. Consequently, at 10° N a transport uncertainty at the western boundary is assumed. In the NBC retroflexion area north of the equator, *Bourlès et al. (1999)* observed mean equatorward western boundary transport at thermocline level based on several ship sections between 1989 to 1991. Although, mean transport derived from Argo float data is in agreement with *Bourlès et al. (1999)*, an uncertainty due to a data gap in the mean section remains (Fig. 3.2).

The asymmetric transport convergence at thermocline level (9 Sv in the southern, 3 Sv in the northern hemisphere) is compensated by symmetric flow divergence in the surface layer (Fig. 3.8). A set of satellite and reanalysis wind products agrees well on a symmetric Ekman divergence of about 21 Sv between 10° N and 10° S which is in good agreement with previous studies (e.g. *Zhang et al., 2003*; *Schott et al., 2004*). Eventually, the resulting Ekman divergence is reduced by a geostrophic surface layer convergence of about 6 Sv. Overall, the remaining transport residual of about 3 Sv is attributed to uncertainties due to sparse observations at the western boundary at 10° N and/or to tropical, diapycnal upwelling of the MOC equatorward of 10° N/S (e.g. *Roemmich, 1983*; *Hazeleger and Drijfhout, 2006*).

This thesis provides an updated estimate of the mean Atlantic STC transports which is an important benchmark for general circulation model studies. It serves as a reference that is in good agreement with previous observational (*Zhang et al., 2003*) and model studies (e.g. *Hazeleger and Drijfhout, 2006*). Furthermore, this study provides new insights into the vertical and horizontal structure of the horizontal STC branches in the Atlantic Ocean by thoroughly identifying the vertical boundaries of the STC branches from Argo float data and complementing transport estimates with additional observations. For now, this is the only observational STC study in the 21st century. Due to its general agreement with the results of *Zhang et al. (2003)* no strong changes of the mean STC pathways and transport strengths between the two time periods have been detected.



- **What are the dominant time scales of transport variability observed in the individual horizontal branches of the Atlantic STCs?**

Building up on the vertical separation of the horizontal STC branches in chapter 3, 16 years of Argo data between 2004 to 2019 are used to provide the first observational time series of the individual STC transport components (Figs. 4.2 and 4.3). Both the surface layer and thermocline layer transport at  $10^{\circ}$  N and  $10^{\circ}$  S are dominated by seasonal variability with maximum amplitude in boreal winter and minimum amplitude in boreal summer (Fig. 4.4). In the surface layer, the Ekman divergence marks the largest component reaching values between 20 – 25 Sv in boreal winter and a distinct minimum of about 10 Sv in August. Hence, the overall surface layer net transport (Ekman + geostrophy) is dominated by the seasonality and amplitude of the Ekman component and the geostrophic convergence reduces the poleward transport by about 5 – 7 Sv on average. In the thermocline layer, transports vary from about 7 Sv in boreal summer to about 14 Sv in boreal winter. At the western boundary, transport differences between reanalysis and Argo data are largest, indicating a similar uncertainty as described in chapter 3. The interior thermocline layer transport components agree well for the different data products (Argo, ORAS4) emphasizing that Argo data at the western boundary is generally too sparse to fully resolve the seasonal cycle.

In both layers, a semi-annual cycle can be found superimposed on the annual cycle. Additionally, a spectral analysis shows variability at a period of 120 days in all four transport components ( $10^{\circ}$  N/S, western boundary/interior). In equatorial (*Tuchen et al., 2018*) and eastern boundary zonal velocity records (*Kopte et al., 2018*) this variability has previously been noted. The 120-day period is suggested to be linked to equatorial and coastal Kelvin waves that excite westward propagating Rossby waves at off-equatorial latitudes.

On time scales longer than seasonal, transport variability is not significantly enhanced compared to an AR-1 red noise spectrum. Nonetheless, relatively weak interannual fluctuations with amplitudes of about 1 Sv are observed which likely modulate SST anomalies (see section 4.4.3). A recent strengthening of both the surface layer divergence and the thermocline layer convergence appears to be driven by enhanced transport in the northern hemisphere (Fig. 4.7a). This is somewhat surprising as, in the mean, the northern hemisphere STC contributes about three times less water to the overall thermocline layer convergence, but could be the main driver of this recent trend.

Following previous studies for the Pacific Ocean (e.g. *Lee and Fukumori, 2003*; *Capotondi et al., 2005*; *Schott et al., 2007*), this thesis separates the thermocline layer transport components into western boundary (WB) and interior (INT) transport anomalies. Despite the deficits of Argo data at the western boundary, a significant anti-correlation between both components is found in both hemispheres (Fig. 4.5). Generally, such

an anti-correlation is expected: Sverdrup dynamics prescribe that interior transport due to wind stress curl must be balanced by opposed transport at the western boundary. However, the role of the superimposed STCs could not be isolated in this thesis, but could be further investigated in suitable model simulations. *Capotondi et al. (2005)* attribute the partial compensation between WB and INT transport anomalies to baroclinic adjustment to Rossby waves through wind stress curl changes. In this thesis, the WB transport component appears to lead the INT transport which has been noted in previous studies as well (*Klinger et al., 2002; Capotondi et al., 2005*). This relation appears to be counter-intuitive when considering westward propagating waves. However, an additional time lag distortion through remotely forced Rossby waves poleward of  $10^\circ$  N/S could explain the observed time lag. From there, Rossby waves propagate westward, reach the western boundary and propagate equatorward as coastally-trapped waves and are potentially captured in the WB component at  $10^\circ$  N/S. This relation deserves more attention and needs to be further investigated in future research. The partial compensation of WB and INT transport has also been noted in model studies of the Atlantic Ocean, but the generation mechanism proposed by *Capotondi et al. (2005)* could not be confirmed (*Hüttel and Böning, 2006; Rabe et al., 2008*).

- **How is STC transport variability connected to tropical SST anomalies?**

One of the most important findings about the STCs is their connection to tropical SST anomalies on decadal time scales as shown in the Pacific Ocean (*McPhaden and Zhang, 2002, 2004*). For the Atlantic, however, no such relation has been shown in observational studies so far. In this thesis, the transport time series of the individual STC components described in the previous section and their relation to SST anomalies is investigated with a focus on observed time lags between the different branches, time scale dependencies of the results and an evaluation of the favored  $v'\bar{T}$  mechanism (*Kleeman et al., 1999*). STC transport variability is compared to SST anomalies from an areal average in which a linear regression analysis suggests the strongest connection ( $30^\circ$  W to  $10^\circ$  W and  $3^\circ$  S to  $1^\circ$  N; see Fig. 4.11). Model studies from the Pacific rather focused on tropical SST averages between  $9^\circ$  N to  $9^\circ$  S (*McPhaden and Zhang, 2002; Farneti et al., 2014*) - far away from expected equatorial upwelling regions - or mixed layer temperature in the Niño3 region (*Lübbecke et al., 2008*). The results in section 4.4.3 suggest that STC-driven SST variability is constricted to the central equatorial Atlantic and to some extent to the eastern boundary upwelling region (Fig. 4.11).

The most important result is that the interior thermocline layer transport convergence is suggested to modulate equatorial SST anomalies only on time scales longer than 5 years (5-year running mean; Fig. 4.10). This is consistent with model studies for the Pacific Ocean showing that SST variability on decadal time scales is associated to STC transport

changes while SST variability on shorter time scales is mostly attributed to equatorial wind forcing (e.g. *Nonaka et al.*, 2002; *Lohmann and Latif*, 2007). The present results generally confirm the mechanism proposed by *Kleeman et al.* (1999) while adding a time scale dependency to it for the Atlantic Ocean which is in agreement with the results of *Rabe et al.* (2008). At the time lag of maximum anti-correlation between INT transport convergence and SST anomalies, especially the equatorial Atlantic SST is modulated by STC variability (Fig. 4.11). A linear regression analysis suggests that an observed maximum INT transport convergence anomaly of about  $\pm 0.4 \text{ Sv}$  drives negative SST anomalies of about  $-0.8^\circ \text{ C}$  (Fig. 4.10).

At shorter time scales (2-year running mean), the thermocline layer transport convergence anomalies show maximum positive correlations with the transport anomalies leading SST anomalies by about 24 to 30 months. In contrast, the surface layer branch shows a significant anti-correlation at these time scales (Fig. 4.8). In the STC loop the wind-driven poleward STC branch is the first one to respond to wind stress changes followed by the upwelling branch that is mainly manifested in the EUC and only afterwards the thermocline layer branch responds (*Rabe et al.*, 2008). It is remarkable that only the surface layer net transport anomaly seems to lead SST anomalies while the Ekman divergence anomaly lags by about 4 months. These lead-lag relations appear to be insensitive to the window size of the applied filter (2-year and 5-year running mean; Figs. 4.8 and 4.9). In the Pacific, an instantaneous anti-correlation is reached between the interior part of the thermocline layer convergence and SST anomalies (*McPhaden and Zhang*, 2002). This thesis found a similar relationship in the Atlantic for equatorial SST anomalies. By distinguishing between western boundary (WB) and interior (INT) transport convergence at thermocline level (Fig. 4.10) a significant anti-correlation ( $r = -0.89$ ) is observed between INT transport convergence and SST anomalies at zero lag for time series filtered by a 2-year running mean. However, maximum correlation is found when SST leads by about 2 months. This counter-intuitive relation has previously been noted by *Klinger et al.* (2002) and *Capotondi et al.* (2005) for the Pacific Ocean. They proposed that averaging along the entire or large parts of the zonal sections could introduce artificial time lags since the STCs are continuously impacted by zonally propagating Rossby waves. Here, it is also argued that at these shorter time scales (2-year running mean applied) the observed strong anti-correlation between INT transport convergence and SST could, instead, arise from parallel, disconnected responses to the same wind forcing at the surface. An initial wind stress change forces anomalous Ekman divergence impacting both SST through changes in equatorial upwelling and thermocline layer transport through a spin-up or spin-down of the entire cell. Thus at interannual time scales, the results suggest that SST and STC variability in the tropical Atlantic are both associated with local forcing due to changes in zonal wind stress rather than impacting each other (Fig. 4.12).

The observed positive correlation between WB transport convergence and SST anomalies could be an indication of warm water volume conservation above the lower boundary of the thermocline layer. This is indicated by differences in the correlation of thermocline layer convergence and surface layer divergence for shorter (2-year running mean) and longer (5-year running mean) time scales. Clearly, more research is required regarding this relation.

In conclusion, the results of this study suggest that the interior part of the STCs modulate SST variability only on time scales longer than 5 years. The role of the western boundary for SST variability remains an open question. Eventually, it should be noted that by estimating the STCs at  $10^{\circ}$  N/S a lot of variability and interaction with the equatorial dynamics is missed between the thermocline layer and the upwelling branch, i.e. the EUC. Especially, recirculation between the EUC and the SECs or interaction with Tropical Instability Waves equatorward of the chosen sections at  $10^{\circ}$  N/S could introduce additional variability (e.g. [von Schuckmann et al., 2008](#)).

## 5.2 Outlook

The results of this thesis have advanced our three-dimensional perception of the Atlantic STCs and have provided new insights into their variability and connection to tropical SST fluctuations. Naturally, within the framework of such a thesis, unresolved issues and open questions remain of which the most pressing ones are presented in the following.

### 5.2.1 The recent strengthening of the STCs

Although the horizontal branches of the Atlantic STCs are dominated by seasonal variability they also show fluctuations on longer time scales, i.e. multi-year periods of increasing and decreasing transport. In chapter 4, a recent strengthening in both the surface layer net transport divergence and the thermocline layer transport convergence is observed (see Figs. 4.7 and 4.8). The strengthening is indicated by an increase of about 2 Sv between 2009 and 2015 in the surface layer and 1 Sv between 2010 and 2017 in the thermocline layer. At the equator, the horizontal layers of the STCs are connected with each other by the eastward shoaling EUC as part of the upwelling branch of the zonally averaged STCs. Though the EUC is generated locally by the eastward pressure gradient along the equator (e.g. [Brandt et al., 2014](#)), a strengthening of the horizontal STC branches is suggested as a remote forcing of increasing EUC transport.

Moored velocity records at  $23^{\circ}$  W/ $0^{\circ}$  N reveal a strengthening of the EUC core velocity from 2008 to 2018 (Fig. 5.1a and 5.2a). Although the strengthening of the horizontal STC branches rebounded between 2015 and 2017, the EUC core velocity continued to strengthen further until

2018/2019. Since then, the velocity records rather indicate a weakening of the EUC. In *Rabe et al. (2008)* the so-called STC loop is described by consecutive responses of the EUC and the thermocline layer transport to initial changes of the surface layer transport due to zonal wind stress fluctuations. The EUC strengthening is observed both at 23° W and - reassuringly - also at 10° W (Fig. 5.1b). Monthly anomalies (mean and seasonal cycle subtracted) of equatorial zonal velocity at both longitudes show anomalous eastward flow towards the end of the time series over a depth range between approximately 100 – 200 m (Fig. 5.1).

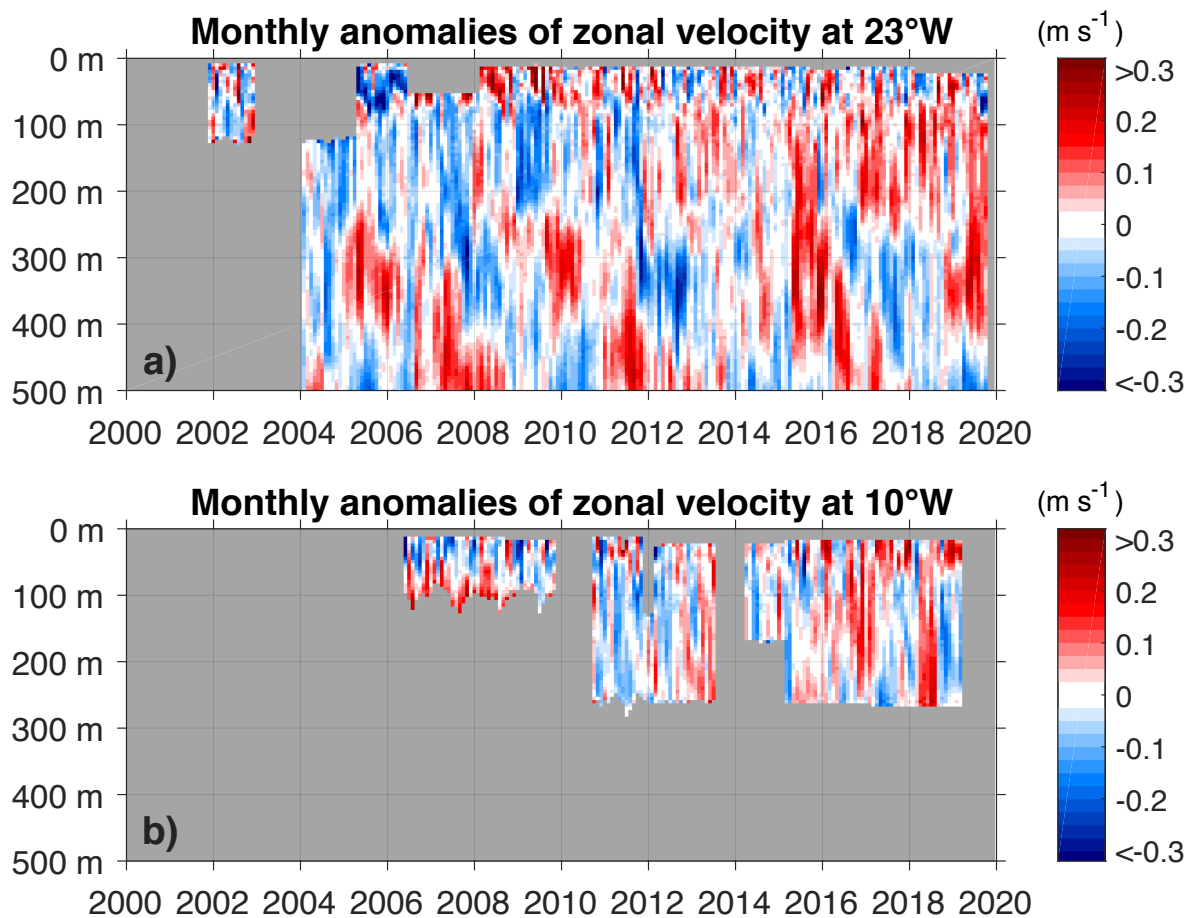


**Figure 5.1:** Monthly time series of equatorial zonal velocity anomaly with mean and seasonal cycle subtracted at (a) 23° W and (b) 10° W. Red (blue) colors indicate eastward (westward) anomalous flow. Data gaps are marked in grey.

In order to estimate the linear trend of zonal velocity at both mooring sites, the 10 year time period between August 2008 and July 2018 is chosen. Between 2008 and 2018, the surface flow down to about 50 m at 23° W became increasingly westward by about 0.1 m s<sup>-1</sup>, whereas the EUC between about 80 – 100 m at 23° W strengthened by about 0.2 m s<sup>-1</sup> (Fig. 5.2a). In comparison to the vertical mean structure of the EUC with its maximum at around 80 m (Fig. 5.2a, red curve) the strengthening of the eastward velocities extends from the core to around 200 m. At 10° W, a similar trend is indicated with stronger westward flow at the surface and stronger eastward flow below, but, most likely due to sparser observations, no significant

positive decadal trend can be derived since the confidence interval mostly includes the zero crossing.

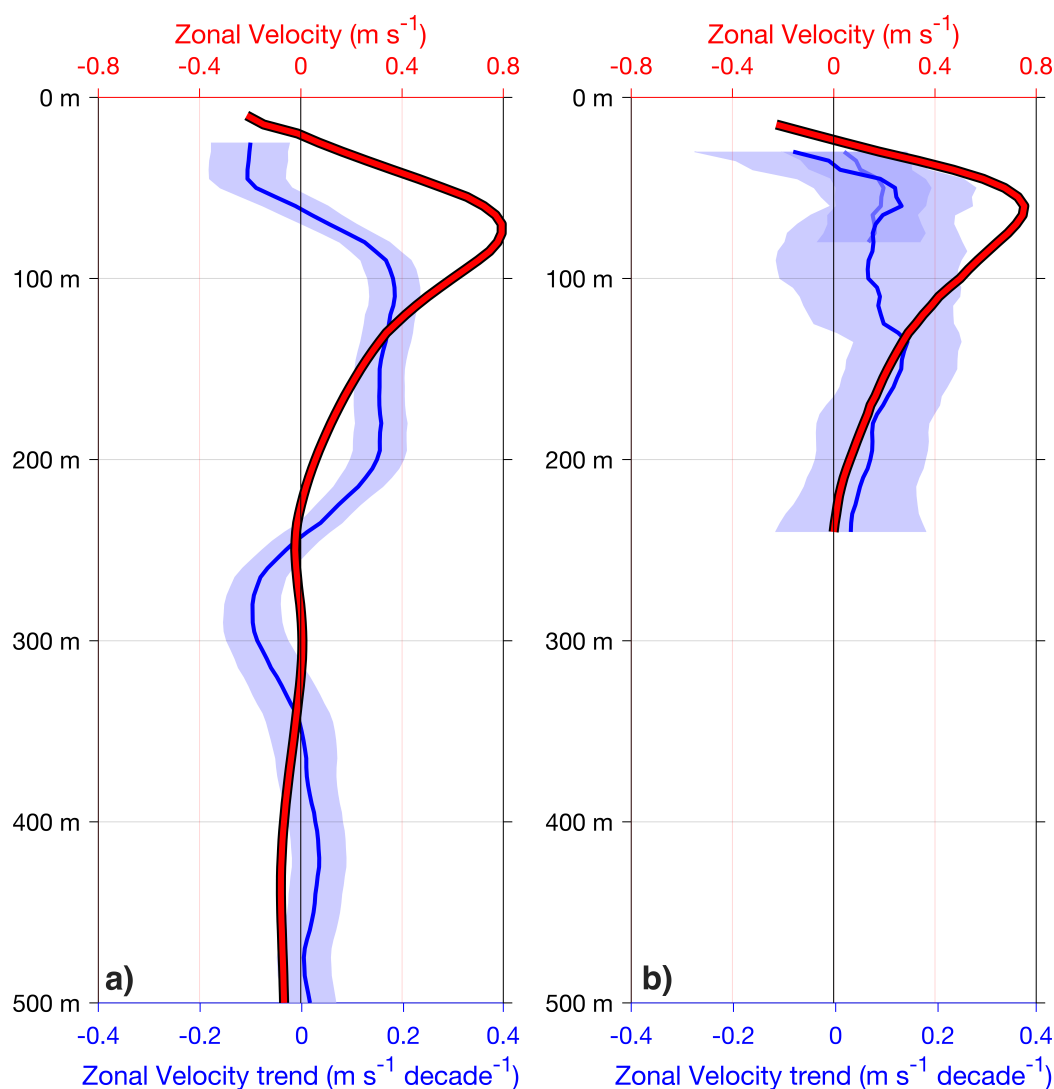


**Figure 5.2:** Linear trend (blue with 95% confidence interval shading) and mean equatorial zonal velocity (red) at (a) 23° W and (b) at 10° W. The trend at 23° W was calculated for the period August 2008 to July 2018 and at 10° W in the depth range 30 – 80 m for the period August 2008 to July 2018 and in the depth range 30 – 240 m for October 2010 to July 2018.

The EUC is generated locally by the eastward pressure gradient along the equator due to generally westward wind stress. To investigate the relative role of local versus remote forcing, the decadal trend in zonal wind stress from ASCAT is analyzed between August 2008 and July 2018. It shows that along the equator, only weak decadal trends are observed in the central basin of the equatorial Atlantic (Fig. 5.3). Clearly, the dominant signal is found in the northern hemisphere, where, especially in the western part of the basin between about 10° – 20° N, an acceleration of the easterlies has led an increase of the westward zonal wind stress by up

to  $-0.03 \text{ N m}^{-2} \text{ decade}^{-1}$ . In contrast, easterly trade winds in the southern hemisphere also accelerated predominantly over the eastern part of the basin but to a much weaker extent than in the northern hemisphere.

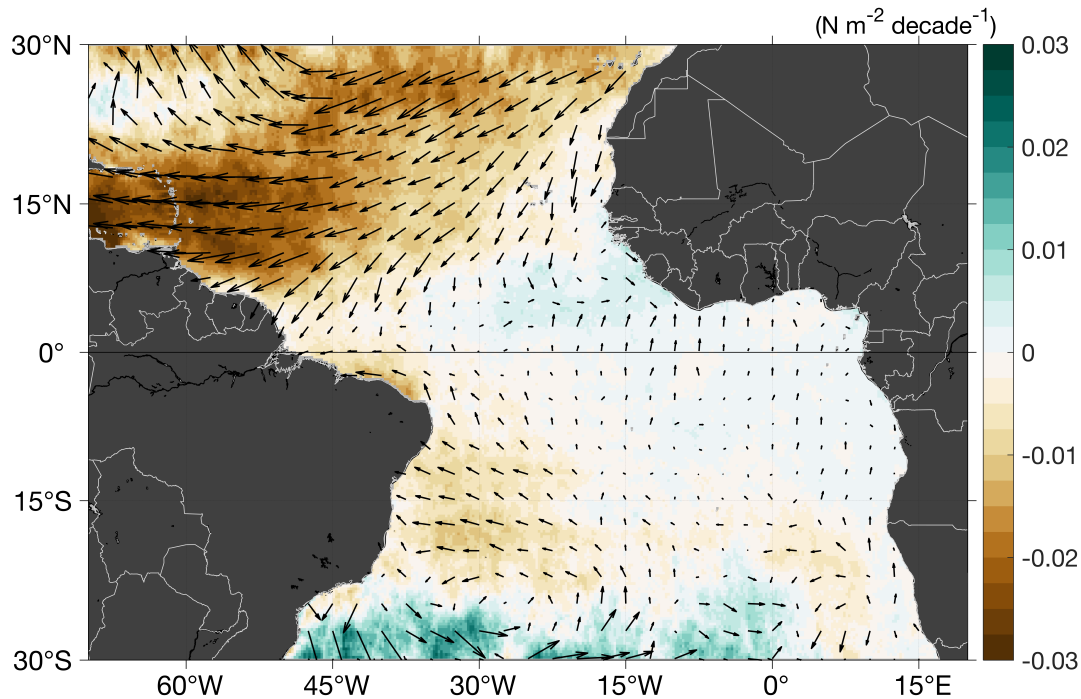


**Figure 5.3:** Linear decadal trend of wind stress (arrows) and zonal wind stress (color shading) between August 2008 to July 2018 derived from scatterometer data by ASCAT.

Consequently, the poleward Ekman transport shows a similar trend pattern due to its direct dependence on the zonal wind stress (Fig. 5.4). Note that close to the equator Ekman balance does not hold due to the vanishing Coriolis parameter (see section 2.1). In both hemispheres, stronger poleward Ekman transport at the western boundary is observed, though, this trend is clearly emphasized in the northern hemisphere. In the central basin, rather equatorward Ekman transport is observed. The supply of water towards the equator in the central and the divergence at the western boundaries explains the acceleration of the westward surface flow to balance changes in meridional water mass transport. Consequently, due to conservation of mass, the westward surface flow must be balanced by eastward transport at thermocline level by the acceleration of the eastward flowing EUC.

In conclusion, it is suggested that an acceleration of the easterlies in the western part of the northern hemisphere remotely forces a strengthening of the Atlantic EUC. In contrast local wind stress changes along the equator are fairly weak in comparison to the off-equatorial trend in zonal wind stress in the northern hemisphere. However, the persistence of the EUC trend beyond the strengthening maximum of the horizontal STC branches deserves further atten-

tion. Furthermore, the acceleration of the EUC has implications for the oxygen supply of the central and eastern equatorial Atlantic and thus impacts marine life in general. Clearly, more research is necessary to evaluate the impact of the recent strengthening of the EUC on the biogeochemistry in the tropical Atlantic.

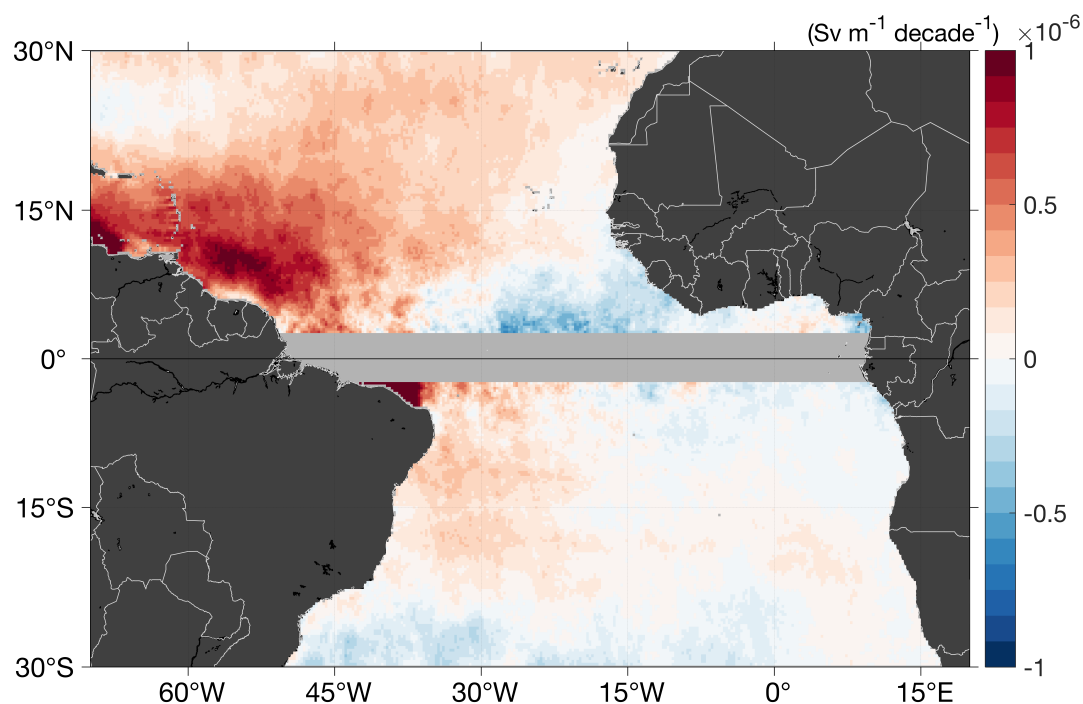


**Figure 5.4:** Linear decadal trend of poleward Ekman transport per unit length between August 2008 to July 2018 from ASCAT weekly wind data. Red (blue) colors indicate increasing (decreasing) poleward transports.

### 5.2.2 EUC water mass analysis

Previous studies agree that the EUC is mainly fed by the retroflection of the NBC north of the equator thereby mainly distributing southern hemisphere water (e.g. [Metcalf et al., 1962](#); [Schott et al., 1998](#); [Fratantoni et al., 2000](#)). However, the relative contribution of northern hemisphere water to the EUC is unclear (e.g. [Hazeleger et al., 2003](#)). In the Pacific Ocean, [Kuntz and Schrag \(2018\)](#) show that about 80 – 90 % of the EUC can be attributed to the southern hemisphere water. In their analysis, they defined a northern hemisphere and a southern hemisphere source water region where the surface density agrees with the density range of the Pacific EUC. Those northern and southern source water regions are mainly located within the subtropical gyres. By a simple comparison to the water mass composition of the EUC at each longitude, [Kuntz and Schrag \(2018\)](#) could quantify the ratio between southern



and northern hemisphere water.

In the Atlantic Ocean, a comparable analysis is complicated by the resemblance of subducted water masses in the northern and southern hemisphere subtropical gyres. Thus, to date, a clear separation of the Atlantic EUC water mass composition into northern and southern hemisphere origin is not possible based on hydrographic properties from Argo data. Future research could include additional parameters such as oxygen to carry out a multi-parameter analysis of the Atlantic EUC water mass composition. Furthermore, model studies and Lagrangian particle tracking could help to identify STC pathways and links for a possible water mass exchange between the northern and southern hemisphere and the equatorial Atlantic.

### **5.2.3 Concluding remarks**

The fundamental increase of observational data due to the start of the Argo program more than 20 years ago opened the possibility for this study investigating the STCs in detail from an observational perspective. Although, the main characteristics of the mean STCs and new insights into their transport variability are derived by this comprehensive available data set, several restrictions and limitations have also been addressed throughout this thesis. The importance of complementing Argo float observations with repeated ship sections and mooring arrays along the western boundary is emphasized. On the continental shelf, in upwelling regions or in areas with strong currents, observations by Argo floats are, to date, often still too sparse. In chapter 3 it is pointed out that the Argo-based western boundary transport at 10° N introduces one of the main uncertainties in the budget-like STC transport estimate (Fig. 3.9), whereas data from a repeated ship section in the southern hemisphere reveals the difference to Argo observations and provides a more accurate transport estimate at 10° S.

The results of this thesis highlight the benefits of the Argo program and demonstrate one of its possible applications. More years of Argo observations and the deployment of new floats that are able to cover the deep ocean (Deep Argo Mission) and/or are attached with further biogeochemical sensors (BioGeoChemical Argo mission) promise an exciting future for observational oceanography.



# Bibliography

- Amante, C., and B. W. Eakins (2009), ETOPO1 1 Arc-Minute Global Relief Model: procedures, data sources and analysis, *NOAA Technical Memorandum NESDIS NGDC-24*, doi:10.7289/V5C8276M.
- Athie, G., and F. Marin (2008), Cross-equatorial structure and temporal modulation of intraseasonal variability at the surface of the Tropical Atlantic Ocean, *Journal of Geophysical Research: Oceans*, *113*(8), 1–17, doi:10.1029/2007JC004332.
- Balmaseda, M. A., K. Mogensen, and A. T. Weaver (2013), Evaluation of the ECMWF ocean reanalysis system ORAS4, *Quarterly Journal of the Royal Meteorological Society*, *139*(674), 1132–1161, doi:10.1002/qj.2063.
- Belmonte Rivas, M., and A. Stoffelen (2019), Characterizing ERA-Interim and ERA5 surface wind biases using ASCAT, *Ocean Science*, *15*(3), 831–852, doi:10.5194/os-15-831-2019.
- Bourlès, B., R. L. Molinari, E. Johns, W. D. Wilson, and K. D. Leaman (1999), Upper layer currents in the western tropical North Atlantic (1989-1991), *Journal of Geophysical Research: Oceans*, *104*(C1), 1361–1375, doi:10.1029/1998JC900025.
- Brandt, P., V. Hormann, B. Bourlès, J. Fischer, F. A. Schott, L. Stramma, and M. Dengler (2008), Oxygen tongues and zonal currents in the equatorial Atlantic, *Journal of Geophysical Research*, *113*(C04012), doi:10.1029/2007JC004435.
- Brandt, P., G. Caniaux, B. Bourlès, A. Lazar, M. Dengler, A. Funk, V. Hormann, H. Giordani, and F. Marin (2011a), Equatorial upper-ocean dynamics and their interaction with the West African monsoon, *Atmospheric Science Letters*, *12*(1), 24–30, doi:10.1002/asl.287.
- Brandt, P., A. Funk, V. Hormann, M. Dengler, R. J. Greatbatch, and J. M. Toole (2011b), Interannual atmospheric variability forced by the deep equatorial Atlantic Ocean, *Nature*, *473*(7348), 497–500, doi:10.1038/nature10013.
- Brandt, P., A. Funk, A. Tantet, W. E. Johns, and J. Fischer (2014), The Equatorial Undercurrent in the central Atlantic and its relation to tropical Atlantic variability, *Climate Dynamics*, *43*(11), 2985–2997, doi:10.1007/s00382-014-2061-4.

- Brandt, P., M. Claus, R. J. Greatbatch, R. Kopte, J. M. Toole, W. E. Johns, and C. W. Böning (2016), Annual and Semiannual Cycle of Equatorial Atlantic Circulation Associated with Basin-Mode Resonance, *Journal of Physical Oceanography*, *46*(10), 3011–3029, doi:10.1175/JPO-D-15-0248.1.
- Bunge, L., C. Provost, and A. Kartavtseff (2007), Variability in horizontal current velocities in the central and eastern equatorial Atlantic in 2002, *Journal of Geophysical Research: Oceans*, *112*(C02014), doi:10.1029/2006JC003704.
- Burmeister, K., P. Brandt, and J. F. Lübbecke (2016), Revisiting the cause of the eastern equatorial Atlantic cold event in 2009, *Journal of Geophysical Research: Oceans*, *121*(7), 4777–4789, doi:10.1002/2016JC011719.
- Cane, M. A., and D. W. Moore (1981), A Note on Low-Frequency Equatorial Basin Modes, *Journal of Physical Oceanography*, *11*(11), 1578–1584, doi:10.1175/1520-0485(1981)011<1578:ANOLFE>2.0.CO;2.
- Capotondi, A., M. A. Alexander, C. Deser, and M. J. McPhaden (2005), Anatomy and Decadal Evolution of the Pacific Subtropical–Tropical Cells (STCs)\*, *Journal of Climate*, *18*, 3739–3758, doi:10.1175/JCLI3496.1.
- Carton, J. A., X. Cao, B. S. Giese, and A. M. Da Silva (1996), Decadal and Interannual SST Variability in the Tropical Atlantic Ocean, *Journal of Physical Oceanography*, *26*(7), 1165–1175, doi:10.1175/1520-0485(1996)026<1165:DAISVI>2.0.CO;2.
- Chang, P., L. Ji, H. Li, C. Penland, and L. Matrosova (1998), Prediction of tropical Atlantic sea surface temperature, *Geophysical Research Letters*, *25*(8), 1193–1196, doi:10.1029/98GL00852.
- Chang, P., R. Saravanan, L. Ji, and G. C. Hegerl (2000), The Effect of Local Sea Surface Temperatures on Atmospheric Circulation over the Tropical Atlantic Sector, *Journal of Climate*, *13*, 2195–2216, doi:10.1175/1520-0442(2000)013<2195:TEOLSS>2.0.CO;2.
- Chang, P., et al. (2006), Climate Fluctuations of Tropical Coupled Systems - The Role of Ocean Dynamics, *Journal of Climate*, *19*, 5122–5174, doi:10.1175/JCLI3903.1.
- Claus, M., R. J. Greatbatch, P. Brandt, and J. M. Toole (2016), Forcing of the Atlantic Equatorial Deep Jets Derived from Observations, *Journal of Physical Oceanography*, *46*(12), 3549–3562, doi:10.1175/JPO-D-16-0140.1.
- Cushman-Roisin, B., and J.-M. Beckers (2011), *Introduction to Geophysical Fluid Dynamics: Physical and Numerical Aspects*, Academic Press, doi:10.1080/00107514.2012.762047.

- Dee, D. P., et al. (2011), The ERA-Interim reanalysis: configuration and performance of the data assimilation system, *Quarterly Journal of the Royal Meteorological Society*, *137*, 553–597, doi:10.1002/qj.828.
- Enfield, D. B., and D. A. Mayer (1997), Tropical Atlantic sea surface temperature variability and its relation to El Niño-Southern Oscillation, *Journal of Geophysical Research: Oceans*, *102*, 929–945, doi:10.1029/96JC03296.
- Farneti, R., S. Dwivedi, F. Kucharski, F. Molteni, and S. M. Griffies (2014), On Pacific Subtropical Cell Variability over the Second Half of the Twentieth Century, *Journal of Climate*, *27*, 7102–7112, doi:10.1175/JCLI-D-13-00707.1.
- Foltz, G. R., and M. J. McPhaden (2010), Interaction between the Atlantic meridional and Niño modes, *Geophysical Research Letters*, *37*(L18604), doi:10.1029/2010GL044001.
- Foltz, G. R., et al. (2019), The Tropical Atlantic Observing System, *Frontiers in Marine Science*, *6*(May), 1–36, doi:10.3389/fmars.2019.00206.
- Fratantoni, D. M., W. E. Johns, T. L. Townsend, and H. E. Hurlburt (2000), Low-Latitude Circulation and Mass Transport Pathways in a Model of the Tropical Atlantic Ocean\*, *Journal of Physical Oceanography*, *30*(8), 1944–1966, doi:10.1175/1520-0485(2000)030<1944:LLCAMT>2.0.CO;2.
- Garzoli, S. L., A. Ffield, and Q. Yao (2003), North Brazil Current rings and the variability in the latitude of retroflection, *Interhemispheric Water Exchange in the Atlantic Ocean*, *68*, 357–373, doi:10.1016/S0422-9894(03)80154-X.
- Garzoli, S. L., A. Ffield, W. E. Johns, and Q. Yao (2004), North Brazil Current retroflection and transports, *Journal of Geophysical Research: Oceans*, *109*(C01013), doi:10.1029/2003jc001775.
- Goldenberg, S. B., C. W. Landsea, A. M. Mestas-Nuñez, and W. M. Gray (2001), The recent increase in Atlantic hurricane activity: Causes and implications, *Science*, *293*, 474–479, doi:10.1126/science.1060040.
- Graffino, G., R. Farneti, F. Kucharski, and F. Molteni (2019), The Effect of Wind Stress Anomalies and Location in Driving Pacific Subtropical Cells and Tropical Climate, *Journal of Climate*, *32*(5), 1641–1660, doi:10.1175/JCLI-D-18-0071.1.
- Gray, A. R., and S. C. Riser (2014), A Global Analysis of Sverdrup Balance Using Absolute Geostrophic Velocities from Argo, *Journal of Physical Oceanography*, *44*(4), 1213–1229, doi:10.1175/JPO-D-12-0206.1.

- Greatbatch, R. J., et al. (2018), Evidence for the Maintenance of Slowly Varying Equatorial Currents by Intraseasonal Variability, *Geophysical Research Letters*, 45(4), 1923–1929, doi:10.1002/2017GL076662.
- Grodsky, S. A., J. A. Carton, and C. R. McClain (2008), Variability of upwelling and chlorophyll in the equatorial Atlantic, *Geophysical Research Letters*, 35(L03610), doi:10.1029/2007GL032466.
- Gu, D., and S. G. H. Philander (1997), Interdecadal Climate Fluctuations That Depend on Exchanges Between the Tropics and Extratropics, *Science*, 275, 805–807, doi:10.1126/science.275.5301.805.
- Haarsma, R. J., E. Campos, W. Hazeleger, and C. Severijns (2008), Influence of the Meridional Overturning Circulation on Tropical Atlantic Climate and Variability, *Journal of Climate*, 21(6), 1403–1416, doi:10.1175/2007JCLI1930.1.
- Harper, S. (2000), Thermocline ventilation and pathways of tropical-subtropical water mass exchange, *Tellus, Series A: Dynamic Meteorology and Oceanography*, 52(3), 330–345, doi:10.3402/tellusa.v52i3.12269.
- Hazeleger, W., and S. Drijfhout (2006), Subtropical cells and meridional overturning circulation pathways in the tropical Atlantic, *Journal of Geophysical Research*, 111(C03013), doi:10.1029/2005JC002942.
- Hazeleger, W., M. Visbeck, M. A. Cane, A. Karspeck, and N. Naik (2001), Decadal upper ocean temperature variability in the tropical Pacific, *Journal of Geophysical Research: Oceans*, 106(C5), 8971–8988, doi:10.1029/2000JC000536.
- Hazeleger, W., P. de Vries, and Y. Friocourt (2003), Sources of the Equatorial Undercurrent in the Atlantic in a High-Resolution Ocean Model, *Journal of Physical Oceanography*, 33(4), 677–693, doi:10.1175/1520-0485(2003)33<677:SOTEUI>2.0.CO;2.
- Hersbach, H., and D. Dee (2016), ERA5 reanalysis is in production, *ECMWF Newsletter* 147:7.
- Hummels, R., P. Brandt, M. Dengler, J. Fischer, M. Araujo, D. Veleda, and J. V. Durgadoo (2015), Interannual to decadal changes in the western boundary circulation in the Atlantic at 11°S, *Geophysical Research Letters*, 42, 7615–7622, doi:10.1002/2015GL065254.
- Hüttl, S., and C. W. Böning (2006), Mechanisms of decadal variability in the shallow subtropical-tropical circulation of the Atlantic Ocean: A model study, *Journal of Geophysical Research*, 111(C07011), doi:10.1029/2005JC003414.
- Inui, T., A. Lazar, P. Malanotte-Rizzoli, and A. J. Busalacchi (2002), Wind Stress Effects on Subsurface Pathways from the Subtropical to Tropical Atlantic, *Journal of Physical*

- Oceanography*, 32(8), 2257–2276, doi:10.1175/1520-0485(2002)032<2257:WSEOSP>2.0.CO;2.
- Jochum, M., and P. Malanotte-Rizzoli (2001), Influence of the Meridional Overturning Circulation on Tropical–Subtropical Pathways, *Journal of Physical Oceanography*, 31(5), 1313–1323, doi:10.1175/1520-0485(2001)031<1313:IOTMOC>2.0.CO;2.
- Johns, W. E., T. N. Lee, R. C. Beardsley, J. Candela, R. Limeburner, and B. Castro (1998), Annual Cycle and Variability of the North Brazil Current, *Journal of Physical Oceanography*, 28(1), 103–128, doi:10.1175/1520-0485(1998)028<0103:ACAVOT>2.0.CO;2.
- Johns, W. E., P. Brandt, B. Bourlès, A. Tantet, A. Papapostolou, and A. Houk (2014), Zonal structure and seasonal variability of the Atlantic Equatorial Undercurrent, *Climate Dynamics*, 43(11), 3047–3069, doi:10.1007/s00382-014-2136-2.
- Jouanno, J., O. Hernandez, and E. Sanchez-Gomez (2017), Equatorial Atlantic interannual variability and its relation to dynamic and thermodynamic processes, *Earth System Dynamics*, 8(4), 1061–1069, doi:10.5194/esd-8-1061-2017.
- Karstensen, J., and D. Quadfasel (2002), Formation of Southern Hemisphere Thermocline Waters: Water Mass Conversion and Subduction\*, *Journal of Physical Oceanography*, 32(11), 3020–3038, doi:10.1175/1520-0485(2002)032<3020:FOSHTW>2.0.CO;2.
- Keenlyside, N. S., and M. Latif (2007), Understanding Equatorial Atlantic Interannual Variability, *Journal of Climate*, 20(1), 131–142, doi:10.1175/JCLI3992.1.
- Kleeman, R., J. P. McCreary, and B. A. Klinger (1999), A mechanism for generating ENSO decadal variability, *Geophysical Research Letters*, 26(12), 1743–1746, doi:10.1029/1999GL900352.
- Klinger, B. A., J. P. McCreary, and R. Kleeman (2002), The Relationship between Oscillating Subtropical Wind Stress and Equatorial Temperature\*, *Journal of Physical Oceanography*, 32(5), 1507–1521, doi:10.1175/1520-0485(2002)032<1507:TRBOSW>2.0.CO;2.
- Knight, J. R., R. J. Allan, C. K. Folland, M. Vellinga, and M. E. Mann (2005), A signature of persistent natural thermohaline circulation cycles in observed climate, *Geophysical Research Letters*, 32(L20708), doi:10.1029/2005GL024233.
- Knight, J. R., C. K. Folland, and A. A. Scaife (2006), Climate impacts of the Atlantic Multidecadal Oscillation, *Geophysical Research Letters*, 33(L17706), doi:10.1029/2006GL026242.
- Kopte, R., P. Brandt, M. Claus, R. J. Greatbatch, and M. Dengler (2018), Role of Equatorial Basin-Mode Resonance for the Seasonal Variability of the Angola Current at 11°S, *Journal of Physical Oceanography*, 48(2), 261–281, doi:10.1175/JPO-D-17-0111.1.

- Kröger, J., A. J. Busalacchi, J. Ballabrera-Poy, and P. Malanotte-Rizzoli (2005), Decadal variability of shallow cells and equatorial sea surface temperature in a numerical model of the Atlantic, *Journal of Geophysical Research*, *110*(C12003), doi:10.1029/2004JC002703.
- Kuntz, L. B., and D. P. Schrag (2018), Hemispheric Asymmetry in the Ventilated Thermocline of the Tropical Pacific, *Journal of Climate*, *31*(3), 1281–1288, doi:10.1175/JCLI-D-17-0686.1.
- Kushnir, Y., W. A. Robinson, P. Chang, and A. W. Robertson (2006), The Physical Basis for Predicting Atlantic Sector Seasonal-to-Interannual Climate Variability\*, *Journal of Climate*, *19*(12), 5949–5970, doi:10.1175/JCLI3943.1.
- Latif, M., C. W. Böning, J. Willebrand, A. Biastoch, J. Dengg, N. S. Keenlyside, U. Schweckendiek, and G. Madec (2006), Is the Thermohaline Circulation Changing?, *Journal of Climate*, *19*(9), 4631–4637, doi:10.1175/JCLI3876.1.
- Lazar, A., T. Inui, P. Malanotte-Rizzoli, A. J. Busalacchi, L. Wang, and R. Murtugudde (2002), Seasonality of the ventilation of the tropical Atlantic thermocline in an ocean general circulation model, *Journal of Geophysical Research*, *107*(C83104), doi:10.1029/2000JC000667.
- Lebedev, K. V., H. Yoshinari, N. A. Maximenko, and P. W. Hacker (2007), YoMaHa'07: Velocity data assessed from trajectories of Argo floats at parking level and at the sea surface, *IPRC Technical Note*, *4*(2).
- Lee, T., and I. Fukumori (2003), Interannual-to-Decadal Variations of Tropical–Subtropical Exchange in the Pacific Ocean: Boundary versus Interior Pycnocline Transports, *Journal of Climate*, *16*(12), 4022–4042, doi:10.1175/1520-0442(2003)016<4022:IVOTEI>2.0.CO;2.
- Liu, Z., S. G. H. Philander, and R. C. Pacanowski (1994), A GCM Study of Tropical–Subtropical Upper-Ocean Water Exchange, *Journal of Physical Oceanography*, *24*(12), 2606–2623, doi:10.1175/1520-0485(1994)024<2606:AGSOTU>2.0.CO;2.
- Lohmann, K., and M. Latif (2007), Influence of El Niño on the Upper-Ocean Circulation in the Tropical Atlantic Ocean, *Journal of Climate*, *20*(10), 5012–5018, doi:10.1175/JCLI4292.1.
- Lozier, M. S., et al. (2019), A sea change in our view of overturning in the subpolar North Atlantic, *Science*, *363*, 516–521, doi:10.1126/science.aau6592.
- Lu, P., J. P. McCreary, and B. A. Klinger (1998), Meridional Circulation Cells and the Source Waters of the Pacific Equatorial Undercurrent, *Journal of Physical Oceanography*, *28*(1), 62–84, doi:10.1175/1520-0485(1998)028<0062:MCCATS>2.0.CO;2.
- Lübbecke, J. F., and M. J. McPhaden (2012), On the Inconsistent Relationship between Pacific and Atlantic Niños\*, *Journal of Climate*, *25*(6), 4294–4303, doi:10.1175/JCLI-D-11-00553.1.



- Lübbecke, J. F., C. W. Böning, and A. Biastoch (2008), Variability in the subtropical-tropical cells and its effect on near-surface temperature of the equatorial Pacific: a model study, *Ocean Science*, 4, 73–88, doi:10.5194/os-4-73-2008.
- Lübbecke, J. F., B. Rodríguez-Fonseca, I. Richter, M. Martín-Rey, T. Losada, I. Polo, and N. S. Keenlyside (2018), Equatorial Atlantic variability - Modes, mechanisms, and global teleconnections, *Wiley Interdisciplinary Reviews: Climate Change*, 9(4), 1–18, doi:10.1002/wcc.527.
- Lumpkin, R., and S. L. Garzoli (2005), Near-surface circulation in the Tropical Atlantic Ocean, *Deep Sea Research Part I: Oceanographic Research Papers*, 52(3), 495–518, doi:10.1016/j.dsr.2004.09.001.
- Lux, M., H. Mercier, and M. Arhan (2001), Interhemispheric exchanges of mass and heat in the Atlantic Ocean in January–March 1993, *Deep Sea Research Part I: Oceanographic Research Papers*, 48(3), 605–638, doi:10.1016/S0967-0637(00)00033-9.
- Luyten, J. R., J. Pedlosky, and H. Stommel (1983), The Ventilated Thermocline, *Journal of Physical Oceanography*, 13(2), 292–309, doi:10.1175/1520-0485(1983)013<0292:TVT>2.0.CO;2.
- Malanotte-Rizzoli, P., K. Hedstrom, H. Arango, and D. B. Haidvogel (2000), Water mass pathways between the subtropical and tropical ocean in a climatological simulation of the North Atlantic ocean circulation, *Dynamics of Atmospheres and Oceans*, 32, 331–371, doi:10.1016/S0377-0265(00)00051-8.
- Martín-Rey, M., I. Polo, B. Rodríguez-Fonseca, T. Losada, and A. Lazar (2018), Is There Evidence of Changes in Tropical Atlantic Variability Modes under AMO Phases in the Observational Record?, *Journal of Climate*, 31(2), 515–536, doi:10.1175/JCLI-D-16-0459.1.
- McCreary, J. P., and P. Lu (1994), Interaction between the Subtropical and Equatorial Ocean Circulations: The Subtropical Cell, *Journal of Physical Oceanography*, 24(2), 466–497, doi:10.1175/1520-0485(1994)024<0466:IBTSAE>2.0.CO;2.
- McDougall, T. J., and P. M. Barker (2011), *Getting started with TEOS-10 and the Gibbs Seawater (GSW) Oceanographic Toolbox*, 34p pp., SCOR/IAPSO WG127.
- McPhaden, M. J., and D. Zhang (2002), Slowdown of the meridional overturning circulation in the upper Pacific Ocean, *Nature*, 415, 603–608, doi:10.1038/415603a.
- McPhaden, M. J., and D. Zhang (2004), Pacific Ocean circulation rebounds, *Geophysical Research Letters*, 31(L18301), doi:10.1029/2004GL020727.
- Metcalf, W. G., A. D. Voorhis, and M. C. Stalcup (1962), The Atlantic Equatorial Undercurrent, *Journal of Geophysical Research*, 67(6), 2499–2508, doi:10.1029/JZ067i006p02499.

- Molinari, R. L., S. Bauer, D. Snowden, G. C. Johnson, B. Bourlès, Y. Gouriou, and H. Mercier (2003), A comparison of kinematic evidence for tropical cells in the Atlantic and Pacific oceans, *Elsevier Oceanography Series*, 68, 269–286, doi:10.1016/S0422-9894(03)80150-2.
- Munk, W. H. (1950), On the Wind-Driven Circulation, *Journal of Meteorology*, 7(2), 80–93, doi:10.1175/1520-0469(1950)007<0080:OTWDOC>2.0.CO;2.
- Nagura, M., and M. J. McPhaden (2018), The Shallow Overturning Circulation of the Indian Ocean, *Journal of Physical Oceanography*, 48, 413–434, doi:10.1175/JPO-D-17-0127.1.
- Nnamchi, H. C., J. Li, F. Kucharski, I.-S. Kang, N. S. Keenlyside, P. Chang, and R. Farneti (2016), An Equatorial–Extratropical Dipole Structure of the Atlantic Niño, *Journal of Climate*, 29(10), 7295–7311, doi:10.1175/JCLI-D-15-0894.1.
- Nnamchi, H. C., M. Latif, N. S. Keenlyside, and W. Park (2020), A Satellite Era Warming Hole in the Equatorial Atlantic Ocean, *Journal of Geophysical Research: Oceans*, 125(4), 1–16, doi:10.1029/2019JC015834.
- Nobre, P., and J. Shukla (1996), Variations of Sea Surface Temperature, Wind Stress, and Rainfall over the Tropical Atlantic and South America, *Journal of Climate*, 9(10), 2464–2479, doi:10.1175/1520-0442(1996)009<2464:VOSSTW>2.0.CO;2.
- Nonaka, M., S.-P. Xie, and J. P. McCreary (2002), Decadal variations in the subtropical cells and equatorial pacific SST, *Geophysical Research Letters*, 29(7), 1116, doi:10.1029/2001GL013717.
- Olbers, D., J. Willebrand, and C. Eden (2012), *Ocean Dynamics*, 1–704 pp., Springer Berlin Heidelberg, Berlin, Heidelberg, doi:10.1007/978-3-642-23450-7.
- Oschlies, A., P. Brandt, L. Stramma, and S. Schmidtko (2018), Drivers and mechanisms of ocean deoxygenation, *Nature Geoscience*, 11(7), 467–473, doi:10.1038/s41561-018-0152-2.
- Pedlosky, J. (1987), An Inertial Theory of the Equatorial Undercurrent, *Journal of Physical Oceanography*, 17(11), 1978–1985, doi:10.1175/1520-0485(1987)017<1978:AITOTE>2.0.CO;2.
- Pedlosky, J. (1988), Entrainment and the Termination of the Equatorial Undercurrent, *Journal of Physical Oceanography*, 18(6), 880–886, doi:10.1175/1520-0485(1988)018<0880:EATTOT>2.0.CO;2.
- Pedlosky, J. (1991), The Link between Western Boundary Currents and Equatorial Undercurrents, *Journal of Physical Oceanography*, 21(10), 1553–1558, doi:10.1175/1520-0485(1991)021<1553:TLBWBC>2.0.CO;2.

- Pedlosky, J., and R. M. Samelson (1989), Wind Forcing and the Zonal Structure of the Equatorial Undercurrent, *Journal of Physical Oceanography*, *19*(9), 1244–1254, doi:10.1175/1520-0485(1989)019<1244:WFATZS>2.0.CO;2.
- Peña-Izquierdo, J., E. van Sebille, J. L. Pelegrí, J. Sprintall, E. Mason, P. J. Llanillo, and F. Machín (2015), Water mass pathways to the North Atlantic oxygen minimum zone, *Journal of Geophysical Research: Oceans*, *120*, 3350–3372, doi:10.1002/2014JC010557.
- Perez, R. C., V. Hormann, R. Lumpkin, P. Brandt, W. E. Johns, F. Hernandez, C. Schmid, and B. Bourlès (2014), Mean meridional currents in the central and eastern equatorial Atlantic, *Climate Dynamics*, *43*, 2943–2962, doi:10.1007/s00382-013-1968-5.
- Picaut, J., A. J. Busalacchi, M. J. McPhaden, and B. Camusat (1990), Validation of the geostrophic method for estimating zonal currents at the equator from Geosat altimeter data, *Journal of Geophysical Research*, *95*(C3), 3015–3024, doi:10.1029/JC095iC03p03015.
- Polo, I., A. Lazar, B. Rodríguez-Fonseca, and J. Mignot (2015), Growth and decay of the equatorial Atlantic SST mode by means of closed heat budget in a coupled general circulation model, *Frontiers in Earth Science*, *3*:37, doi:10.3389/feart.2015.00037.
- Rabe, B., F. A. Schott, and A. Köhl (2008), Mean Circulation and Variability of the Tropical Atlantic during 1952–2001 in the GECCO Assimilation Fields, *Journal of Physical Oceanography*, *38*(1), 177–192, doi:10.1175/2007JPO3541.1.
- Reynolds, R. W., T. M. Smith, C. Liu, D. B. Chelton, K. S. Casey, and M. G. Schlax (2007), Daily High-Resolution-Blended Analyses for Sea Surface Temperature, *Journal of Climate*, *20*(11), 5473–5496, doi:10.1175/2007JCLI1824.1.
- Ricciardulli, L., and F. J. Wentz (2015), A Scatterometer Geophysical Model Function for Climate-Quality Winds: QuikSCAT Ku-2011, *Journal of Atmospheric and Oceanic Technology*, *32*(10), 1829–1846, doi:10.1175/JTECH-D-15-0008.1.
- Ricciardulli, L., and F. J. Wentz (2016), Remote Sensing Systems ASCAT C-2015 Daily Ocean Vector Winds on 0.25 deg grid, Version 02.1, Santa Rosa, CA: Remote Sensing Systems.
- Richter, I., S. K. Behera, Y. Masumoto, B. Taguchi, H. Sasaki, and T. Yamagata (2013), Multiple causes of interannual sea surface temperature variability in the equatorial Atlantic Ocean, *Nature Geoscience*, *6*, 43–47, doi:10.1038/ngeo1660.
- Roemmich, D. H. (1983), The Balance of Geostrophic and Ekman Transports in the Tropical Atlantic Ocean, *Journal of Physical Oceanography*, *13*(8), 1534–1539, doi:10.1175/1520-0485(1983)013<1534:TBOGAE>2.0.CO;2.

- Roemmich, D. H., and J. Gilson (2009), The 2004–2008 mean and annual cycle of temperature, salinity, and steric height in the global ocean from the Argo Program, *Progress in Oceanography*, *82*(2), 81–100, doi:10.1016/j.pocean.2009.03.004.
- Rühs, S., F. U. Schwarzkopf, S. Speich, and A. Biastoch (2019), Cold vs. warm water route – sources for the upper limb of the Atlantic Meridional Overturning Circulation revisited in a high-resolution ocean model, *Ocean Science*, *15*, 489–512, doi:10.5194/os-15-489-2019.
- Schmidtko, S., G. C. Johnson, and J. M. Lyman (2013), MIMOC: A global monthly isopycnal upper-ocean climatology with mixed layers, *Journal of Geophysical Research: Oceans*, *118*, 1658–1672, doi:10.1002/jgrc.20122.
- Schneider, N., A. J. Miller, M. A. Alexander, and C. Deser (1999), Subduction of Decadal North Pacific Temperature Anomalies: Observations and Dynamics, *Journal of Physical Oceanography*, *29*(5), 1056–1070, doi:10.1175/1520-0485(1999)029<1056:SODNPT>2.0.CO;2.
- Schott, F. A., J. Fischer, and L. Stamma (1998), Transports and Pathways of the Upper-Layer Circulation in the Western Tropical Atlantic, *Journal of Physical Oceanography*, *28*(10), 1904–1928, doi:10.1175/1520-0485(1998)028<1904:TAPOTU>2.0.CO;2.
- Schott, F. A., P. Brandt, M. Hamann, J. Fischer, and L. Stamma (2002a), On the boundary flow off Brazil at 5–10°S and its connection to the interior tropical Atlantic, *Geophysical Research Letters*, *29*(17), 1840, doi:10.1029/2002GL014786.
- Schott, F. A., M. Dengler, and R. Schoenefeldt (2002b), The shallow overturning circulation of the Indian Ocean, *Progress in Oceanography*, *53*(1), 57–103, doi:10.1016/S0079-6611(02)00039-3.
- Schott, F. A., J. P. McCreary, and G. C. Johnson (2004), Shallow Overturning Circulations of the Tropical-Subtropical Oceans, *Earth Climate: The Ocean–Atmosphere Interaction. Geophysical Monography Series.*, *147*, 261–304, doi:10.1029/147GM15.
- Schott, F. A., M. Dengler, R. Zantopp, L. Stamma, J. Fischer, and P. Brandt (2005), The Shallow and Deep Western Boundary Circulation of the South Atlantic at 5°–11°S, *Journal of Physical Oceanography*, *35*(11), 2031–2053, doi:10.1175/JPO2813.1.
- Schott, F. A., W. Wang, and D. Stammer (2007), Variability of Pacific subtropical cells in the 50-year ECCO assimilation, *Geophysical Research Letters*, *34*(L05604), doi:10.1029/2006GL028478.
- Servain, J., I. Wainer, J. P. McCreary, and A. Dessier (1999), Relationship between the equatorial and meridional modes of climatic variability in the tropical Atlantic, *Geophysical Research Letters*, *26*(4), 485–488, doi:10.1029/1999GL900014.

- Servain, J., G. Caniaux, Y. K. Kouadio, M. J. McPhaden, and M. Araujo (2014), Recent climatic trends in the tropical Atlantic, *Climate Dynamics*, 43(11), 3071–3089, doi:10.1007/s00382-014-2168-7.
- Stommel, H. (1948), The westward intensification of wind-driven ocean currents, *Transactions, American Geophysical Union*, 29(2), 202, doi:10.1029/TR029i002p00202.
- Stramma, L., and M. England (1999), On the water masses and mean circulation of the South Atlantic Ocean, *Journal of Geophysical Research: Oceans*, 104(C9), 20,863–20,883, doi:10.1029/1999JC900139.
- Stramma, L., and F. A. Schott (1999), The mean flow field of the tropical Atlantic Ocean, *Deep Sea Research Part II: Topical Studies in Oceanography*, 46, 279–303, doi:10.1016/S0967-0645(98)00109-X.
- Stramma, L., J. Fischer, and J. Reppin (1995), The North Brazil Undercurrent, *Deep Sea Research Part I: Oceanographic Research Papers*, 42(5), 773–795, doi:10.1016/0967-0637(95)00014-W.
- Sutton, R. T., S. P. Jewson, and D. P. Rowell (2000), The Elements of Climate Variability in the Tropical Atlantic Region, *Journal of Climate*, 13(9), 3261–3284, doi:10.1175/1520-0442(2000)013<3261:TEOCVI>2.0.CO;2.
- Sverdrup, H. U. (1947), Wind-Driven Currents in a Baroclinic Ocean; with Application to the Equatorial Currents of the Eastern Pacific, *Proceedings of the National Academy of Sciences*, 33(11), 318–326, doi:10.1073/pnas.33.11.318.
- Tokinaga, H., and S.-P. Xie (2011), Weakening of the equatorial Atlantic cold tongue over the past six decades, *Nature Geoscience*, 4, 222–226, doi:10.1038/ngeo1078.
- Tsuchiya, M. (1986), Thermostads and circulation in the upper layer of the Atlantic Ocean, *Progress in Oceanography*, 16(4), 235–267, doi:10.1016/0079-6611(86)90040-6.
- Tuchen, F. P., P. Brandt, M. Claus, and R. Hummels (2018), Deep Intraseasonal Variability in the Central Equatorial Atlantic, *Journal of Physical Oceanography*, 48(12), 2851–2865, doi:10.1175/JPO-D-18-0059.1.
- Tuchen, F. P., J. F. Lübbecke, S. Schmidtko, R. Hummels, and C. W. Böning (2019), The Atlantic Subtropical Cells Inferred from Observations, *Journal of Geophysical Research: Oceans*, 124, 7591–7605, doi:10.1029/2019JC015396.
- von Schuckmann, K., P. Brandt, and C. Eden (2008), Generation of tropical instability waves in the Atlantic Ocean, *Journal of Geophysical Research: Oceans*, 113(C08034), doi:10.1029/2007JC004712.

- Wallace, J. M., E. M. Rasmusson, T. P. Mitchell, V. E. Kousky, E. S. Sarachik, and H. von Storch (1998), On the structure and evolution of ENSO-related climate variability in the tropical Pacific: Lessons from TOGA, *Journal of Geophysical Research: Oceans*, *103*(C7), 14,241–14,259, doi:10.1029/97JC02905.
- Xie, S.-P., and J. A. Carton (2004), Tropical Atlantic Variability: Patterns, Mechanisms, and Impacts, in *Earth Climate: The Ocean-Atmosphere Interaction, Geophysical Monograph Series*, vol. 147, pp. 121–142, American Geophysical Union, doi:10.1029/147GM07.
- Zhang, D., and M. J. McPhaden (2006), Decadal variability of the shallow Pacific meridional overturning circulation: Relation to tropical sea surface temperatures in observations and climate change models, *Ocean Modelling*, *15*, 250–273, doi:10.1016/j.ocemod.2005.12.005.
- Zhang, D., M. J. McPhaden, and W. E. Johns (2003), Observational Evidence for Flow between the Subtropical and Tropical Atlantic: The Atlantic Subtropical Cells\*, *Journal of Physical Oceanography*, *33*(8), 1783–1797, doi:10.1175/2408.1.
- Zilberman, N. V., D. H. Roemmich, and S. T. Gille (2013), The Mean and the Time Variability of the Shallow Meridional Overturning Circulation in the Tropical South Pacific Ocean, *Journal of Climate*, *26*(6), 4069–4087, doi:10.1175/JCLI-D-12-00120.1.

# Academic CV

**Franz Philip Tuchen** (\*09.09.1990 in Eckernförde, Germany)

*Mail:* ftuchen@geomar.de , *Phone:* +49 152 21701308

*Address:* Legienstraße 3, 24103 Kiel , *Nationality:* German

**Jun 2009: University-Entrance Diploma** at Jungmannschule Eckernförde, Germany.

**Oct 2010 - Sep 2013: Bachelor of Science** in "Physik des Erdsystems: Meteorologie - Ozeanographie - Geophysik" at Kiel University, Germany (6 semesters). Thesis: "Einfluss des Windschubes auf die Atlantische Umwälzbewegung" supervised by Dr. Thomas Martin and Prof. Dr. Mojib Latif.

**Oct 2013 - Dec 2016: Master of Science** in "Climate Physics: Meteorology and Physical Oceanography" at Kiel University, Germany (7 semesters). Thesis: "Intraseasonal Variability of the Equatorial Atlantic Ocean" supervised by Prof. Dr. Peter Brandt and Prof. Dr. Martin Claus.

**Apr 2017 - present: Doctoral Researcher** in the Physical Oceanography department at GEOMAR Helmholtz Centre for Ocean Research Kiel, Kiel, Germany. Thesis: "The Atlantic Subtropical Cells - mean state and variability from an observational perspective" supervised by Prof. Dr. Joke F. Lübbecke.





# Publications

5. **Tuchen, F. P.**, Lübbecke, J. F., Brandt, P., and Fu, Y. (under review): Observed transport variability of the Atlantic Subtropical Cells and their connection to tropical sea surface temperature variability, *Journal of Geophysical Research: Oceans*.
4. Brandt, P., Hahn, J., Schmidtko, S., **Tuchen, F. P.**, Kopte, R., Kiko, R., Bourlès, B., Czeschel, R., and Dengler M. (under review): Upper equatorial Atlantic current intensification counteracting warming induced deoxygenation, *Nature Geoscience*.
3. **Tuchen, F. P.**, Lübbecke, J. F., Schmidtko, S., Hummels, R., and Böning, C. W. (2019): The Atlantic Subtropical Cells Inferred from Observations, *Journal of Geophysical Research: Oceans*, 124, 7591-7605, <https://doi.org/10.1029/2019JC015396>
2. **Tuchen, F. P.**, Brandt, P., Claus, M., and Hummels, R. (2018): Deep Intraseasonal Variability in the Central Equatorial Atlantic, *Journal of Physical Oceanography*, 48, 2851-2865, <https://doi.org/10.1175/JPO-D-18-0059.1>
1. Greatbatch, R. J., Claus, M., Brandt, P., Matthießen, J.-D., **Tuchen, F. P.**, Ascani, F., Dengler, M., Toole, J. M., Roth, C., and Farrar, J. T. (2018): Evidence for the Maintenance of Slowly Varying Equatorial Currents by Intraseasonal Variability, *Geophysical Research Letters*, 45, 1923-1929, <https://doi.org/10.1002/2017GL076662>



# Acknowledgments

First and foremost, I want to thank Joke Lübbecke for granting me the opportunity to conduct this thesis as a doctoral researcher in the Physical Oceanography department. Joke's reliable supervision and continuous support were always motivating and kept me on track during the last 3.5 years. Especially in the beginning of my PhD time, when I was still working on publications originating from my Master thesis, I greatly appreciated her patience with me.

Further, I want to thank Peter Brandt. I largely benefited from his enormous knowledge of the dynamics of the tropical ocean and from his (always justified) critical view on my work since I was a Master student. I am also looking back with a lot of joy at several research cruises to the tropical oceans (four with Peter as chief scientist) that continuously channelled my enthusiasm for the observational oceanography.

I would also like to thank Mojib Latif and Arne Biastoch for agreeing to examine this thesis.

Throughout the last 3.5 years, my PhD advisory committee consisting of Joke Lübbecke, Sunke Schmidtke and Claus Böning provided helpful advice and guidance in return for coffee and cookies, for which I am very grateful. Here, I also want to thank the ISOS Graduate School for financially supporting various conference trips.

In the end, 3.5 years are a rather short period of time, especially when surrounded by great friends and colleagues in the PO department. It was a lot of fun in the B11 office under many different constellations and also outside of the office at conferences, research cruises or lunch breaks. Special thanks to Robert, Kristin, Rebecca, Flo, Johannes H., Jan, Yao, Tim, Arthur, Fehmi and Rodrigue for making this time both enjoyable and valuable. Thanks to Kristin, Rebecca, Robert, Johannes H. and Jan for their helpful comments on parts of this thesis. Thanks to Richard Greatbatch for organizing international bi-weekly online beer tastings under these special circumstances in 2020. I also want to thank the PO secretariat for their great support with all the administrative and bureaucratic issues (Nadira, Sigrun, Juliane, Christin).

Last but not least, I want to thank my family and friends for their continuous moral support during the last 3.5 years and during occasional "disappearances" on cruises or conferences and while writing this thesis.



# Declaration

I hereby declare that - apart from my supervisor's guidance and acknowledged assistance - the content and design of this thesis is my own work. This thesis has not been submitted either partially or wholly as part of a doctoral degree to another examining body and has not been published or submitted for publication. This thesis has been prepared in accordance with the Rules of Good Scientific Practice of the German Research Foundation. An academic degree has never been withdrawn from me.

Kiel, August 2020, \_\_\_\_\_

(Franz Philip Tuchen)